UNIVERSITY OF THESSALY
ENGINEERING SCHOOL
FACULTY OF MECHANICAL ENGINEERING

"Numerical and Experimental Study of a Formula Type Micro Scale Model"

Panagiotis K. Andreadis

Submitted in partial fulfillment of the requirements for the Diploma of
Mechanical Engineering

VOLOS 2021

Approved by the Examination Committee

1st Member:

(Supervisor) Assistant Prof. G. Charalampous, Department of Mechanical Engineering, University of Thessaly

2nd Member:

Prof. A. Stamatelos, Department of Mechanical Engineering, University of Thessaly

3rd Member:

Prof. A.Papathanasiou, Department of Mechanical Engineering, University of Thessaly

Abstract

The purpose of the study was to validate a CFD simulation setup that can be used for the design and development of complex aerodynamic devices used in Formula Student cars or F3 cars, in order to conduct comparative simulations and improve the performance of the race car. For this reason, wind tunnel experiments were conducted for 2 geometrically similar formula models at a 33% scale to each other, for 5 free stream velocities. The velocity profiles in front and behind the models, were experimentally measured using hot wire anemometry and the drag force on the model was estimated from the momentum equation. CFD simulations were also conducted for the same flow conditions and model geometries with the experiments. For the simulations tetrahedral and hexahedral meshes of coarse and fine volumes were compared in order to minimize the simulation's time. After the mesh independence study the k-e and k-ω turbulence models were compared to identify differences in the quality of the flow field, both far and close to the geometry's surface, but also how the drag is affected. The drag force on the formula models, extracted from the CFD simulations was compared to the drag force measurement from the wind tunnel experiments. After evaluating the discrepancy between the wind tunnel experimental results and the CFD calculations, a further simulation of 33% scale up geometry was conducted in order to extrapolate the model results to a full-scale model. In the end after proving that our CFD tools could be trusted for producing reliable results, the special case of Centaurus Racing Team's 5th race car, "Amphion", was also examined numerically in straight line and while cornering, in order to explain, how comparative CFD simulations can be useful for the design of an aerodynamic package and for predicting its performance.

Acknowledgements

First of all, I would like to express my thankfulness and gratitude to my supervisor, Professor Georgios Charalambous, for his continuous support and guidance throughout the dissertation of my thesis study. His observations, advices and problem-solving skills were vital for the quality improvement of my study. Moreover, I would like to thank the rest of the committee for their careful reading of my thesis.

Secondly, I would like to thank my best friends for all the times that we have past together up until now and for believing in me and my dreams. I should not forget to mention all my colleagues for the cooperation and patience during my 3-year experience in the Formula Student Team of our University, Centaurus Racing Team, were I learned a lot about race car aerodynamics and came I apart with challenging engineering problems. At this point I would also like to thank the following companies: Dassault Systemes, Simtec and Beta CAE Systems, for providing free licenses of the SOLIDWORKS (Licence Number: 902001317081970053RXK8J9), Ansys 18.1 (VENDOR_STRING=customer:20120530), ANSA and META v.18.0.1 (License Number: 10.64.33.248, for both), to Centaurus Racing Team, which I was able to use in my thesis dissertation.

Finally, above all, I would like to thank deeply my parents Kyriakos and Galini and my brother Ilias for their love and moral support over the whole period of my academic studies. All their sacrifices have led to a better future for me.

Table of Contents

List of Figures

List of Tables

Nomenclature

A	Frontal Area	m^2
A.R.	Aspect Ratio	%
AB	Aero Balance	%
B.A.	Vehicle Body slip Angle	degrees
C.O.G.	Vehicle Center of Gravity	-
C_d	Coefficient of Drag	-
C_l	Coefficient of Lift	-
COP	Center of Pressure	%
Cs	Coefficient of Side Force	-
D	Drag	N
D.A.	Vehicle Dive Angle	degrees
DF	Downforce	N
f.l.h.	First layer height	mm
g	Gravitational Constant	m^2/s
k	Turbulent kinetic energy	J/kg
L	Characteristic Length	m
L	Lift	N
m	Vehicle Mass	kg
P.A.	Vehicle Pitch Angle	degrees
p_{air}	Air Pressure	Pa
P_d	Dynamic Pressure	Pa
P_s	Static Pressure	Pa
Pt	Total Pressure	Pa
r	Turn Radius	degrees
R.A.	Vehicle Roll Angle	degrees

R_DD	Rear Damper Displacement	mm
R_Downforce	Rear Downforce	N
R_Fz	Rear Vertical Load	N
R_MR	Rear Motion Ratio	%
R_WD	Rear Wheel Displacement	mm
R_WR	Rear Wheel Rate	-
Re	Reynolds Number	-
Re	Reynolds Number	-
S	Side Force	N
S.A.	Vehicle Steering Angle	degrees
u+	Non-dimensional laminar boundary layer velocity	-
U_{air}	Air Translational Speed	m/s
U_{veh}	Vehicle Speed	m/s
W	Vehicle Weight	kg
Y.A.	Vehicle Yaw Angle	degrees
y+	Non dimensional normal cell wall distance	-
ε	Turbulent Dissipation Rate	J/kg*s
μ	Dynamic Viscosity	kg/m*s
ν	Kinematic Viscosity	m^2/s
ρ	Air Density	kg/m^3
T	Air Temperature	C or K
ω	Specific Dissipation Rate	1/s
ω_{air}	Air Rotational Speed	rad/sec
ω_{veh}	Vehicle Wheels Rotational Speed	rad/sec

1. Introduction

1.1 Formula SAE

1.1.1 FSAE Competition

Formula SAE is a student design competition organized by SAE International (previously known as the Society of Automotive Engineers, SAE). The competition first started in 1980 by the SAE student branch at the University of Texas at Austin after a prior asphalt racing competition proved to be unsustainable.

The concept behind the competition is the following: A team which consists of undergraduate students are challenged to design and construct a prototype car which complies with the rules stated by the FSAE community. The rules are both technical and organizational and might vary from one competition to another. A team can belong to each one of the following categories: combustion vehicle, electric vehicle and driverless vehicle.

During the competition, the teams compete in both static and dynamic events. The difference between the two is that during the static events the research and development of the design, the construction, the budget management and the marketing strategy of each team is judged and during the dynamic events the car's performance against time. The available points for each team are presented in Figure 1:

FSAE Events Scoring Table		
Static Events	Design	150
	Cost and Manufacturing	100
	Business Plan Presentation	75
Dynamic Events	Acceleration	75
	Skid Pad	75
	Autocross	100
	Endurance	325
	Efficiency	100
Total Score		1000

Figure 1: FSAE Scoring Table for Combustion Teams

1.1.2 Importance of Aerodynamics in FSAE

In order to design a fully operational aerodynamic package, which consists of the front wing, the rear wing, the sidepods, the undertray and the diffusers, most of the FSAE aerodynamic departments are conducting CFD simulations where they are placing the car in a straight tunnel in which the air is moving towards it. In that way the teams are simulating the same condition that is going through when a wind tunnel test is conducted. Even though the biggest percentage of the simulations is performed in a straight tunnel with the car having constant speed and flat ride height, aerodynamicists are gathering lot more information by simulating the car at different ride heights (pitch and dive angles), yaw angles but also by examining the air-vehicle interaction, while the car is travelling through a corner. Optimizing the performance of the race car at different dynamic conditions can maximize the downforce produced, but also the overall balance of the car during the endurance event, from which the team will draw the most points than any other event of the competition.

The most critical aspect of this research was the validation of the CFD tools that are used for the development of a Formula type car aerodynamic package. For this reason, the wind tunnel in the fluid mechanics laboratory was utilized to conduct experiments and draw valuable data from a TSI anemometer and pitot tube placed in different positions around the vehicle, which would then be compared to the data calculated by the CFD.

Since full model testing is not feasible in the wind tunnel, a micro scale model was created by 3D printing, with a simplified geometry in several regions which would be impossible for the 3D printer to create. The same model was used in the CFD simulations. Finally, after comparing the CFD and the wind tunnel data, we used the same setup to evaluate the performance of a real Formula Student car.

1.1.3 Previous Research

The literature on race car aerodynamics is large, especially in CFD research, because of the competitive nature of the sport. Many academic test cases, theses and papers exist, with a wide range of data available for validation.

Such a study was performed by a former student and member of the aerodynamics department [Oxyzoglou, 2018] whose thesis describes the process of designing and developing the aerodynamic package of the 2016 Formula Student race car of Centaurus Racing Team, named "Thireus", with the use of CAD Tools and Computational Fluid Dynamics (CFD). It investigates the effects of aerodynamics on the vehicle's behaviour and performance regarding the Formula Student competition regulations. After conducting several comparative simulations for each one of the aerodynamic devices, he proved the contribution of the front and rear wing to the overall performance of the car while validating the results using a lap time simulation.

Another study was conducted by [Frystak, 2016] at Brno Institute of Technology. His work focuses on wind tunnel testing of a 25% scale model of a Formula SAE racecar. First he reviews the theoretical background of his experiment, then he describes the experiment and presents the results. His goal was to determine the aerodynamic characteristics of the model and find areas from which improvement of these characteristics could be extracted. The testing was done with a scaled model of a Formula SAE race car, derived from TU Brno Racing's 2016 car, Dragon 6. Four different configurations were measured, differing in usage of a floor with diffuser and inverted wings. The model was mounted on a sting balance and measurements were done with stationary wheels and floor. The wind tunnel blockage in this configuration was approximately 20%. From load measurements for configurations without wings, it was found that the model produces lift. When using a floor with a diffuser, the overall lift was reduced. The resulting difference was 35% reduction in the overall lift and a 12% reduction in the overall drag. Configurations with wings produced downforce, but also considerably higher drag. However, the trend was different compared to configuration without wings. Although the difference was marginal, only 2%, with wings, the configuration with the diffuser produced lower downforce, than the configuration with planar floor. Probable cause for such unexpected behavior was thought to be resulting from balance deflection. Such deflection consequently induced a rake angle of the model, thus generating greater downforce. Even though the most dominant source of downforce were the wings, pressure coefficient distribution on the floor showed, that the rear wing also contributes to higher downforce generation on the floor. Moreover, due to the high blockage of the test section and the consequent pressure losses, he was unable to obtain

Reynolds number equivalent to full scale car's velocity of 50 and the maximum speed that was achieved in the wind tunnel was equal to 22.5 (m/s).

Another study that was used for data validation was that of [Sagmo, 2016] at the Norwegian University of Science and Technology. His study was also divided into two parts. The first part of the study was the evaluation of the accuracy of RANS steady state simulations with respect to predicting aerodynamic forces on the 2016 race car, Gnist. The second part was the investigation of the aerodynamic effects for a turning Formula Student vehicle, to see if significant discrepancies exist with respect to yaw cases. His study considered different RANS turbulence models such as: Spalart-Allmaras, Realizable k-ε and Menter SST k - ω. He found out that all of them were able to give fair results as long as flow was largely attached to wings with simple geometries. Relatively large discrepancies aroused when the turbulence models were asked to handle turbulent wakes in separated flows. For the case of estimating the overall performance of the formula student race-car Gnist, large discrepancy was observed between the estimates obtained from a simplified car geometry and the forces acting on the vehicle out on track. A good explanation for this discrepancy could be the simplification in the geometry of the model used in the CFD and secondly due to side winds present during track testing. When modeling cornering rotational flow around the car, significant difference was found with respect to pure yaw angle cases. Even for relatively large corner radii, or small corner indexes, modeling pure yaw angles would lead to opposing conclusions for the case assessing the yaw moment on the car. The conclusion was that the better approach would be to model a cornering car by implementing a rotational reference frame motion in addition to setting the appropriate vehicle attitudes.

[Dahlberg, 2014] from the KTH Royal Institute of Technology, studied the development procedure of an aerodynamic package aiming to be featured on KTH Formula Student Team's racecar. He focused on investigating the effects of aerodynamics on the vehicle's behavior and performance, in order to build an efficient aerodynamics package. In terms of methodology validation, he researched the correlation between a wind-tunnel experiment of a wing in ground proximity and its simulated counterpart.

[Flag and Hammond, 2006] from the University of Auckland conducted a research regarding the racecar's performance dependence on the increase of downforce. They used both computational fluid dynamics simulations and a wind tunnel research facility for his study. For the simulations, a half-cut model was tested solving the RANS equations and the Shear-Stress-Transport (SST) turbulence model, with the final design of the undertray to give a lift coefficient of -0.87. Moreover, a half-scale model was tested in the wind tunnel, using a moving

belt to simulate the ground boundary condition. It was found that the addition of a front and rear wing to the body and undertray design produced a lift coefficient of -2.36 and that the aerodynamic load, in its optimal configuration, on the front and rear wheels respectively was able to be adjusted between 43% on the front and 57% on the rear to 33% on the front and 67 % on the rear by changing the angle of the foils. Data collected from on-track measurements proved the experiment's validity as well as the enhanced overall performance that the aerodynamic package provided the race car with.

[Lesniewicz, Kulak and Karczewski, 2014], from Lodz University of Technologyfocused their study on the aerodynamic impact of a single rotating wheel. For the sake of their research they used both moving wall boundary and multiple reference frame simulation methods, with the latter to be proved the most accurate approach. Two tyre models were tested through simulations; a slick and a grooved one. The foremost critical contrasts between flow around the tire with grooves and the smooth tire were spotted not only in terms of drag coefficient but also pressure distribution.

[Wang, Hu, Xu, Li and Yang, 2013] aimed to isolate both the front and the rear wing and study their performance at first separately and afterwards implement them on the Formula Student racecar on several heights and observe their combined results. The simulation results were also compared to the experimental data that were extracted from a wind tunnel experiment. It was found that the optimal combination of heights was of 60mm for the front wing and 860mm for the rear wing. For the aforementioned setup and a velocity of 25m/s the car had a downforce of 680N.

[Keogh, Barber, Diasinos, and Doig, 2015] expressed the importance of downforce during vehicle cornering and the inability of the aerodynamicists to replicate this condition through experiments. They explained that whirling arms, rotating rigs and curved test sections may give a good but quite compromised insight into the cornering condition. For this reason, they focused on numerical simulations which allow a more detailed investigation of the flow field around a vehicle when it is travelling through a corner. After analyzing both the experimental techniques available and the numerical investigation of the Ahmed Body into a curved domain, they concluded that the close ground proximity, the high blockage and the type of motion make the experiments less effective when it comes to achieving the required flow conditions, in comparison to the CFD, which showed that during cornering the drag began to act on curved path and variation in Re occurred within the domain.

[Kratochvnl, Astraverkhau, Slanina, 2014] from CTU Cartech did a research in order to explain the reasons why the use of aerodynamics devices in Formula Student cars is important despite the fact that the top speed is a bit over 100 km/h, which might indicate that aerodynamics do not play an important role at these speeds. Through their research they present the C_l and C_d values of the front wing, the rear wing and whole car. The car's C_d value obtained from the CFD was validated by conducting an on track coast down test, while the C_l value from the bump of the dampers. For both measurements the car was travelling straight with steady speed. The CFD validation was important but only for checking the reliability of the CFD tools. The answer to question on why the aerodynamic devices should be used was given when 2 different wing configurations where tested to see how acceleration, deceleration, cornering and thus the overall performance is affected. The configurations are characterized as Minimal Downforce (Car without Wings) and Maximal Downforce (Car with front and rear wing). The results showed that the car was decelerating with extra 0.21 (G) when the maximal downforce configuration was applied, while for the same configuration the driver was going 2.4 seconds faster at track layout formed in the shape of an endurance/autocross track.

Finally, [Jareteg, Wallin, Bergfjord and Lindstrand, 2012] from Chalmers University of Technology focused on building a wind tunnel model that can be easily adjusted to various designs. This was implemented by creating a frame to which varying body features would be attached, with an additional system for featuring rolling wheels. A stiff and ridged backbone or frame was opted as a concept and printed plastic body parts would be added. Finally, aluminium wheels were attached to the tunnel. The measurements were carried out using a balance and pitot tubes that could be placed in different locations depending on each race car's needs.

Data from the before mentioned studies are included in specific parts of the current study, for validation purposes.

1.2 Background on vehicle Aerodynamics

1.2.1 Why do we study vehicle aerodynamics?

Aerodynamics is one of the most important design aspects in the automotive industry. The reason for that is the fuel economy which can be achieved through the aerodynamic efficiency which is deeply connected to the minimization of the resistance of the air through which the car is travelling. Less air resistance means lower power dependence, in other words less fuel. The aerodynamic efficiency can be measured through the C_l/C_d ratio of the car, where C_l stands for coefficient of lift and C_d for the coefficient of drag.

Additionally, especially in the field of motorsport, aerodynamics can play an important role in the overall performance of the car. External aerodynamics can be extremely beneficial to the vehicle's dynamics, since the higher the vertical load on the tires, the higher the force generation due to friction. More friction results to a better functionality of the tires, thus the car gains more grip, so the driver can apply more throttle and travel faster through corners.

1.2.2 How are the aerodynamic forces created?

For a moving body, the pressure on the body surface and the air velocity over the body surface varies from point to point. Aerodynamic forces are generated through the pressure distribution on the body surface, which acts perpendicular to the surface and from the skin friction, which is caused by the viscosity of the fluid and acts tangentially to the surface. The net force can be found by integrating (or summing) the pressure and friction forces across the entire surface. For some simple flow problems, we can determine the pressure distribution (and the net force) if we know the velocity distribution by using Bernoulli's equation.

1.2.3 Aerodynamic Lift

A lot of arguments have aroused concerning the creation of lift and most of them are concerned to the Bernoulli's and Newton equations, but most of them are misleading because they oversimplify the problem of the aerodynamic lift[https://www.grc.nasa.gov/www/k-12/airplane/short.html].

The most popular incorrect theory arises from the misapplication of the Bernoulli equation. This theory is well known as the "equal transit time" or "longer path" theory. This theory states that the wings are designed with the upper surface longer than the lower surface in order to generate higher velocities on the upper surface because the molecules of the fluid have to reach the trailing edge at the same time as the molecules of the lower surface. The theory then invokes the Bernoulli's theory to describe the lower pressure on the upper side and the higher pressure

on the lower side. Knowing the velocity distribution, we can use the Bernoulli principle to extract pressure and thus the force. The problem here is that the equal transit velocity is not correct since the velocity on the upper surface of a lifting wing is much higher than the equal transit velocity. Another false theory is the one of the venturi flows, but this is also misleading since a wing section is definitely not a venturi nozzle.

The final incorrect theory corresponds the misapplication of Newton's third law of the interaction between two objects. This theory equates the lift force to a stone skipping across the water, but the problem here is that it neglects both sides of the wing contribute to the turning of the flow. The principle of the conservation of momentum dictates that as the stone enters the water and pushes some of the water downwards, the stone is forced upwards. This force is equal to the hydrodynamic pressure on the stone multiplied by its area. Assuming that this force is balanced against the weight of the stone, then Mg, where M is its mass and g is the acceleration due to gravity, there is a minimum velocity, a few kilometers per hour above which, the stone will bounce.

The actual way in which lift is generated is much more complex and does not lend itself to any kind of simplification. Especially in the case of a gas, we must simultaneously conserve the mass, the momentum and energy. Newton's laws correspond to the conservation of momentum whilst the Bernoulli's equation is derived by the conservation of energy. So, both above theories are satisfied in the generation of lift. But the complexity is introduced with the conservation of mass. From the conservation of mass, a change in velocity in one direction results in a change in the velocity of the gas in the direction perpendicular to the original change. The simultaneous conservation of mass, momentum and energy while taking into consideration the viscous effects are the Navier Stokes equations. Solving these equations can give us a quite good prediction of the pressure and velocity field around the object.

1.2.4   Aerodynamic Drag

Drag is a mechanical force that can only be produced if an object comes in physical contact with a fluid. Drag is generated by the difference in velocity between the solid and the fluid. Since it is a mechanical force it has both magnitude and direction. The direction on which it acts is the one opposite to the solid's direction of movement. There are 3 sources of aerodynamic drag [Cook, 2007]. One of the sources of drag is the skin friction between the fluid's molecules and the solid's surface. The second source of drag depends on the object's shape and is called form drag; in other words, it is the aerodynamic resistance to the motion of the object through the fluid. As the air flows round the object there are variations on the local velocity and pressure.

Since pressure is a measure of the momentum of the air molecules, a change of momentum will result in a creation of force. The component of this force that opposes the object's movement is the form drag. Finally, the 3rd form of drag is the induced drag Figure 2 which is the drag caused by the generation of lift. Induced drag occurs because the distribution of lift is not uniform on an aerofoil but varies from the leading to the trailing edge. Considering a flow around an aerofoil, there is pressure difference between the upper and the lower surface. Air from the high-pressure region has the tendency to move to the lower pressure region. This movement creates vortices which are formed at the aerofoil's trailing edges as it is seen from the following figure:
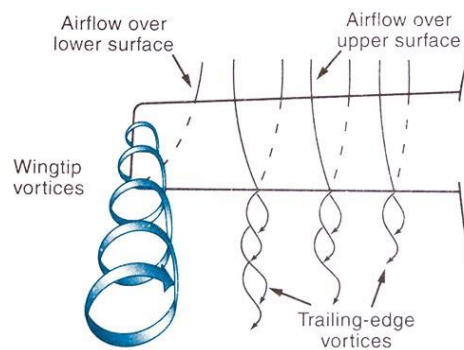
Figure 2: Representation of Induced Drag

The swirling flow is very strong and when speaking about airplane aero foils they create a downstream facing force. This force is called induced drag because it has been induced by the action of the tip vortices (see Figure 2). If we do not have any lift the pressure would be the same on both sides so no drag would be induced.

1.2.5   Aerodynamic Side Force

Side Force is created when the yaw angle of the object is changing. The yaw angle is the angle between the direction of the air and the direction to which the object is heading.

1.2.6   Centre of Pressure or Aerodynamic Balance

When speaking about the center of pressure of an object that moves through air, we refer to the position were the resultant aerodynamic force is exerted this resultant aerodynamic force can be analyzed into 3 components the drag, the side force and the lift or downforce [Research Glenn Center, Aerodynamics Index].

In other words we call the center of pressure as the average location of the pressure distribution, in the same way that we call the average location of the weight of an object the center of gravity. The center of pressure is proportional to the pressure distribution around the object that we are

studying but as someone can understand the pressure distribution around the object is very sensitive depending on the velocity magnitude of the object, the angle of attack in case that we are studying a wing. So, a minor change to the above factors can lead to a change in the pressure distribution and thus to the location of the center of pressure.

In our case and generally in motorsport defining the location of the C.O.P. of the car for some given conditions (speed, roll angle, yaw angle, pitch angle etc.) is significantly important. In the motorsport language the C.O.P. is called aero balance, which is a percentage that shows how close is the location of the C.O.P. to the front or the rear axle of the car. When the location is closer to the front axle that means that for the conditions on which it was calculated the front tires of the car have more grip since they receive a bigger percentage of downforce in comparison to the rear ones. Depending on the suspension's performance goals, the dynamic balance of the car and the lateral acceleration that a car is designed to produce, the suspension engineers give for an average steady state condition a specific goal to the aerodynamicists in order to have the optimum stability in the car. Due to limited resources of the formula team, we are not able to implement our car with all the needed sensors in order to create a network that will be able to provide us, through mathematic channels, the downforce and drag values while our car is running on track. The only way in which we can calculate the discrepancy between the CFD and the track data is the determination of the C.O.P. location with respect to the front and the rear axle, during steady state conditions (ex. while the car is travelling with a steady speed, or while turning with a turning speed), so that the calculations can be simplified since the load transfers can be neglected. The way in which the C.O.P. is determined both in the CFD and on track is going to be further analysed in the respective fields of the thesis.

1.3 Vehicle Dynamics

Vehicle dynamics is one of the most important aspects of the vehicle and one must have a good knowledge from that aspect in order to understand the relationship between aerodynamics vehicle performance. At this point it would be important to explain that we will not go deep into the analysis of this topic since it is not the main subject of this thesis. The only purpose is to show and explain in a simple way the mathematical relationship and the influence of the aerodynamic forces on the vehicle's performance and behaviour.

The performance of a racing car is defined by the amount of lateral and longitudinal acceleration that can be produced with respect to the tire's specification. The tire specification provides the engineers with the maximum lateral and longitudinal acceleration that can be achieved from a

car, using a specific set of tires. In any vehicle model the basic tire forces that relate the vehicle motion to the grip forces each tire exchanges with the road, should be constructed. These forces consist of the longitudinal (Fx) force, the lateral force (Fy) and the yaw moment (Mz). Under steady-state conditions, it is often assumed that, for each wheel with tire, these grip forces and moments depend on the following parameters:

$$F_x = F_x\left(F_z, \gamma, \sigma_x, \sigma_y, \varphi\right)$$
$$F_y = F_y\left(F_z, \gamma, \sigma_x, \sigma_y, \varphi\right)$$
$$M_z = M_z\left(F_z, \gamma, \sigma_x, \sigma_y, \varphi\right)$$

where,

1. Fz, is vertical load acting on each tire
2. γ is the camber angle
3. σx is the longitudinal theoretical slip
4. σy is the lateral theoretical slip
5. ϕ is the spin slip

We will not give the analytical expression for the Fx,Fy, Mz and we will not analyze the other parameters rather than the vertical load, since they are quite complex, and they contain an awful lot of theory that needs to be explained. We just want to show that they are proportional to down force and that is the actual way in which aerodynamics help the car go faster.

1.3.1 Friction Circle

Tires are responsible for providing the connection between the car and the tarmac. Through this connection the driver can accelerate, brake and corner. The most important thing is that the amount of grip or force that can be produced is finite, and this can be described in a simple way by the traction circle which is a simplification of the friction ellipse:
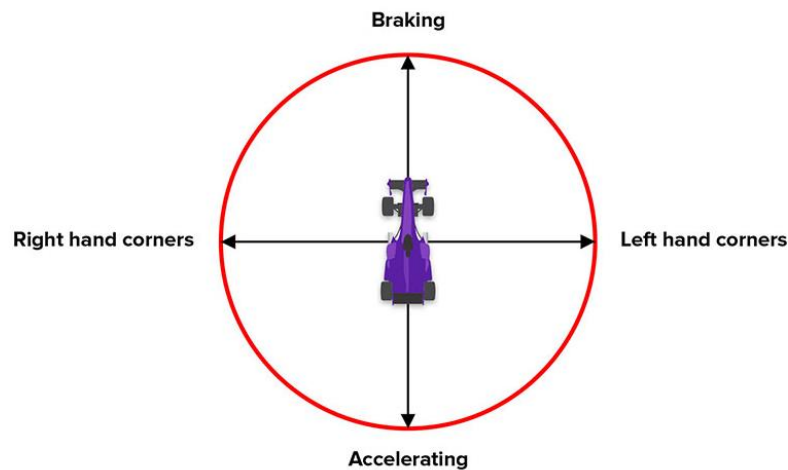
Figure 3: Friction/Traction Circle

What does the traction circle represent? Focusing on Figure 3, the two axes represent the g-forces experienced by the car as a result of tire grip in a single direction and the red circle represents the maximum g-force that the tires can produce at any direction. This means that the circle's area represents the available grip.

So how does the circle work? When the car is coasting on a straight line with constant speed then both the longitudinal and the lateral g forces equal zero and that means that we stand on the centre of the circle. When the driver accelerates then the front tires produce grip in the forward direction which results to a rearward longitudinal force and exactly the opposite happens when the driver is braking, while the lateral forces are effectively zero. When the car is turning then the tires produce side forces and thus lateral acceleration and depending on if is a right hand or a left-hand corner, a lateral acceleration in the opposite direction is experienced.

1.3.2   External forces acting on the vehicle

There are 4 types of external forces acting on a road vehicle:

1. Weight
2. Aerodynamic Force
3. Road-Tire Friction Forces
4. Road-Tire Vertical Forces

1.3.3 Aerodynamic Force

$$F_a = -D \cdot i + S \cdot j + L \cdot k$$

where D=Drag, S=Side Force and L=Lift

This force depends essentially on the vehicle's shape, size and on the relative speed Vrel between the vehicle and the air. Let's give the analytical expressions for each one of the components D, S and L:

- $D = \dfrac{1}{2} \cdot \rho_{air} \cdot V_{rel}^2 \cdot C_D \cdot A$

- $S = \dfrac{1}{2} \cdot \rho_{air} \cdot V_{rel}^2 \cdot C_s \cdot A$

- $L = \dfrac{1}{2} \cdot \rho_{air} \cdot V_{rel}^2 \cdot C_L \cdot A$

If the vehicle is running at the straight, then Cy=0 and Ya=0. A typical way of describing a car's efficiency is by directly providing the product: Sa*Cx and Sa*Cz. In general, the aerodynamic force is not applied at the C.O.G. and therefore it contributes to MG with an aerodynamic moment:

> $M_a = M_{a_x} \cdot i + M_{a_y} \cdot j + M_{a_z} \cdot k$

where M_{a_x} = rolling moment, M_{a_y} = pitching moment, M_{a_z} = yawing moment

It is common practice in motorsport racing to define the front and rear vertical forces:

$$Z_1^a = \frac{1}{l}\left[Z_a a_2 - M_{a_y} + X_a h \right] = \frac{1}{2}\rho_a V_a^2 C_{z1} S_a$$

$$Z_2^a = \frac{1}{l}\left[Z_a a_1 + M_{a,y} - X_a h \right] = \frac{1}{2}\rho_a V_a^2 C_{z2} S_a$$

1.3.4 Road-Tire Vertical Forces

The vertical load acting on a tire does affect very much its behavior [Massimo Guiggiani, 2014]. During vehicle motion, the vertical loads change whenever there are accelerations. In case of

substantial aerodynamic vertical loads, the vehicle speed also affects the vertical loads. The vertical load on each one of the vehicle's tires is given by the following equations:

$$Z_{11} = 0.5\left(Z_1^0 - Z_1^a + \Delta Z\right) - \Delta Z_1$$
$$Z_{12} = 0.5\left(Z_1^0 - Z_1^a + \Delta Z\right) + \Delta Z_1$$
$$Z_{21} = 0.5\left(Z_2^0 - Z_2^a - \Delta Z\right) - \Delta Z_2$$
$$Z_{22} = 0.5\left(Z_2^0 - Z_2^a - \Delta Z\right) + \Delta Z_2$$

Where,

1. Z_1^a and Z_2^a are the aerodynamic vertical loads which were stated before.

2. $Z_1^0 = \dfrac{mga_2}{l}$, $\quad Z_2^0 = \dfrac{mga_1}{l}$, are the static loads on the front and rear axle, respectively.

3. $\Delta Z = -\dfrac{ma_x h}{l} + \dfrac{J_{zx} r^2}{l} \square - \dfrac{ma_x h}{l}$, is the longitudinal load transfer on each axle.

4. ΔZ_1 and ΔZ_2 are the lateral load transfers.

Considering that Fz=Z then the vertical loads can be implanted into the constitutional tire forces:

$$F_{x_{ij}} = F_{x_{ij}}\left(F_{z_j}, \gamma_{ij}, \sigma_{x_{ij}}, \sigma_{y_{ij}}, \varphi_{ij}\right)$$
$$F_{yj} = F_{y_{ij}}\left(F_{z_{jj}}, \gamma_{ij}, \sigma_{x_{ij}}, \sigma_{y_{ij}}, \varphi_{ij}\right)$$

The aim is to maximize the above forces in order to help the tire work at the limit of the friction ellipse (traction circle). From the above relationships we understand that the longitudinal and lateral tire forces are proportional to the vehicle's down force.

1.3.5 Cornering Dynamics

Considering that the biggest percent of the FSAE endurance tracks consist of slow and fast corners with an average radius of 15 degrees. This gives an indication to the aerodynamicists to investigate the aerodynamic performance of the car in this kind of conditions rather than the

straights and through the optimization of the design to gain performance in the corners and thus improve the handling characteristics of the car.

The close relationship between the car's downforce and the vehicle's dynamic performance can be easily seen through the following example: If we consider the vehicle as a point, of mass m, driving along a circular path with radius r in the xy-plane, we have the maximum tangential velocity, U_{max}, as a function of grip only:

$$U_{max} = \sqrt{\frac{F_{grip}r}{m}} = \sqrt{\frac{\mu_{peak}F_z fr}{m}} = \sqrt{\frac{\mu_{peak}(gm+DF)fr}{m}}$$

where μ_{peak} is the maximum friction coefficient (for a given contact patch), F_z is the normal force exerted on the vehicle along the z axis, g is the gravitational acceleration constant, m is the vehicle's mass, DF is the total downforce produced by the vehicle, f is a function of the tire's state and finally r is the radius of the corner.

So, we understand that the cornering speed is proportional to the car's downforce and thus maximizing downforce can lead to maximization of the car's cornering speed. For the better understanding of the relationship between the aerodynamic forces and the tire forces we can pay some attention in Figure 4 and Figure 5.
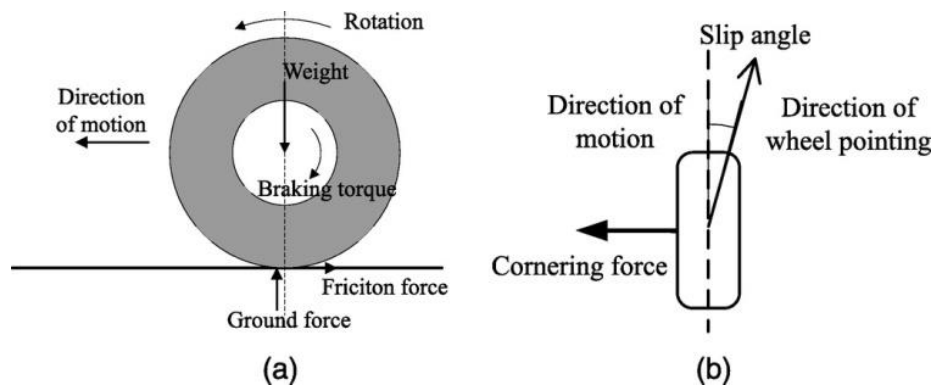
Figure 4: Longitudinal Tire Forces
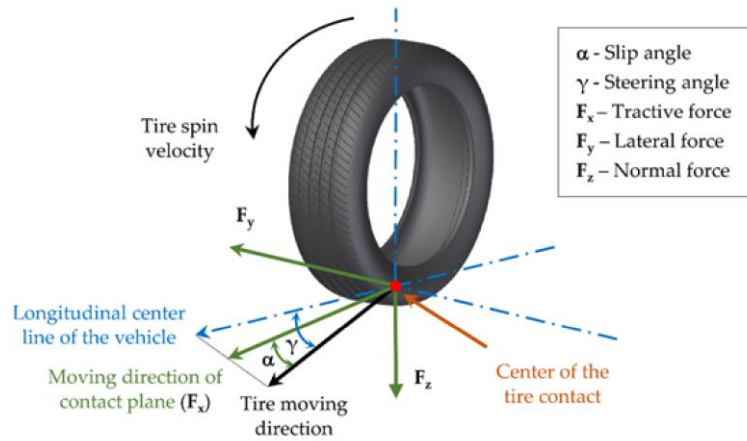
Figure 5: Lateral Tire Forces

In CFD, the cornering condition can be modeled through the creation of a curved domain and the introduction of the rotating flow in the domain. The radius of the domain can be changed depending on the curvature of the corner that we want to investigate. The cornering radius of the following study equals the radius of the skid pad track and all the different simulations were conducted using the same domain.

The track layout of the Skidpad dynamic event is the same in all the Formula Student Competitions and can be seen in Figure 6:
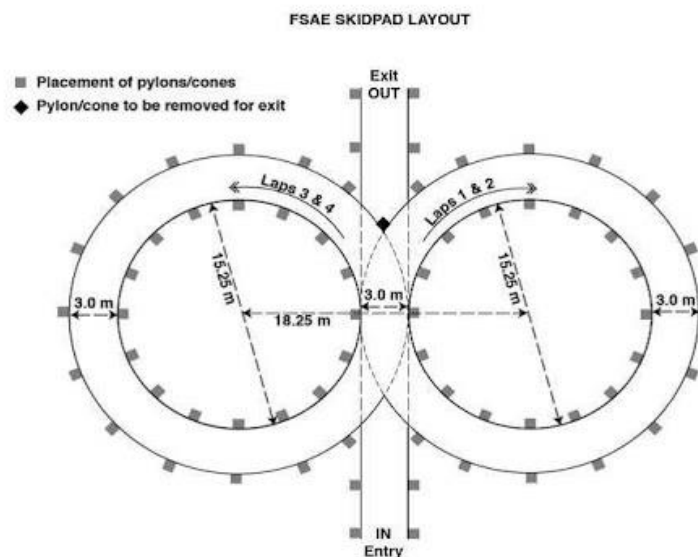
Figure 6: Skidpad Track Layout

This is done because the CFD data can be better correlated to data extracted from the track testing, when the vehicle conducts a steady state cornering condition, during the skid pad event.

1.3.6 Conclusion on the relationship between aerodynamics and vehicle dynamics

The tire specification provides the engineers with the maximum lateral and longitudinal acceleration that can be achieved from a car, using a specific set of tires. That means that the engineers who design the suspension system will provide the aerodynamicists with a down force, drag and aero balance range, in order to maximize the performance of the tires by making them work on their limit, while having a balanced-on track behavior. Someone can understand that the more downforce the better is not the case here. Instead, there is a specific range for the aerodynamicists that needs to be satisfied.

1.4 Computational Fluid Dynamics

1.4.1 Governing Equations

The flow type that we are dealing with during this study is a steady state incompressible viscous turbulent flow. Fluent solves the incompressible Navier Stokes Equations along with the turbulence model equations in order to obtain the pressure field around the car and calculate forces exerted on the car surface.

The Navier Stokes equations describe the conservation equations of mass, momentum and energy, for a conveniently selected control volume, in integral form. In many engineering problems, approximate solutions concerning the overall properties of a fluid system can be obtained by their application. This approach necessitates in general introduction of simplifying assumptions, regarding in particular the spatial distributions of the different variables and the neglect of terms that are anticipated to give a relatively small contribution to the overall balances.

The N.S. equations for an incompressible fluid with constant transport properties are the following:

Continuity equation

$$\frac{\partial u_x}{\partial x} + \frac{\partial u_y}{\partial y} + \frac{\partial u_z}{\partial z} = 0$$

Momentum equation

$$\rho\left(\frac{\partial v_x}{\partial t} + v_x\frac{\partial v_x}{\partial x} + v_y\frac{\partial v_x}{\partial y} + v_z\frac{\partial v_x}{\partial z}\right) = -\frac{\partial p}{\partial x} + \mu\left[\frac{\partial^2 v_x}{\partial x^2} + \frac{\partial^2 v_x}{\partial y^2} + \frac{\partial^2 v_x}{\partial z^2}\right] + \rho f_{m_x}$$

$$\rho\left(\frac{\partial v_y}{\partial t} + v_x\frac{\partial v_y}{\partial x} + v_y\frac{\partial v_y}{\partial y} + v_z\frac{\partial v_y}{\partial z}\right) = -\frac{\partial p}{\partial y} + \mu\left[\frac{\partial^2 v_y}{\partial x^2} + \frac{\partial^2 v_y}{\partial y^2} + \frac{\partial^2 v_y}{\partial z^2}\right] + \rho f_{m_y}$$

$$\rho\left(\frac{\partial v_z}{\partial t} + v_x\frac{\partial v_z}{\partial x} + v_y\frac{\partial v_z}{\partial y} + v_z\frac{\partial v_z}{\partial z}\right) = -\frac{\partial p}{\partial z} + \mu\left[\frac{\partial^2 v_z}{\partial x^2} + \frac{\partial^2 v_z}{\partial y^2} + \frac{\partial^2 v_z}{\partial z^2}\right] + \rho f_{m_z}$$

Energy Equation

$$\rho c\left(\frac{\partial T}{\partial t} + v_x\frac{\partial T}{\partial x} + v_y\frac{\partial T}{\partial y} + v_z\frac{\partial T}{\partial z}\right) = \phi_v + k\left[\frac{\partial^2 T}{\partial x^2} + \frac{\partial^2 T}{\partial y^2} + \frac{\partial^2 T}{\partial z^2}\right] + Q_c + Q_r$$

$$\phi_v = \mu \left[2\left(\frac{\partial v_x}{\partial x}\right)^2 + 2\left(\frac{\partial v_y}{\partial y}\right)^2 + 2\left(\frac{\partial v_z}{\partial z}\right)^2 + \left(\frac{\partial v_x}{\partial y} + \frac{\partial v_y}{\partial x}\right)^2 + \left(\frac{\partial v_x}{\partial z} + \frac{\partial v_z}{\partial x}\right)^2 + \left(\frac{\partial v_y}{\partial z} + \frac{\partial v_z}{\partial y}\right)^2 \right]$$

Since our simulation is steady state and there is no heat transfer, we understand that the velocity derivative over time in the momentum equations is eliminated and the energy equation is not even solved.

1.4.2   Turbulence models

1.4.2.1   The k-ε Model

When our flow is turbulent then the velocities are fluctuating so the only way in which we can describe the flow field, is by using the mean values. The N.S. equations are averaged using the Reynolds Decomposition method because the velocities are fluctuating. The Reynolds Decomposition helps us deal with the complexity of the turbulent flows as it suggests that all the variables can be decomposed into a basic state and a turbulent part. The general form of decomposition is given by:

$$\text{➢} \quad c = \bar{c} + c'$$

Where $\bar{c}$ refers to the basic state and c' to the turbulent part. If this method is applied to each one of the variables of our problem, then:

1. $U_x = \bar{U}_x + U'_x$

2. $U_y = \bar{U}_y + U'_y$

3. $U_z = \bar{U}_z + U'_z$

4. $p = \bar{p} + p'$

and

1. $\bar{u}_i = \frac{1}{T} \int_T^{t+T} u_i dt$

2. $\frac{1}{T} \int_T^{t+T} u'_i dt = 0$

The average of the turbulent parts for each one of the variables is zero because the variations are very short.

Substituting the above decomposed variables in the N.S. equations, they are converted into the Reynolds Averaged Navier Stokes Equations:

$$\rho\left(\frac{\partial \overline{u}}{\partial t} + \overline{u}\frac{\partial \overline{u}}{\partial x} + \overline{v}\frac{\partial \overline{u}}{\partial y} + \overline{w}\frac{\partial \overline{u}}{\partial z}\right) = F_x - \frac{\partial \overline{p}}{\partial x} + \mu\Delta\overline{u} - \rho\left(\frac{\partial \overline{u'u'}}{\partial x} + \frac{\partial \overline{u'v'}}{\partial y} + \frac{\partial \overline{u'w'}}{\partial z}\right)$$

$$\rho\left(\frac{\partial \overline{v}}{\partial t} + \overline{u}\frac{\partial \overline{v}}{\partial x} + \overline{v}\frac{\partial \overline{v}}{\partial y} + \overline{w}\frac{\partial \overline{v}}{\partial z}\right) = F_y - \frac{\partial \overline{p}}{\partial y} + \mu\Delta\overline{v} - \rho\left(\frac{\partial \overline{u'v'}}{\partial x} + \frac{\partial \overline{v'v'}}{\partial y} + \frac{\partial \overline{v'w'}}{\partial z}\right)$$

$$\rho\left(\frac{\partial \overline{w}}{\partial t} + \overline{u}\frac{\partial \overline{w}}{\partial x} + \overline{v}\frac{\partial \overline{w}}{\partial y} + \overline{w}\frac{\partial \overline{w}}{\partial z}\right) = F_z - \frac{\partial \overline{p}}{\partial z} + \mu\Delta\overline{w} - \rho\left(\frac{\partial \overline{u'w'}}{\partial x} + \frac{\partial \overline{v'w'}}{\partial y} + \frac{\partial \overline{w'w'}}{\partial z}\right)$$

The difference between the 2 is the fact that in the RANS equation a new parameter appears which is the Reynolds Stress:

$$\qquad\rhd\qquad -\rho\cdot\overline{U}'_i\cdot\overline{U}'_j$$

The most common way of solving the RANS equations is by using the Bousinesq hypothesis, which correlates Reynolds Stress to the mean velocity gradients:

$$-\rho\overline{u'_i u'_j} = \mu_t\left(\frac{\partial U_i}{\partial x_j} + \frac{\partial U_j}{\partial x_i} - \frac{2}{3}\frac{\partial U_k}{\partial x_k}\delta_{ij}\right) - \frac{2}{3}\rho k\delta_{ij}$$

When the Boussinesq hypothesis is made, all we need to do is calculate the eddy viscosity term (μ_τ). Eddy viscosity is the internal friction acting between the fluid particles which are moving randomly.

In the past the method that was used in order to calculate the eddy viscosity was the mixing length (l_m) approach:

$$\qquad\rhd\qquad \mu_\tau = \rho\cdot\sqrt{k}\cdot l_m \qquad \text{or} \qquad \mu_\tau = \rho\cdot l_m^{\,2}\cdot\left|\frac{\theta U}{\theta y}\right|$$

The approach was introduced by Prandtl and it suggests that $l_m = k\cdot y$ where k=0.41. It is easily understood that the mixing length is proportional to the distance from the wall. The

physical meaning of the mixing length is that it indicates the size of the turbulent eddies that exist in the flow. That means that in the regions where a lot of kinetic energy (turbulence) exists, the mixing length is going to be large and so does the eddy viscosity.

Figure 7: Eddies Detection

According to Van Driest mixing model, the viscosity in the viscous sub-layer dampens the eddies and reduces their size, so according to Driest the following model describes the damping:

$$l_m = \kappa y \left[1 - \exp\left(-\frac{y^+}{A^+} \right) \right]$$
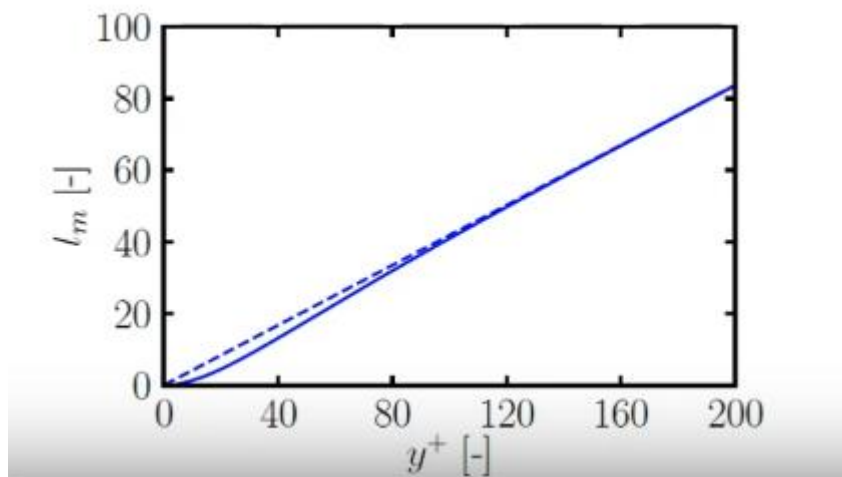
Figure 8: Mixing length vs y+

Now it is better proved that the mixing length depends only on the distance from the wall.

We can also calculate the mixing length from the turbulence dissipation rate:

$$\triangleright \quad l_m = \frac{C_\mu \cdot k^{\frac{3}{2}}}{\varepsilon}$$

The transport equation for k is the same in all the k-ε type models:

$$\underbrace{\frac{\partial(\rho k)}{\partial t}}_{\{\text{Time}\}} + \underbrace{\nabla \cdot (\rho U k)}_{\{\text{Convection}\}} = \underbrace{\nabla \cdot \left[\left(\mu + \frac{\mu_t}{\sigma_k} \right) \nabla k \right]}_{\{\text{Diffusion}\}} + \underbrace{P_k + P_b - \rho \grave{o} + S_k}_{\{\text{Sources+ sinks}\}}$$

The transport equation of ε [Launder and Sharma,1974]is given by:

$$\underbrace{\frac{\partial(\rho \grave{o})}{\partial t}}_{\{\text{Time}\}} + \underbrace{\nabla \cdot (\rho U \grave{o})}_{\{\text{Convection}\}} = \underbrace{\nabla \cdot \left[\left(\mu + \frac{\mu_t}{\sigma_{\grave{o}}} \right) \nabla \grave{o} \right]}_{\{\text{Diffusion}\}} + \underbrace{C_1 \frac{\grave{o}}{k} \left(P_k + C_3 P_b \right) - C_2 \rho \frac{\grave{o}^2}{k} + S_{\grave{o}}}_{\{\text{Sources}+sinks\}}$$

This equation varies between the k-ε models due to the different C_1, C_2, C_3 values that are used. Once the transport equations for k and ε are solved then we can calculate μt.

1.4.2.2 Model Coefficients

The most recent values according to [Launder and Sharma, 1974] are:

$$\triangleright \quad \sigma_\kappa = 1, \sigma_\varepsilon = 1.3, C_1 = 1.44, C_2 = 1.92, C_\mu = 0.09$$

What happens with the k-ε model, is that instead of solving the mixing length, we are solving for the dissipation rate ε. The physical meaning of ε is that it expresses the rate at which turbulent kinetic energy is converted into thermal internal energy. In the case of the mixing length, the length was damped close to the wall to account for viscosity effects that take place in the viscous sub-layer and reduce the effective size of the eddies and therefore the strength of dissipation rate that they introduce. Since there is no mixing length, ε, must be damped close to the wall. For this reason, empirical damping functions are applied. So C_1, C_2, C_3 are the coefficients that are damped from the damping functions: f_1, f_2, f_μ respectively. This is a low Reynolds formulation, and the equations can be applied in the viscous sub-layer. Practically this means that in CFD code is that we can solve our equations even when our computational cells are in the viscous sub-layer. What the empirical function are doing is that they reduce the dissipation rate close to the wall and that exactly is the physical explanation of the damping. The damping functions of the Standard k-εmodel are:

1. $f_1 = 1$

2. $f_2 = 1 - 0.3 \cdot e^{-\text{Re}_T^{\,2}}$

3. $f_\mu = e^{\frac{-3.4}{(1+\text{Re}_T^{\,2}/50)^2}}$

where Re_T is given by:

$$\blacktriangleright \quad \text{Re}_T = \frac{Turbulent\ Forces}{Viscous\ Forces} = \frac{\rho \cdot \sqrt{k} \cdot l_m}{\mu}$$

and expresses the strength of the near wall turbulence, relative to viscosity. When Re_T is small then viscous effects dominate the flow in that region.

1.4.2.3 The k-ω SST model

In this model the transport equation for k is the same with the k-e but in order to obtain the transport equation of ω we substitute $\varepsilon = C_\mu \cdot k \cdot \omega$ the transport equation of ε, so we get:

$$\frac{\partial(\rho\omega)}{\partial t} + \nabla \cdot (\rho \boldsymbol{U} \omega) = \nabla \cdot \left(\left(\mu + \frac{\mu_t}{\sigma_k} \right) \nabla\omega \right) + \frac{\gamma}{v_t} P_k - \beta\rho\omega^2 + \underbrace{2\frac{\rho\sigma_{\omega 2}}{\omega}\nabla k : \nabla\omega}_{\text{Additional Term}}$$

Both the ω (specific dissipation rate) and the εrepresent the same physical quantity and that is the turbulence dissipation rate.

The above underlined additional term exists in the k-e, but in the k-ω it is eliminated.

$$\frac{\partial(\rho\omega)}{\partial t} + \nabla \cdot (\rho \boldsymbol{U} \omega) = \nabla \cdot \left(\left(\mu + \frac{\mu_t}{\sigma_k} \right) \nabla\omega \right) + \frac{\gamma}{v_t} P_k - \beta\rho\omega^2$$

if we multiply the additional term with the so-called blending factor: $(1- F_1)$ then we can blend between the models since $F_1 = 0$ for k-ε and $F_1 = 1$ for k-ω. The way the blending function works in CFD is presented in Figure 9.
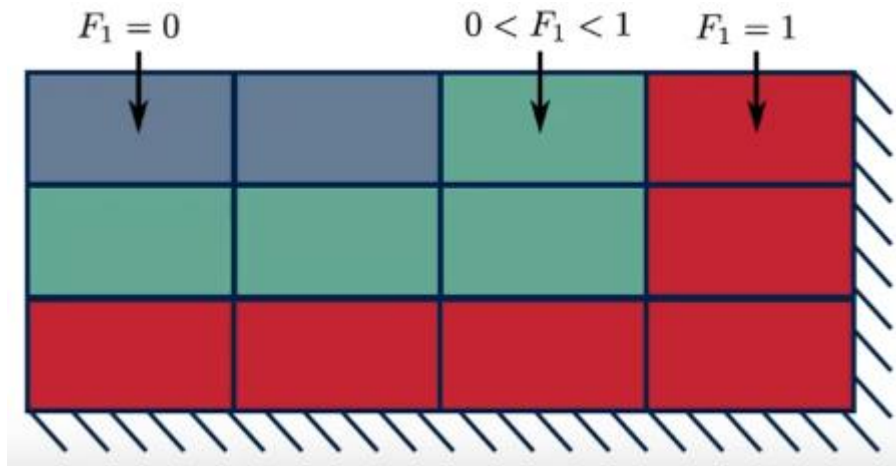
Figure 9: Blending function application.

The analytical expression for F_1 is given by:

> $F_1 = \tanh(\arg_1^h)$
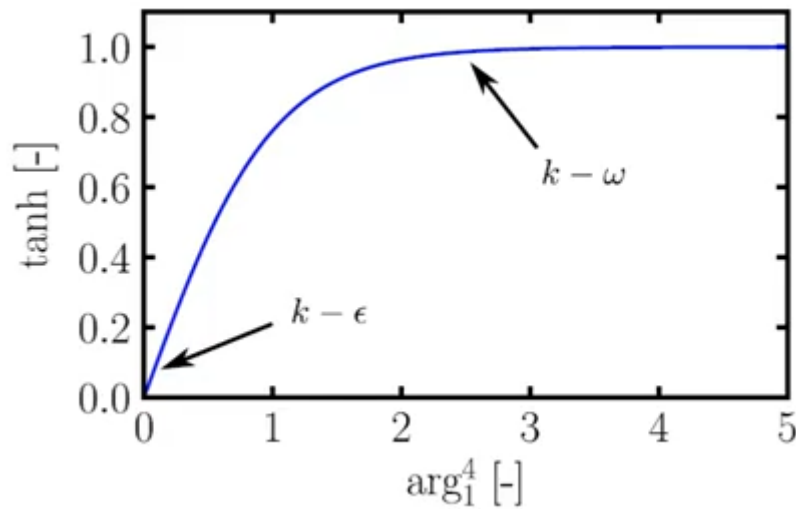
Figure 10: $\tanh$ vs $\arg_1^4$

$\arg_1^4$ depends on the distance to the closest wall (d):

> $$\arg_1 = \min\left[\max\left(\frac{\sqrt{k}}{\beta \cdot \omega \cdot d}, \frac{500 \cdot v}{d^2 \cdot \omega}\right), \frac{4 \cdot \rho \cdot \sigma_{\omega_2} \cdot k}{C \cdot D_{k\omega} \cdot d^2}\right]$$

The blending function is given by:

$$\blacktriangleright \quad \varphi = F_1 \cdot \varphi_\omega + (1 - F_1) \cdot \varphi_\varepsilon \Rightarrow \varphi = F_1 \cdot \beta^* + (1 - F_1) \cdot C_\mu$$

The blending function gives the BST model, so what is the difference of the SST model. The difference is that in the second model there is one extra factor included, the viscosity limiter:

$$\blacktriangleright \quad \mu_\tau = \frac{\rho \cdot k}{\omega} \quad \text{(original)}$$

$$\blacktriangleright \quad \mu_\tau = \frac{\alpha_1 \cdot \rho \cdot k}{\max(\alpha_1 \cdot \omega, SF_2)} \quad \text{(SST model)}$$

This limiter results in better agreement with experimental measurements of a separated flow. F_2 is another blending function similar to F_1. If F_2 or S is large, then the viscosity is reduced. F_2 is given by:

$$\blacktriangleright \quad F_2 = \tanh(\text{arg}_2^2)$$

$$\blacktriangleright \quad \text{arg}_2 = \max\left(\frac{\sqrt{k}}{\beta \cdot \omega \cdot d}, \frac{500 \cdot v}{d^2 \cdot \omega} \right)$$

where d is the distance cell center closest to the wall.

The k-ω SST gives better agreement with experiments of mildly separated flows. This happens due to the viscosity limiter. It is appropriate for external aerodynamics or generally simulations where separation is important.

1.4.3 Boundary layer Treatment and Wall functions

What are the wall functions and why are they needed? Experimental and numerical simulations inside a flat plate tube were conducted in order to define the relationship between the tangential velocity and the distance from the surface:
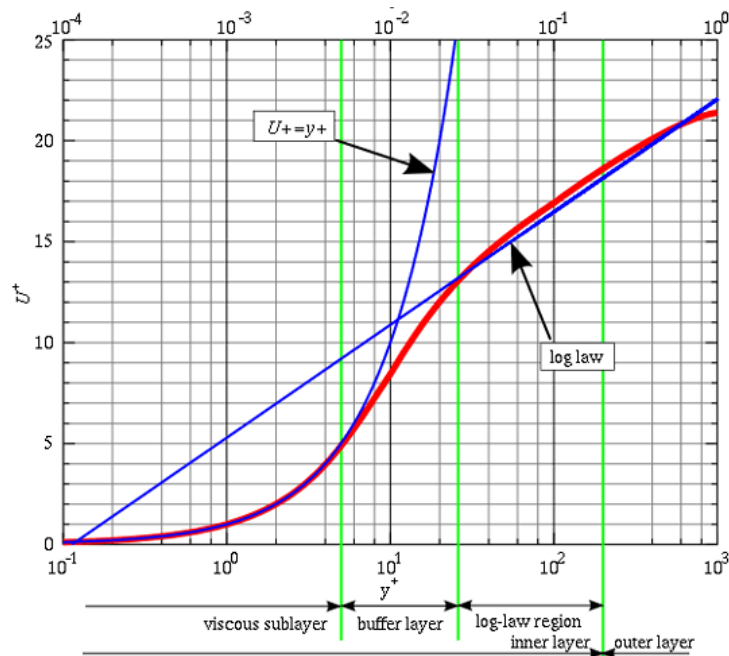
Figure 11: Relationship between U^+ and y^+

The standard wall functions are two [ANSYS Fluent 12.0 User Guide, Standard Wall Function], one for the viscous sub-layer and one for log law region:

$$\triangleright \quad U^+ = y^+ \ , \ y^+ < 5 \ \text{(viscous sub-layer)}$$

$$\triangleright \quad U^+ = \frac{1}{k} \cdot \log\left(E \cdot y^+\right) \ , \ 30 < y^+ < 200 \ \text{(log law)}$$

where k = 0.4187 and E = 9.793

$$\triangleright \quad y^+ = \frac{y \cdot u_\mathrm{T}}{v}$$

$$\triangleright \quad U^+ = \frac{U}{u_T}$$

u_T is a reference velocity based on the wall shear stress: $u_T = \sqrt{\dfrac{\tau_w}{\rho}}$

CFD codes do not recommend placing the cells in the buffer layer. What exactly does the CFD code do near the wall? Near the wall the velocity is zero, due to the no slip condition and the velocity at the cell's centroid (Up) is calculated from momentum equations. What needs to be calculated is the gradient and the wall shear stress. Through the shear stress integration, total drag will be calculated.

According to Figure 11, if the variation of the velocity across the cell is linear, that means that the cell is placed in the viscous sub layer, then the wall shear stress is:

$$\blacktriangleright \quad \tau_w = v \cdot \left(\frac{\theta U}{\theta y} \right)_{y=o} = v \cdot \left(\frac{U_p - 0}{y_p} \right) = v \cdot \frac{U_p}{y_p}$$

On the other hand, if the variation is non-linear, then that means that our cell is placed in the log-law region, so the wall shear stress is estimated by:

$$\blacktriangleright \quad \tau_w = v \cdot \left(\frac{\theta U}{\theta y} \right)_{y=o} = \frac{u_t \cdot U_p}{\frac{1}{k} \cdot \log(E \cdot y^+)}$$

The data from the universal tangential velocity profile plot were extracted from a plane parallel flow, where there was no separation, no curvature and no pressure gradients and so it is understood that it does not apply the same way in all types of flows, but it can be used as a reference point.

1.4.4 Mesh Refinement

In order the engineer to ensure that the wall shear stress is calculated correctly, a target of $y^+ < 5$ or $30 < y^+ < 200$ must be set in order to help the code choose, which model to adopt concerning the velocity profile behavior between the cell centroid and the wall. In Figure 12 the purple and the blue lines are the two models adopted by the code depending on the region in order to approach the experimental behavior. Another expression for the y+ is following:

$$\blacktriangleright \quad y+ = \frac{\rho \cdot u_T \cdot y_p}{\mu} \text{ and } u_T = \sqrt{\frac{\tau_w}{\rho}} \text{, unknown: } \tau_w$$

where y_p, is the smallest distance between the first cell centroid and the wall's surface. The relationship can be easily understood by the following figure:
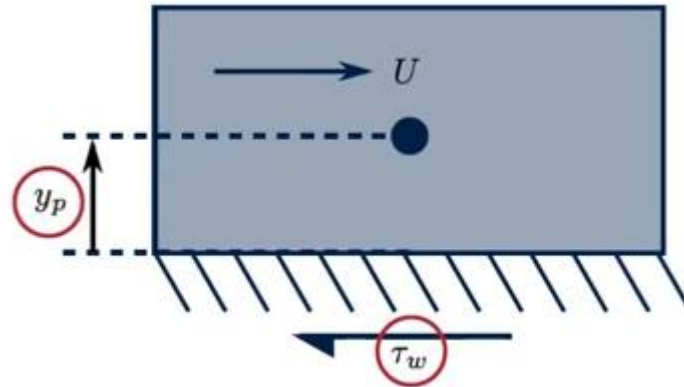
Figure 12: First cell height representation

The main problem here is how small should y_p be? The answer is that this is going to be done through trial and error. Before starting a CFD simulation we do not know the value of y+, so we have to target it in order to create the boundary layer discretization. After using an initial value then we should run an indicative simulation and then plot the y+ in the post processor to see what value we get for y+. If the value is much larger than the one chosen at the start then the mesh should be refined, meaning that we should use a smaller value for y_p in order to create the mesh.

How to make an initial guess for y_p [Introduction to ANSYS Fluent, Lecture 7]?

1. Calculate the Re number, using for L the car's length.

2. Calculate the friction coefficient by: $C_f = \left[2\log_{10}(\text{Re}) - 6.5\right]^{-2.3}$ or estimated from a plot for a fully turbulent boundary layer.

3. Use C_f to calculate wall shear stress by: $\tau_w = \left(\frac{1}{2} \cdot \rho \cdot U^2\right) \cdot C_f$

4. Then calculate friction velocity by: $u_T = \sqrt{\dfrac{\tau_w}{\rho}}$

5. Then rearrange the y+ expression for y_p: $y_p = \dfrac{y^+ \cdot \mu}{\rho \cdot u_T}$

6. The first layer height is calculated by: $flh = 2 \cdot y_p$

The conclusion is that after we make an initial estimation for the y_p and thus for the first layer height, using a target y+, then we solve using the appropriate wall function and by the end of simulation we use the post processor to plot the value of y+. If this value is larger than the one targeted or if it is smaller, then refinement it or coarsening must occur, respectively.

1.4.5   Discretization Schemes

The role of a discretization scheme is to convert a differential equation to an algebraic form. Fluent gives the user the chance to choose among several schemes but we are only going to talk about the scheme that we are applying in our simulations. The type of discretization is upwind differencing and both first order and second order upwind schemes are available, but we are using second order straight away in order to have better accuracy. The convection term creates a diagonally equal matrix only for Upwind Differencing. Any other differencing scheme will create negative coefficients, violate the diagonal equality and potentially create unbounded solution [Jasak,1996]. So, even though the upwind differencing is not accurate, it is the most stable scheme for convection dominated flows, so we use it in order to generate an initial stable solution.

Upwind differencing depends on the direction of the mass flux:

$$\text{➤} \quad F_f = \rho_f \cdot A_f \cdot (U_f \cdot \hat{n})$$

where,

$$\text{➤} \quad F_f > 0 \text{, mass flow out of the cell}$$

$$\text{➤} \quad F_f < 0 \text{, mass flow into the cell}$$

An example of second order upwind differencing scheme is the following:

$$\text{➤} \quad u_x = \frac{3u_i{}^n - 4u_{i-1}{}^n + u_{i-2}{}^n}{2\Delta x}$$

1.4.6 Solving Algorithms

Fluent contains a variety of solving algorithms but we are going to analyze the algorithm that is used in our study and that is the SIMPLE algorithm (1972). The acronym SIMPLE stand for Semi Implicit Method for Pressure-Linked equations [Versteeg and Malalasekera, 1995]. The Navier Stokes equations were stated before and consist of 4 equations with 4 unknowns (U_x, U_y, U_z, p). The problem here is that we have 3 equations for (U_x, U_y, U_z), but we have no equation for p. The computed velocity fields (U_x, U_y, U_z), must satisfy the continuity equation. The convection term in the momentum equation is non-linear and we cannot use the ideal gas law in order to calculate the pressure, since density and temperature are constant.

The tools of the SIMPLE algorithm which solve the N.S. equations are:
1. Derive an equation for pressure from the momentum and continuity equations.
2. Derive a corrector for the velocity field, so that it satisfies the continuity equation.

Solving steps of SIMPLE algorithm
1. The first step of the solver is to express the momentum equations in the general matrix:

$$\succ \quad M \cdot U = -\nabla p$$

With M being the matrix of the coefficients that are products of the discretization method, used for converting the momentum equations into an algebraic form. The coefficients are all known. If we consider the x component, then we have:

$$
\begin{pmatrix}
M_{11}M_{12}.....M_{1n} \\
M_{21} \\
M_{31} \\
. \\
. \\
M_{n1}
\end{pmatrix}
\cdot
\begin{pmatrix}
U_1 \\
U_2 \\
U_3 \\
. \\
. \\
U_n
\end{pmatrix}
=
\begin{pmatrix}
\left(\dfrac{\theta p}{\theta x}\right)_1 \\
\left(\dfrac{\theta p}{\theta x}\right)_2 \\
\left(\dfrac{\theta p}{\theta x}\right)_3 \\
. \\
. \\
\left(\dfrac{\theta p}{\theta x}\right)_n
\end{pmatrix}
$$

There are n equations one for each cell centroid.

2. The second step is to separate the matrix M into diagonal and off diagonal components:

    $$\succ \quad M \cdot U = -\nabla\rho \Rightarrow AU - H = -\nabla\rho$$

3. The third step is to invert the diagonal matrix A into A^{-1}

4. The fourth step is to combine the previous relations and create matrix H.

5. By rearranging the momentum equation and substituting into the continuity equation we get, the pressure equation, which is called Poisson eq.:

    $$\succ \quad AU - H = -\nabla p \Rightarrow U = A^{-1} \cdot H - A^{-1} \cdot \nabla p$$

    $$\succ \quad \nabla U = 0 \Rightarrow \nabla \cdot \left[A^{-1} \cdot H - A^{-1} \cdot \nabla p \right] = 0 \Rightarrow \nabla \cdot \left[A^{-1} \cdot \nabla p \right] = \nabla \cdot \left[A^{-1} \cdot H \right]$$

6. Now we have 4 equations with 4 unknowns.

7. Solution Process:

    i.   The momentum equations are solved first.

    ii. Secondly the Poisson equation for pressure is solved.

    iii. Then the pressure field is used to correct the velocity in order to satisfy the continuity equation.

    iv. If the continuity equation is not satisfied the cycle is repeated.

    v.   If there is turbulence model the transport equations for its variables are solved after the velocity correction and before the continuity equation check.

The SIMPLE algorithm is pressure based and, as we solve a Poisson equation for pressure. If the flow is non isothermal, then density is calculated from an equation of state: $\rho = \dfrac{p}{RT}$. The difference with a density-based solver is that the density is calculated from the continuity equation and the pressure is drawn from the state equation: $p = \rho \cdot R \cdot T$.

1.4.7   Relaxation Factors – Iterative Method

The method which is used from Fluent in order to solve matrices from the discretized N.S. and turbulence model equations, in order to obtain the values for the pressure (p), the velocity components (Ux, Uy, Uz), the turbulent kinetic energy (k) and dissipation rate (ε) at every cell centroid of the discretized control volume, is the Successive Under Relaxation Method (S.U.R.)

which as someone will understand from the following example is a specific case of the S.O.R. method which by itself is a variant of the Gauss Seidel method.

The S.O.R. method was devised simultaneously by David M. Young, Jr. and by Stanley P. Frankel in 1950 for the purpose of automatically solving linear systems on digital computers [Hadjidimos, 1997]. The advantage of this method is the fact that calculating the optimal relaxation factor (ω) value, one can lead the system to a much faster convergence than the Gauss Seidel method. The advantage can be seen by the following example:

Consider a square system of n linear equations with unknown **x**, where in our case n depends on the number of the volume mesh elements and the unknowns are p, Ux, Uy, Uz, k, e:

Ax=B

$$A = \begin{bmatrix} a_{11} & a_{12} & \cdots & a_{1n} \\ a_{21} & a_{22} & \cdots & a_{2n} \\ \vdots & \vdots & \ddots & \vdots \\ a_{n1} & a_{n2} & \cdots & a_{nn} \end{bmatrix}, \quad \mathbf{x} = \begin{bmatrix} x_1 \\ x_2 \\ \vdots \\ x_n \end{bmatrix}, \quad \mathbf{b} = \begin{bmatrix} b_1 \\ b_2 \\ \vdots \\ b_n \end{bmatrix}$$

According to the S.O.R. method the above system can be solved by the following equation:

$$x_i^{(k+1)} = (1-\omega)x_i^{(k)} + \frac{\omega}{a_{ii}} \left(b_i - \sum_{j<i} a_{ij} x_j^{(k+1)} - \sum_{j>i} a_{ij} x_j^{(k)} \right), \quad i = 1,2,\ldots,n$$

where k is the number of the iteration and ω the relaxation factor

In 1947, Ostrowski proved that if A is symmetric and positive definite matrix then the S.O.R. method converges when the spectral radius of the iteration matrix is smaller than 1, for the following values of ω:

$$\rho(C_\omega) < 1, \text{ when } 0 < \omega < 2$$

where C_ω is the iteration matrix given by: $C_\omega = I - D^{-1} \cdot A$

At this point it need to be mentioned that the S.U.R. is applied when the relaxation factor lies between $0 < \omega < 1$ and that for ω=1 we get the Gauss Seidel method.

What really matters in our case is not just the convergence but which value of ω between 0 and 1 will give the fastest convergence. With respect to the theory the optimal ω can be calculated by:

$$\omega_{opt} := 1 + \left(\frac{\mu}{1 + \sqrt{1 - \mu^2}} \right)^2$$

where μ is the spectral radius of the iteration matrix C_ω.

The problem is that using the Fluent solver, the user is not able obtain the iteration matrix which makes it impossible for him to calculate the optimal relaxation factor using the above simple equation. That means that the user must conduct simulations using different ω values for each one of the variables solved in his problem and obtain those which not only give the fastest convergence but also the convergence that leads to a meaningful result.

1.4.8   Solution Residuals

After the discretization of the conservation equation of a variable φ, inside a cell P, the equation can be written in the following form:

$$\blacktriangleright \quad a_p \cdot \varphi_p = \sum_{nb=1}^{N} a_{nb} \cdot \varphi_{nb} + b$$

where a_{nb} are the influence coefficients of the neighboring cells, b is the contribution of the constant part of the source term S_c and of the boundary conditions.

The residuals R^φ: $R^c, R^{ux}, R^{uy}, R^{uz}, R^k, R^\varepsilon$ are calculated from the pressure-based algorithm and equal the sum of the equation's (1) imbalance, computed in each one of the computational cells:

$$\blacktriangleright \quad R^\varphi = \sum_{t=1}^{P} \left| \sum_{nb=1}^{N} a_{nb} \cdot \varphi_{nb} + b - a_p \cdot \varphi_p \right|$$

where P is the total number of elements/cells and N is the number of the neighboring cells of a cell's centroid, on which equation (1) is calculated.

Bearing in mind the previous equation, we cannot understand whether our solution has converged or not. For this reason, fluent scales R^φ using a scaling factor which represents the whole flow inside the control volume. The normalized residual is the one that we see on the solution monitor for all the 6 equations, solved. It is written as:

$$\blacktriangleright \quad R^{\varphi} = \frac{\sum\limits_{t=1}^{P} \left| \sum\limits_{nb=1}^{N} a_{nb} \cdot \varphi_{nb} + b - a_p \cdot \varphi_p \right|}{\sum\limits_{i=1}^{P} a_p \cdot \varphi_p}$$

Now a closer look should be taken concerning the continuity equation since both the definition and the normalization of the residual differs from the ones that were stated above.

The residual of the continuity equation is stated as:

$$\blacktriangleright \quad R^c = \sum_{t=1}^{N} \left| \text{rate of mass creation in cell centroid P} \right|$$

with N being the total number of elements/cell centroids.

The normalized expression is:

$$\blacktriangleright \quad R^c = \frac{R_N^C}{R_5^C}$$

here N symbolizes the number of iterations. As we understand the continuity eq. residual is normalized using the maximum absolute residual value of the first 5 iterations. The program gives the option to the user to change that, for example to use the maximum residual values of the first 50 iterations as a scaling factor.

1.4.9   Mesh Type and Quality Criteria

In this section we will discuss about the importance of the grid generation (meshing) in the CFD, the typical cell shapes and the meshing quality criteria.

The grid or mesh discretizes the geometry of the problem and designates the cells or elements on which the flow is solved. It can have a significant impact on the rate of convergence, in the accuracy of the solution and the CPU time required, depending on the size and the quality of the grid. The difference between the elements and the cells is the fact that the first are used for the discretization of surfaces (2D) and the second for the discretization of control volumes (3D). Typical element shapes are the triangles ("trias") which are transformed into tetrahedron ("tetras") and /or pyramid cells or even polyhedrons, in 3D problems, and the 2D prisms which are transformed into hexahedron ("hexas") cells or wedges. The element and the cell types available are shown in Figure 13 and Figure 14 respectively.
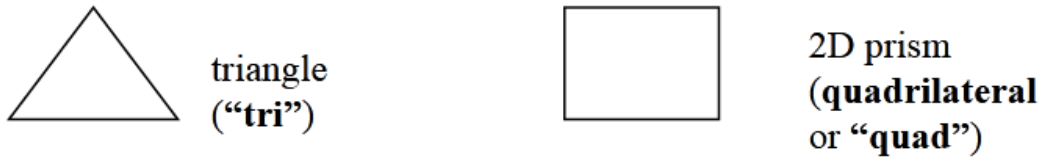
Figure 13: Element Types
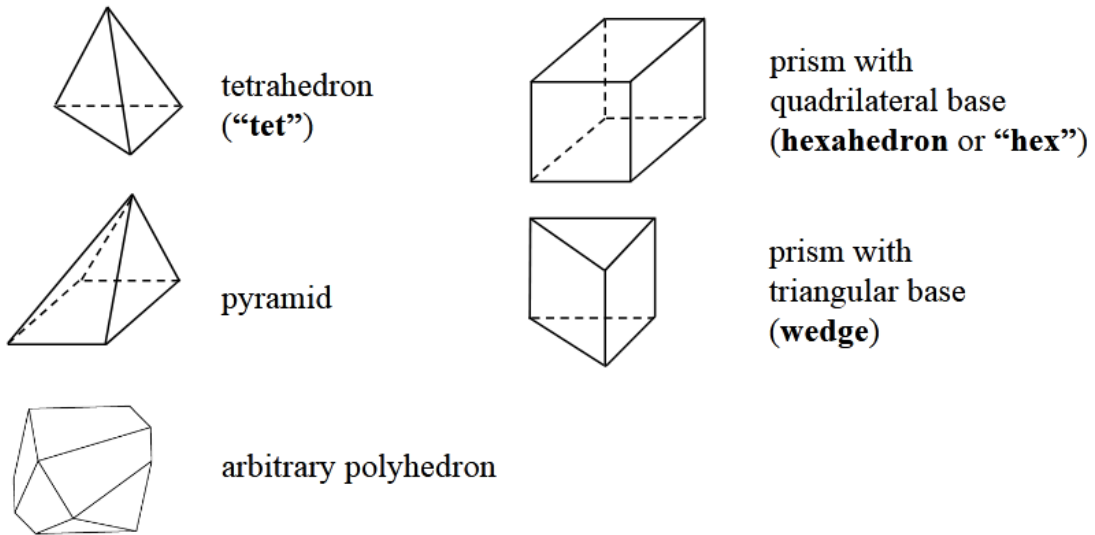
Figure 14: Cell Types

There is also the possibility of generating a hybrid mesh which consists of 2 or more different cell types. The element and cell types that will be chosen by an engineer, depend on the complexity of the simulated geometry. If the geometry is very complex, then triangles are most commonly used, as they can discretize the geometry without deforming it.

Finally, grids are also separated into two bigger categories: the structured and the unstructured grids which is also very much geometry dependable. The difference between the two is that in a structured mesh the all the elements have a regular connectivity (see Figure 15) and in an unstructured mesh irregular connectivity (see Figure 16), so it is easily understood that structured meshes are impossible to be applied in complex geometries.
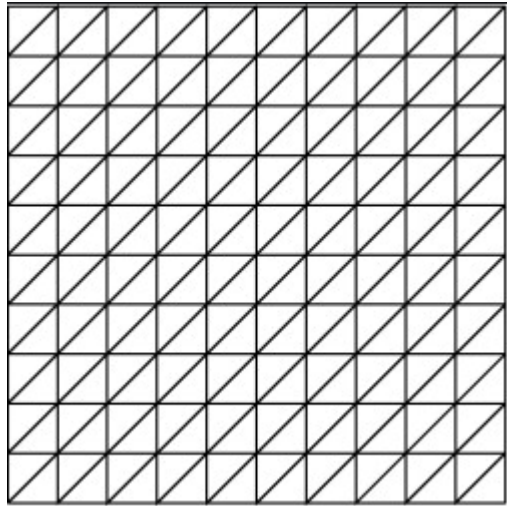
Figure 15: Structured Grid
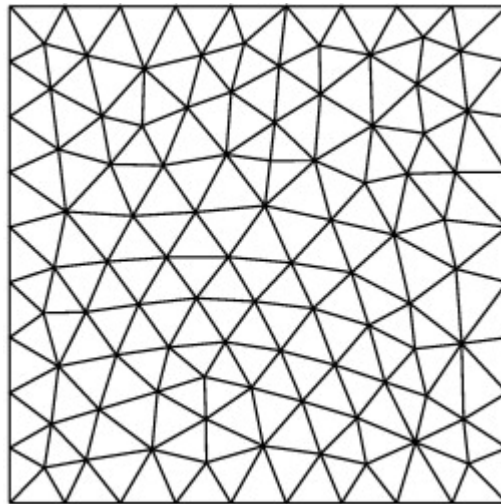
Figure 16: Unstructured Grid

As far as the mesh quality is concerned, 3 criteria will be analyzed:

1. Skewness
2. Cell Squish
3. Aspect Ratio

The skewness criterion shows the difference percentage between the area of an element and the area of the equilateral triangle which is registered to the same circle as the element (see Figure 17). The equilateral triangle is referred as the optimal triangle. The skewness equation is given by:

$$\text{Skewness} = \frac{A_{optimal} - A_{element}}{A_{optimal}}$$
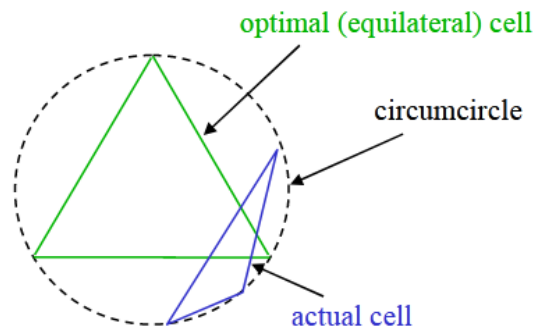
Figure 17: Element Skewness

Table 1: Mesh skewness quality

Skewness Range	0 - 0,25	0,25 - 0,5	0,5 - 0,8	0,8 - 0,95	0,95 - 0,99	0,99 - 1
Cell Quality	excellent	good	acceptable	poor	sliver	degenerate

Cell squish is the quantification of a cell's orthogonality with respect to its areas:

$$\text{Cell Squish} = \frac{1 - A \cdot r_c}{r_c}$$

where A is the area of each one of the cell's sides and r_c the respective distance of the side from the cell's centroid.

Finally, the aspect ratio is a criterion that shows how much stretched a cell is:
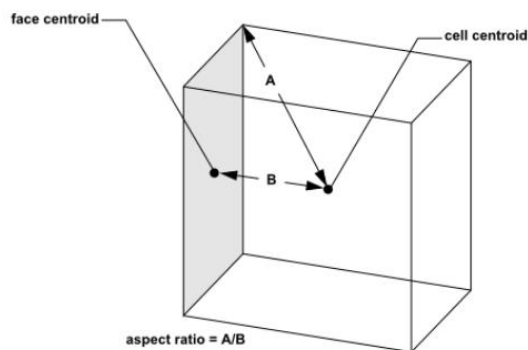
Figure 18: Aspect Ratio

The computation of the aspect ratio of a tetrahedral cell is completed in the same way.

The main sources of error in computational fluid dynamics [Bakker, 2002] are:

1. Mesh too coarse
2. High skewness
3. Large jumps in volume between adjacent cells
4. Large aspect ratios
5. Interpolation errors at non-conformal interfaces.
6. Inappropriate boundary layer mesh.

All the above factors should be taken into consideration before choosing the grid with which the simulations will be conducted. For this reason, before proceeding with the final simulations we had to conduct a mesh independency study and a boundary layer modeling study which will further analyzed in the numerical part.

1.5 Experimental Fluid Dynamics

1.5.1 General Information

All the experiments were conducted in the Laboratory of Fluid Mechanics and Turbo machinery, in the Department of Mechanical Engineering at the University of Thessaly.

The experiment analysis explains both the way the measurements were done but also the equipment's functionality and the data acquisition procedures.

1.5.2 Wind Tunnel Testing Limitations

The two main limitations of wind tunnel testing are:

a. Blockage Ratio
b. Boundary Layer Displacement Thickness Disturbance

Blockage ratio is a parameter carried over from aircraft terminology and describes the ratio of the car's frontal area to the wind tunnel's cross-sectional area. For road vehicles this ratio can be extremely large compared to an aircraft, but this is not the case when we are studying scaled race car geometries.

The wind tunnel which was utilized for this study is open return with a closed test section. This means that wind tunnel test section is of a restricted volume, so the aerodynamic measurements obtained from the wind tunnel tests, do not resemble to that of those obtained in infinitely

spaced boundaries, such as the case of a vehicle moving on a plane road [Sahini, 2004]. In contrast to open test sections, the streamline divergence around a model is less than that in an infinite stream. This causes the measured values of CD to be larger than those in an infinite stream, rather than smaller, and the magnitude of the discrepancy is significantly greater than that for open test sections [Hucho, Wong and Sovran, 1993].

The blockage effect can be divided into three components. Solid blockage, and wake blockage which cause flow speed to increase near the body and boundary induced wake related increment in wind axis drag [Sahini, 2004]. Solid blockage is the blockage, which is the characteristic of the blockage volume and the wake bubble created next to it. The flow speed in this region of the wind tunnel test section increases relatively with respect to the free stream velocity. The pressure decreases with respect to the initial entry pressure. The pressure gradient produced due to the wake source that acts on the model volume, is the reason for the wake-induced drag increment. For this reason, significant research has been done in order to determine the blockage corrections for different blockages of specific models and correct the values of the drag. Such studies also specified a limit at which the blockage ratio of a certain geometry was acceptable.

For a long period, a blockage ratio around 5% was said to be acceptable for the aerodynamic testing of cars, but this is still doubtful since 20% blockage ratios are also used in the automotive industry, bearing in mind cooling test experiments [Hucho, Wong and Sovran, 1993]. Katz also presents experimental data from wind tunnel tests with rather high blockage. Bearing in mind [Barlow, J. B., Rae, W. H., Pope, A., 1999] research, an investigation of wind tunnel wall effects in high blockage testing was done. Four different bluff bodies with a blockage range from 5% to 20% were measured both in a wind tunnel and numerically. It was concluded that as the blockage ratio increases, some effects may become quite significant and simple corrections cannot work efficiently for all the changes. When dealing with blockage values around 7% or even 10%, some of the traditional corrections can be applied since the effects are not very large.

In another paper co-written by Katz, a 25% scaled model of a generic Indy Car formula is tested in a wind tunnel. During the tests both the wheels and the ground plane were kept stationary. The blockage in these experiments was large 15% and use of numerical corrections were introduced. With this experimental set up certain differences were stressed out, but it was proved that such tests can be used for basic studies and thus yield useful aerodynamic data.

What should be done is an evaluation of the blockage and then a conclusion on whether that affects the free stream velocity establishment, by measuring the free stream velocity for a given wind tunnel speed, with and without the test model. If the velocity is affected, then a decision should be made on whether this influence is acceptable or not and so, a blockage correction technique should be applied. It would also help us specify an upper limit of blockage ratio for this specific wind tunnel.

Concerning the boundary layer's influence, another test should be done before proceeding with our main experiments. Based on wind tunnel theory if the displacement thickness of the boundary layer is less than 10% of the vehicle's ground clearance, then this way of representing the road using the floor of the test section and fixing the car above it with non- rotating wheels (due to equipment restrictions), should be acceptable[Hucho, Wong and Sovran, 1993]. So, what we had to do was to measure the velocities from the very low point of the tunnel's floor till a height relative to 50% of our test models height, using a relatively small step. These measurements should be taken without the test model placed in the wind tunnel. After collecting the data, we should observe up until which height the velocity is affected (smaller than the actual free stream velocity) and since that height is below the 10% of our test model's ground clearance, then this method could be applicable.

Both experiments and their results are analyzed in the experimental analysis section below.

1.5.3   Anemometry Measurements

The principal on which hot-wire anemometry is based on the convective heat transfer from a heated wire [Jorgensen, 2002]. There are two types of hot wire anemometer methods for calculating velocity: a) the constant current method b) constant temperature method. Hot wire anemometers use a very thin wire alloy made of tungsten (on the order of several micrometers), electrically heated to some temperature above the ambient. The air flowing past the wire cools the wire. As the electrical resistance of most metals depends upon the temperature of the metal, a relationship can be obtained between the resistance of the wire and the flow speed. In most cases, they cannot be used to measure wind direction, unless coupled with a wind vane. There are two implementations: constant current and the constant temperature. Concerning the constant current method, Figure 19 could be helpful on the understanding of its functionality:
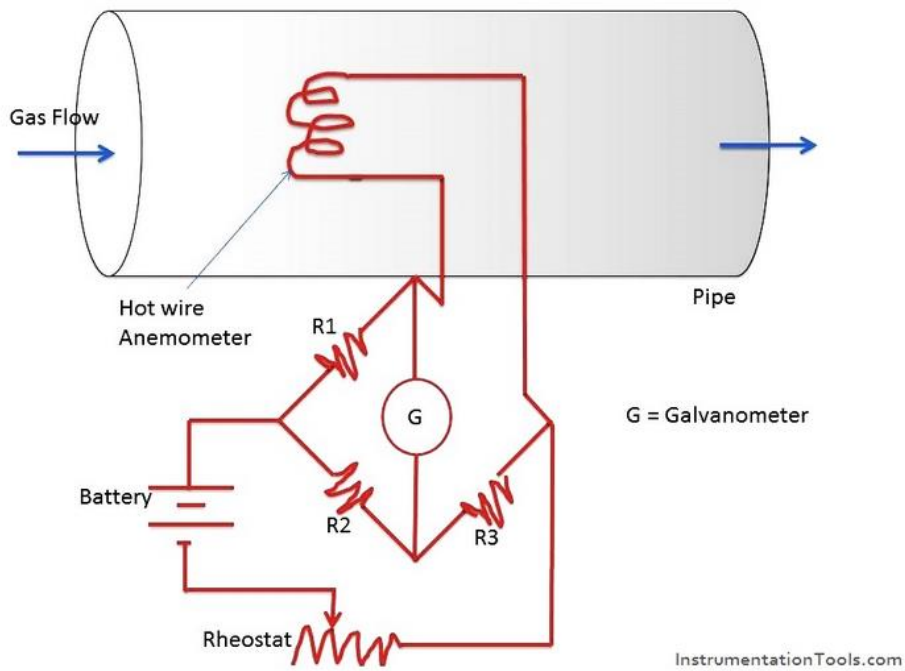
Figure 19: Constant current anemometer

A constant current is passed through the thin wire. Due to the airflow through the sensing wire, heat transfer takes place from the wire to the air, meaning that the temperature of the wire is reduced proportionally to the air velocity. The temperature reduction causes a change in the resistance of the wire and the resistance change becomes a measure of flow rate.
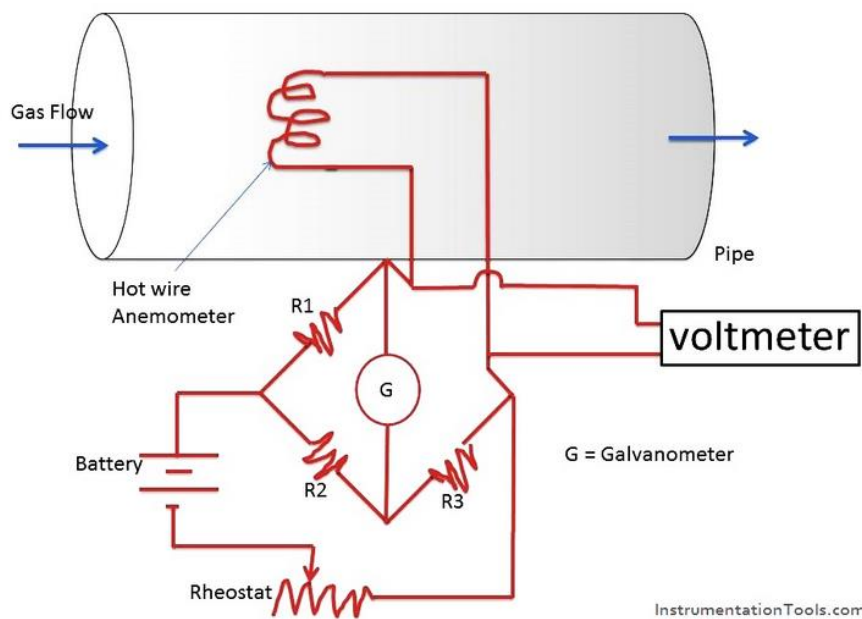
Figure 20: Constant temperature anemometer

The difference in the working principal of the constant temperature is the fact that the electric circuit tries to keep the wire's temperature constant (see Figure 20) while the fluid passes through the sensor and while heat is transferred from the wire to the air. In order the circuit to keep the wire's temperature at its initial value it requires even more current. The total amount of current required to keep the temperature constant is proportional to the flow rate of the air.

Anemometry Governing Equations:

Assuming that the hot wire is placed in the wind tunnel then the wire heated by the current is trying to come into thermal equilibrium with its environment. The thermal equilibrium is the equilibrium between the electrical power supply and the power lost by the convective heat transfer and can be described by the following equation:

$$\blacktriangleright \quad I^2 \cdot R_w = h \cdot A_w \cdot (T_w - T_f)$$

where:

- I, is the current input.
- R_w, is the wire's resistance.
- h, is the convection coefficient.
- A_w, is the projected area of the wire.
- T_w, is the wire's temperature.
- T_f, is the temperature of the fluid.

The resistance of the wire is also a function of temperature:

$$\blacktriangleright \quad R_w = R_{\mathrm{Re}f} \cdot [1 + a \cdot (T_w - T_{\mathrm{Re}f})]$$

where:

- $R_{\mathrm{Re}f}$, the resistance at the reference temperature
- α, is the thermal coefficient of resistance.

According to King's Law the heat transfer coefficient is a function of the fluid's velocity:

$$\blacktriangleright \quad h = a + b \cdot v_f^c$$

where:

- a and b, are variables obtained from the calibration procedure.

- c, is a coefficient that depends on the probe's material and usually equals 0.5.
- v_f, is the fluid's velocity.

Combining all the above equations we can obtain the equation that is giving us the fluid's velocity:

$$v_f = \left\{ \left[\frac{I^2 R_{\mathrm{Re}f}[1+a(\mathrm{T}_w - T_{\mathrm{Re}f})]}{A_w(T_w - T_f)} - a \right] /_b \right\}^{\frac{1}{c}}$$

2. Experimental Study

2.1 Experimental Geometries

The geometries which were chosen to be tested was a remote control formula 1 model, scaled 1:6 and a 3D printed scaled version of the same model. The geometry is not just a scaling of an F1 car size but also has a lot of simplifications in comparison to the complexity of the aerodynamic devices of a real formula 1 car. This geometry could be better compared to Formula 3 or a Formula Student Car. The ideal scenario would be to create two 3D printed (33% and 66% scale) geometries of the 5th race car that our university's Formula Student Team constructed, "Amphion". Due to the fact that constructing two 3D printed geometries would overcome the limit of the budget, it was decided to use the remote control model and by using its respective CAD file a 3D printed 33% of the remote control model would be constructed.

Figure 21: 33% scale of a Formula 3 size model - "Big Model" / R.C. Model

Figure 22: 33% scale of the "Big Model" - "3D Printed Model"

The problem was that there was no CAD file of the remote control model and for this reason the model was scanned using a professional 3D scanner, which was provided by a local 3D

printing company named "3D Hub". The scanned geometry was then used as the base for the design of a representative geometry, using SOLIDWORKS tools. The scanned file lost a lot of accuracy on certain points, due to the complexity of the geometry, as it is demonstrated by the arrows in Figure 23.
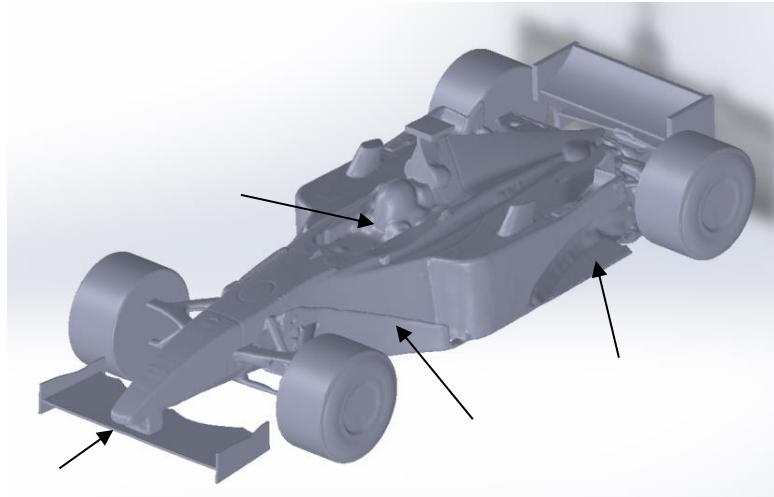
Figure 23: Scanned remote control model

The critical point from our side was to eliminate the geometry errors using the real model, to take accurate dimension and curvature measurements. After completing the design in SOLIDWORKS the geometry was introduced in ANSA where the final geometry cleaning took place, before proceeding with the mesh generation. The final form of the unmeshed geometry is presented in Figure 24.
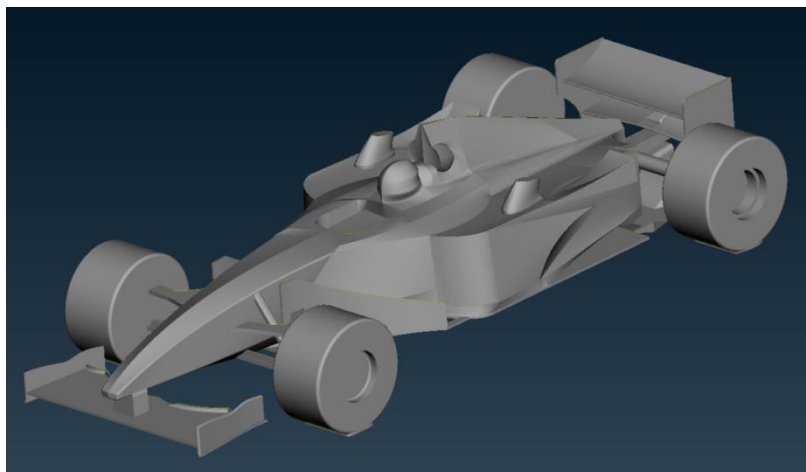
Figure 24: Remote control model geometry in ANSA

The dimensions of the prototype and the models are given in Table 2 and Figure 25:

Table 2: Geometry properties of the wind tunnel test models

Geometry Properties				
Model	**Length (m)**	**Width (m)**	**Height (m)**	**Frontal Area (m^2)**
3D Printed Model	0.25	0.11	0.065	0.0043
Big Model	0.77	0.33	0.195	0.04
F3	2.5	1.128	0.571	0.429

Only the Big and the 3D printed Model were placed in the wind tunnel due to size restrictions.

Below there is a representation of the basic geometrical properties on the CAD file.
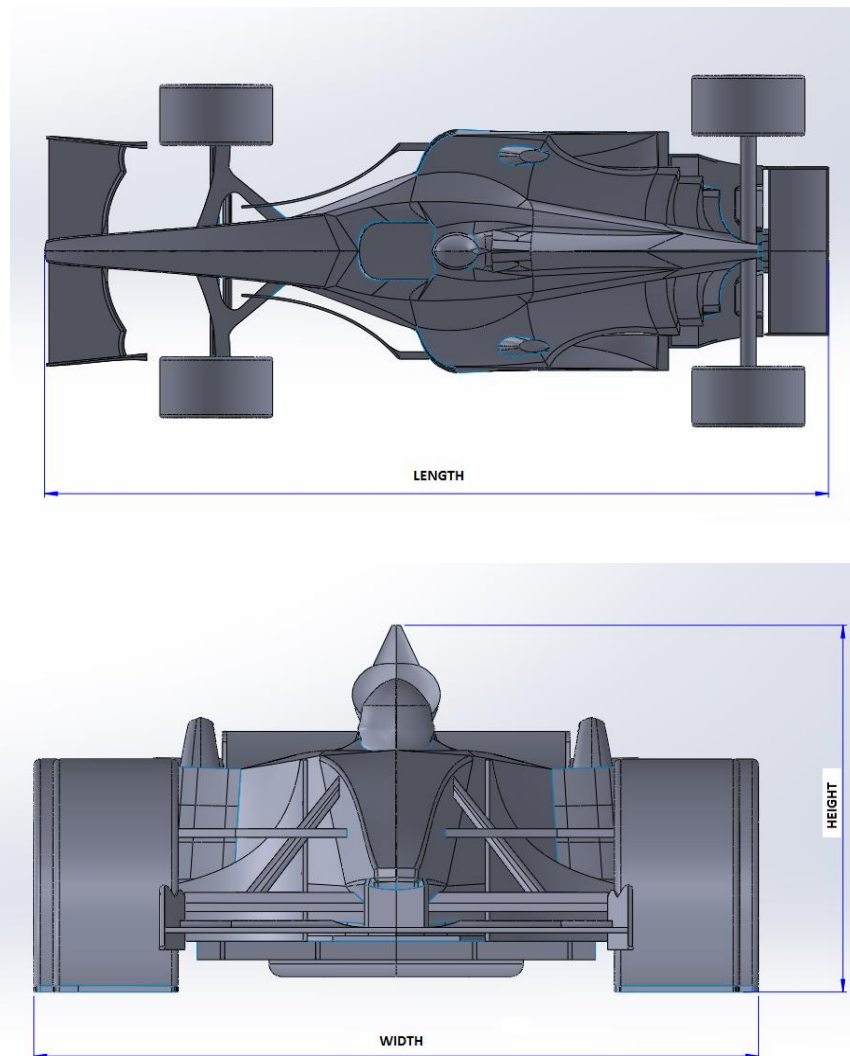
Figure 25: Geometrical Properties of the CAD

2.2 Experimental Equipment

The equipment used consisted of the following items:

1. Subsonic wind tunnel with a 50x70x300cm (W x H x L) working section and speed up to 16 m/s.
2. Remote control model - "Big Model"
3. 3D Printed Model
4. TSI Anemometer
5. 3 axis traverse system

2.3 Experiment Checklist

Experiment outline:

1. Model blockage evaluation.
2. Implementation of the anemometers for the y z planes velocity measurements.
3. Evaluation of the drag produced by the test geometry.
4. Evaluation of the turbulence produced by the test geometry.
5. Flow visualization and turbulence examination.

2.4 Blockage Calculations

As far as the wind tunnel experiments are concerned there is a vital parameter that can play an important role in the results of our experiments which is the test section's blockage ratio, which calculated by the following equation:

$$\text{Blockage} = \frac{\text{Model Frontal Area}}{\text{Wind Tunnel Cross Sectianal Area}} \cdot 100 = \%$$

After conducting these simple calculations for each one of the models, the following results were obtained:

Table 3: Test Model Blockages

Geometry Model	Blockage %
3D Printed Model	1.225
Big Model	11.25

The 3D printed model's blockage is very small comparing it to the theoretical limit which is 5%, so no blockage related problems were expected. For the big model the blockage was

11.25% but considering that blockages up to 20% are studied in automotive industry, we had to investigate whether we had significant error in the free stream speed or not and if that error was acceptable for the rest of the study. At first the free stream's velocity was measured, without installing the model. The experiment was repeated for 5 wind tunnel speeds. Afterwards each of the two models was placed separately, and the following results were obtained:

Table 4: Blockage Effect on Free Stream Velocity

WT Speed (Hz)	No Model Free Stream Velocity (m/s)	Big Model Free Stream Velocity (m/s)	3D Printed Model Free Stream Velocity (m/s)	DU (%)
32	8.9	8.7	8.9	2.2
38.4	10.5	10.2	10.5	2.9
44.4	12.0	11.7	12.0	2.5
51.5	14.5	13.8	14.5	4.8
57.1	15.7	15.2	15.7	3.2

The conclusion was that there was no blockage effect in the case of 3D printed model but there was 3% error in the free stream air when we tested the "Big Model". This error was accepted so we moved on with velocity measurements.

2.5 Description of Experimental Arrangement

The models were placed in the test section, keeping a reasonable distance from the inlet and the outlet of the test section. They were also fixed on the tunnel's floor in order to prevent them from being taken away from the airflow. The experimental concept was to take velocity measurements in front and behind the two models. The distances at which the measurements were taken were 11cm and 5cm for the big and the 3D printed model, respectively. For this reason, the anemometer was placed on the 3-axis transverse system at the top of the tunnel.

Five experiments were conducted for the previously mentioned wind tunnel speeds which resulted in the calculation of 10 velocity planes for each one of the geometries, 5 in front of the car and 5 behind. These measurements were used for the calculation of drag for the respective free stream speed.

2.6 Anemometer Calibration

In order to calculate the velocity profiles in front and behind the car, the TSI anemometer was utilized, since it gives the air velocity value at a specific point, straightforwardly, by contrast to the pitot tube which gives the dynamic pressure which needs to be transformed by the following equation: $P_{dyn} = \frac{1}{2} \cdot \rho \cdot U^2$, in order to obtain the velocity value. That means that using the anemometer we were not going to lose time doing the transformations for all the different points.

Before proceeding with the measurements, we had to validate the anemometer accuracy and check its divergence from the pitot tube which is supposed to give very accurate measurements. For this reason, the air's free stream velocity was measured at a specific point inside the wind tunnel, for 5 wind tunnel speeds and then plotted the respective results. The experimental data and plot can be seen in the following tables and figure:

Table 5: TSI anemometer calibration conditions

Experiment Conditions	
Air Pressure (Pa)	101325
Air Temperature (°C)	30
Air Temperature (K)	303
Air Density (kg/m^3)	1.182

Table 6: TSI Anemometer vs Pitot Tube Experimental Data

Anemometer Calibration Data					
Wind Tunnel Speed (Hz)	Dynamic Pressure (Pa)	U pitot (m/s)	U tsi (m/s)	DU (m/s)	Divergence%
10	4	2.6	2.9	-0.3	0.11
20	19	5.7	5.8	-0.1	0.02
30	43	8.5	8.6	-0.1	0.01
40	77	11.4	11.7	-0.3	0.02
50	119	14.2	14.2	0.0	0.00
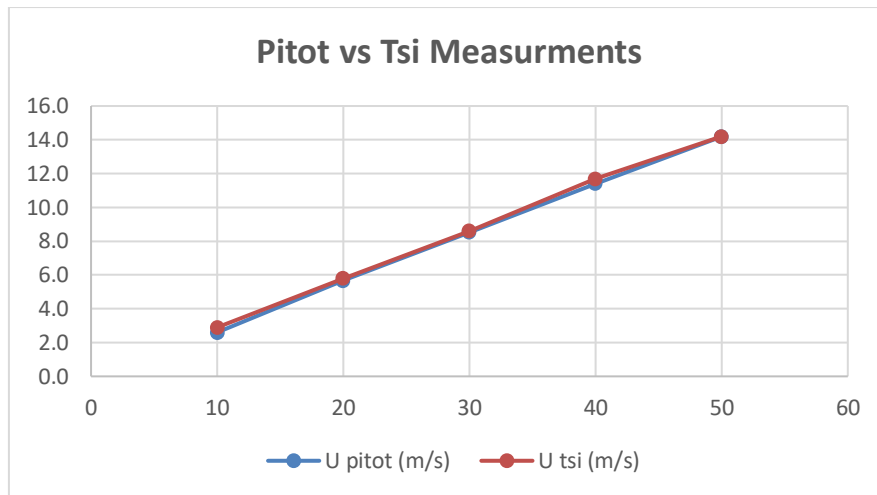
Figure 26: TSI Anemometer Calibration plot

The conclusion from the above Figure 26 is that the difference between the 2 tools is negligible and that the anemometer can be trusted for calculating the velocity profiles.

2.7 Velocity Profiles Development

The planes at which the measurements were taken at the distance of 11cm in front and 11 cm behind the "Big Model" and 5cm respectively for the 3D printed model. The area of each plane was 35cm X 22cm (Width X Height) for the Big model and 15cm X 6cm for the 3D printed model. The measurement step for the "Big Model" was 2.5cm and for the "3d Printed Model" 1cm. The area was chosen using as criterion the frontal area of the models and the fact that we should reach the free stream when measuring either above or on the left and right side of the model. After gathering all the data, before moving to the calculation of the drag, 3D Maps and contour plots were created in order to check their validity. The 3D Maps were created using the splines method. In the following section 8 3D maps and 8 contour plots are presented for each model for the following wind tunnel speeds: 33(Hz) and 57 (Hz). The difference in the free stream velocity during the experiment of the "Big Model" is a result of the blockage effect. In the following pages 3D maps and contour plots for different free stream velocities are presented. In Figure 27 and Figure 31 the 3D velocity maps for the inlet and the outlet of the Big Model respectively, at 8.7 (m/s), are presented. In Figure 28 and Figure 32 the 3D velocity maps for the inlet and the outlet of the 3D Printed Model respectively, at 8.9 (m/s), are presented. In Figure 35 and Figure 39 the 3D velocity maps for the inlet and the outlet of the Big Model respectively, at 15.2 (m/s), are presented. Figure 36 and Figure 40 the 3D velocity maps for the inlet and the outlet of the 3D Printed Model respectively, at 15.7 (m/s), are presented. In Figure 29 and Figure 33 the velocity contour plots for the inlet and the outlet of the Big Model

respectively, at 8.7 (m/s), are presented. In Figure 30 and Figure 34 the velocity contour plots for the inlet and the outlet of the 3D Printed Model respectively, at 8.9 (m/s), are presented. In Figure 37 and Figure 41 the velocity contour plots for the inlet and the outlet of the Big Model respectively, at 15.2 (m/s), are presented. Finally, in Figure 38 and Figure 42 the velocity contour plots for the inlet and the outlet of the 3D Printed Model respectively, at 15.7 (m/s), are presented.
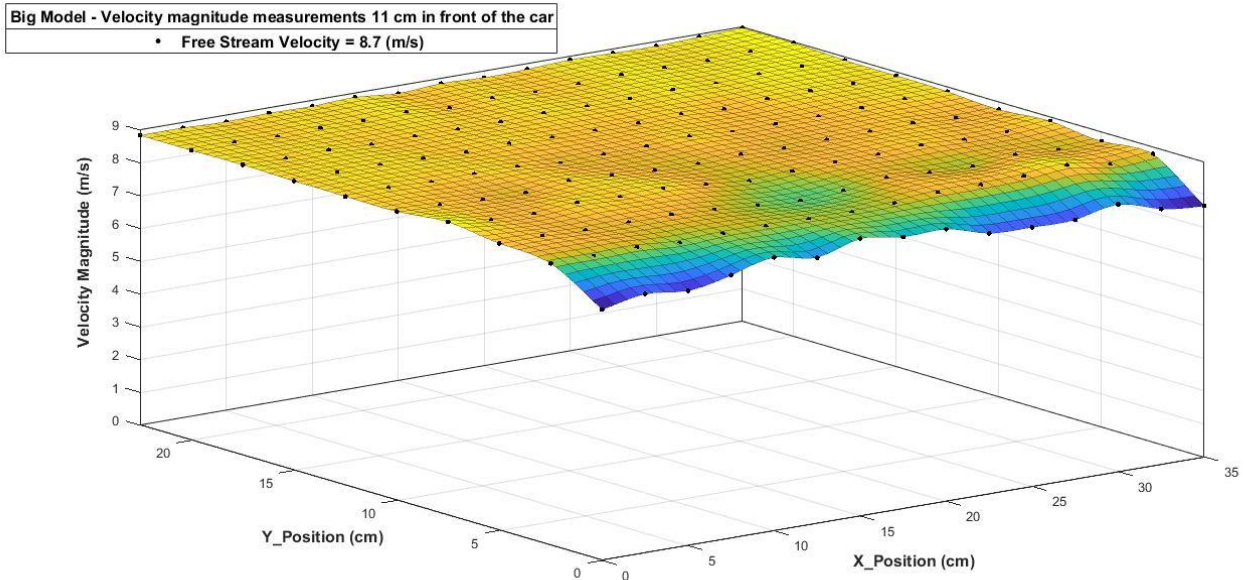
Figure 27: "Big Model", front plane velocity magnitude at 8.7 (m/s)
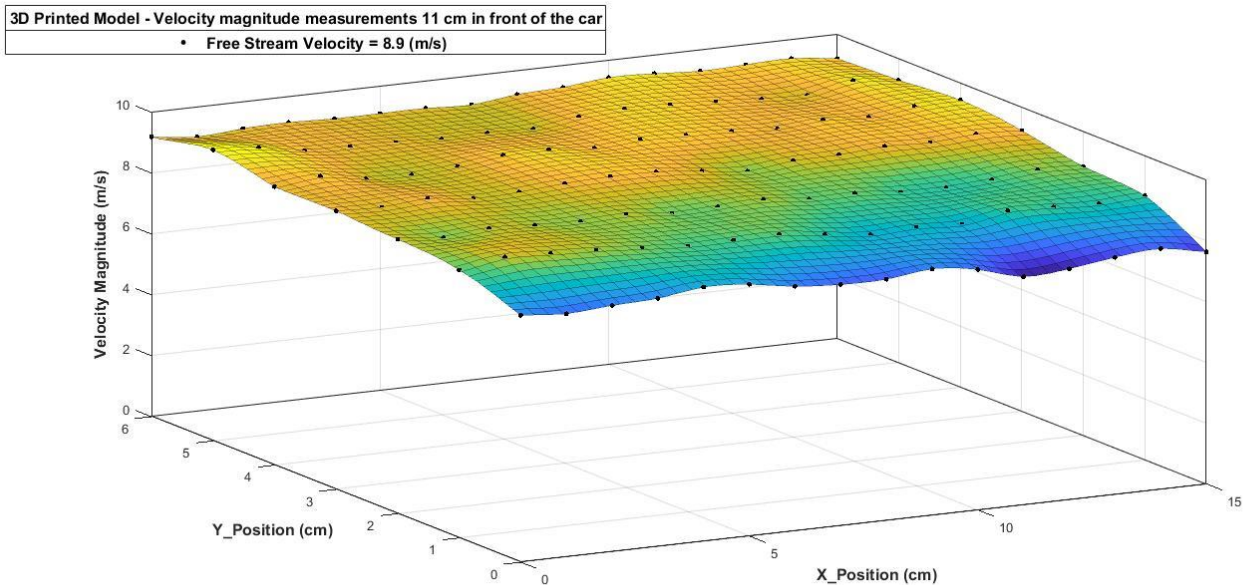
Figure 28: "3D Printed Model", front plane velocity magnitude, at 8.9 (m/s)
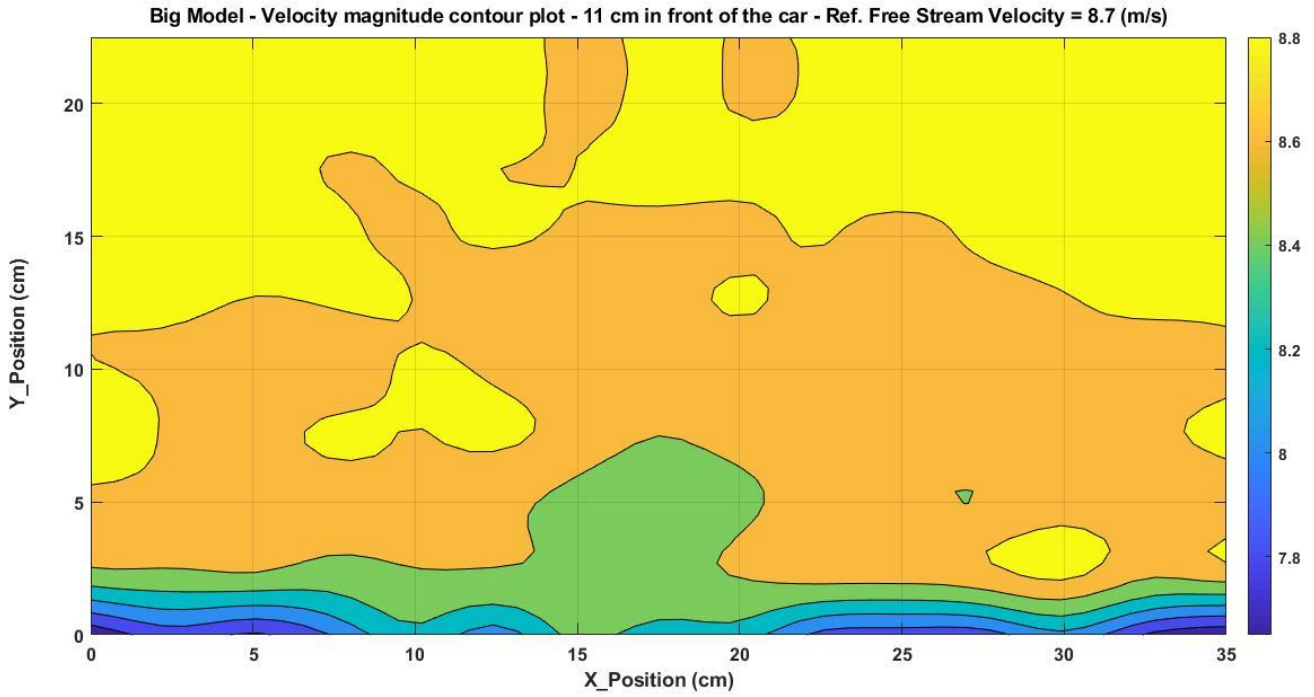
Figure 29: "Big Model", front plane contour plot, at 8.7 (m/s)
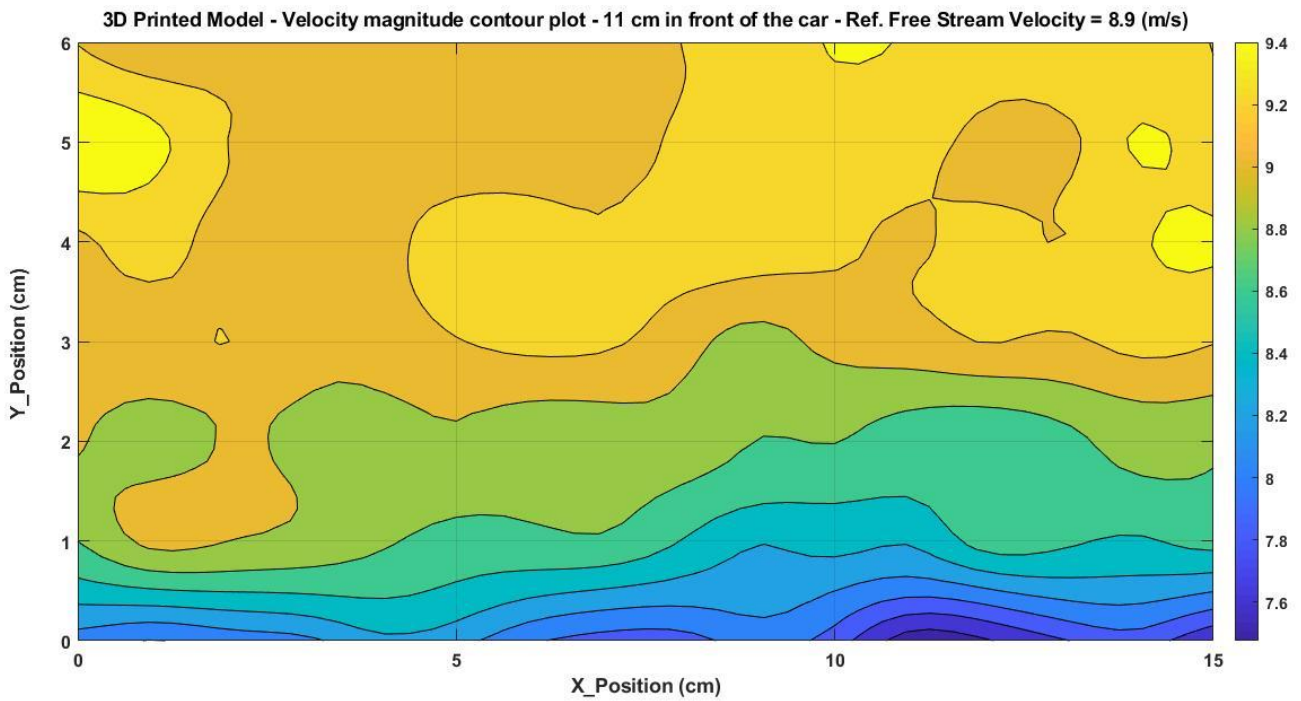
Figure 30: "3D Printed Model", front plane contour plot, at 8.9 (m/s)
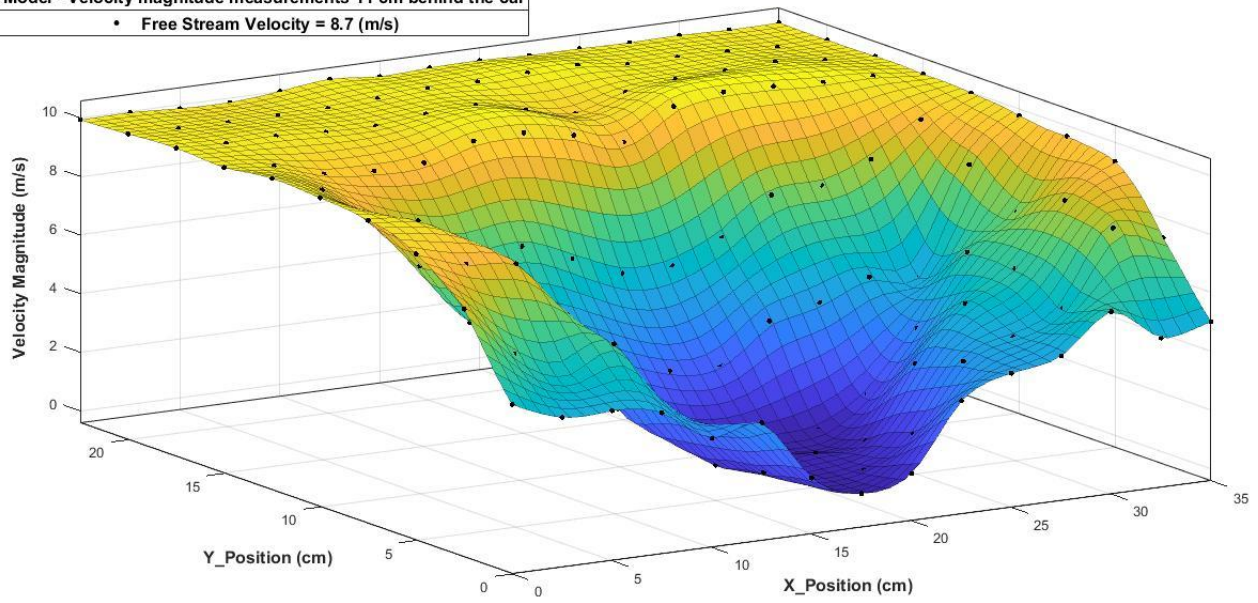
Figure 31: "Big Model", rear plane velocity magnitude, at 8.7 (m/s)
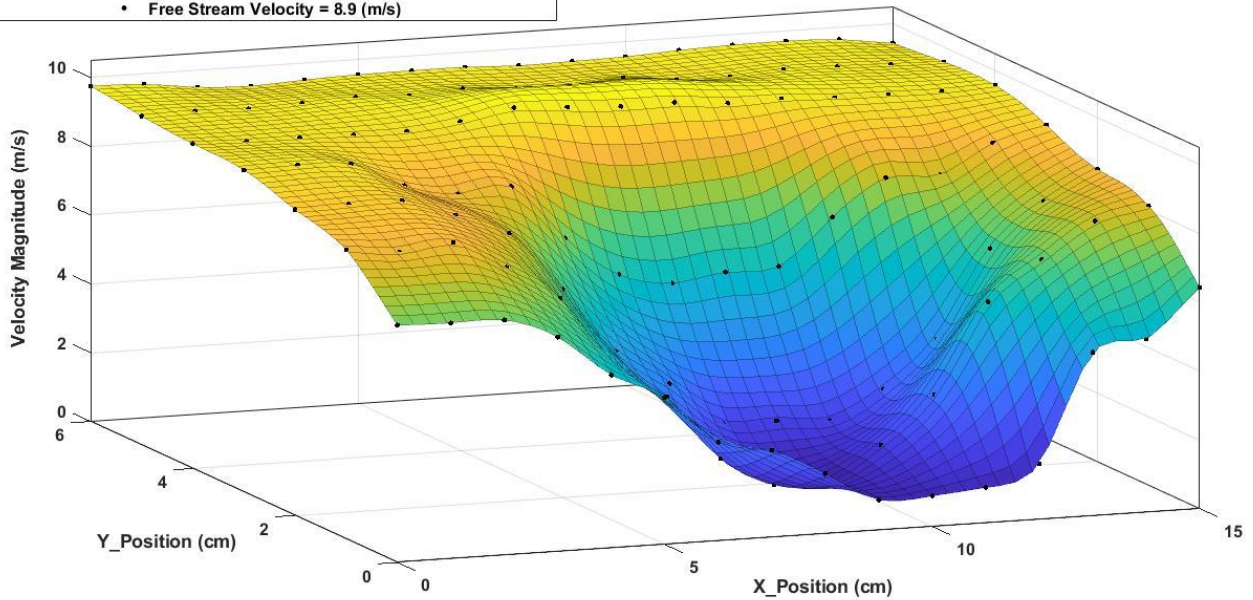
Figure 32: "3D Printed Model", rear plane velocity magnitude, at 8.9 (m/s)
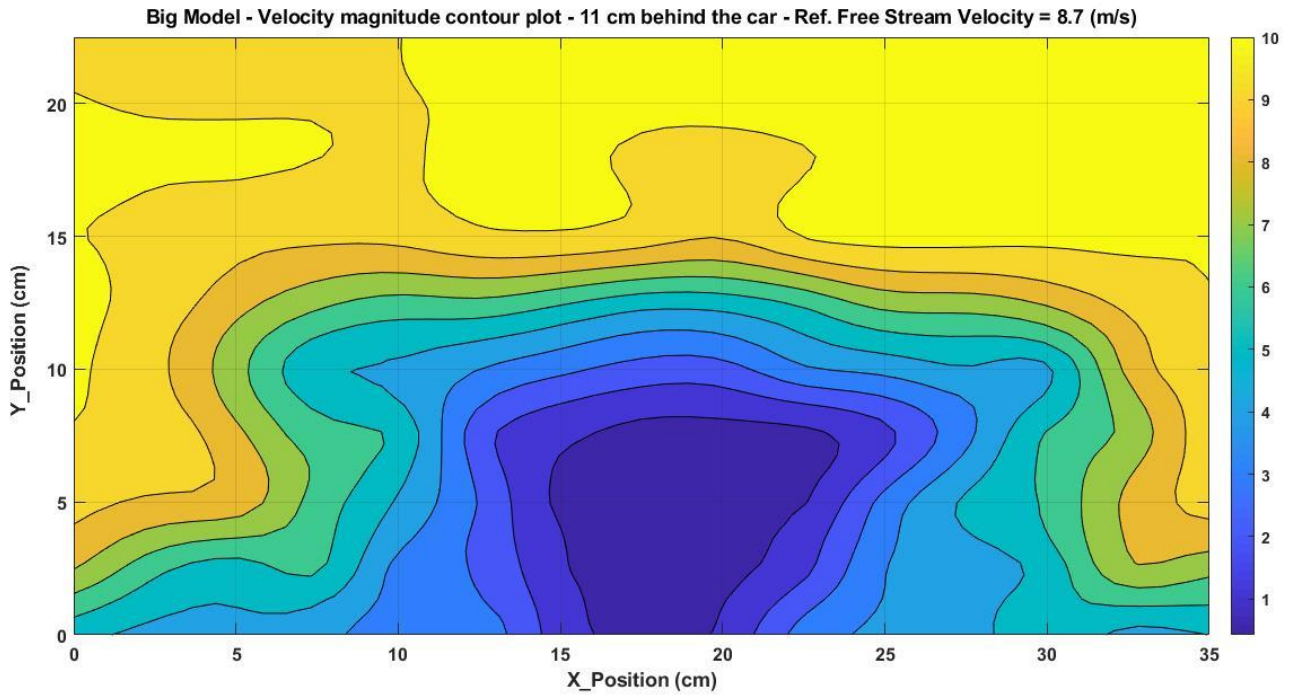
Figure 33: "Big Model", rear plane contour plot, at 8.7 (m/s)
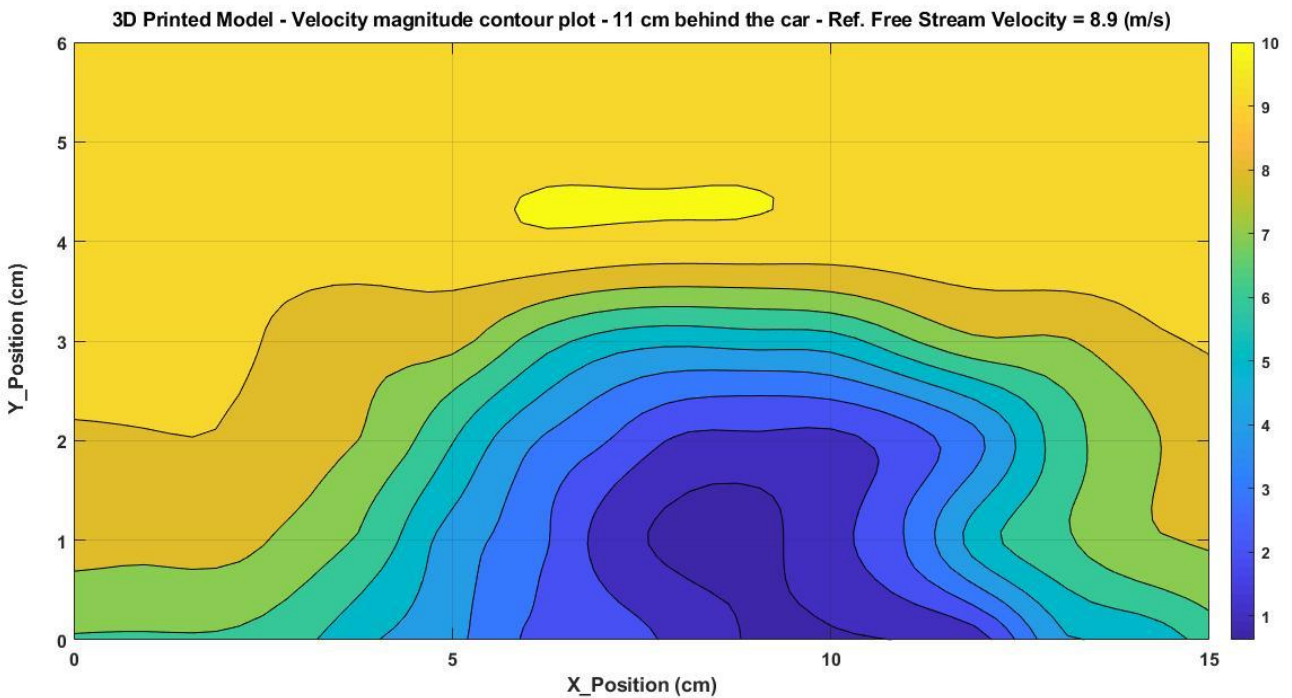
Figure 34: "3D Printed Model", rear plane contour plot, at 8.9 (m/s)
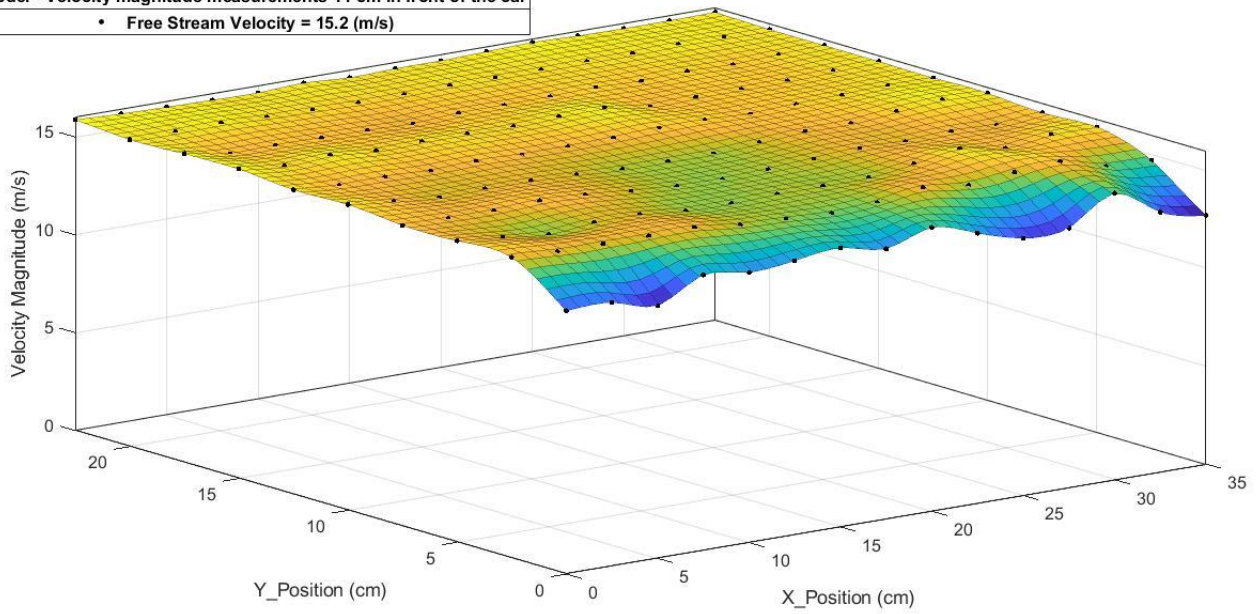
Figure 35: "Big Model", front plane velocity magnitude at 15.2 (m/s)
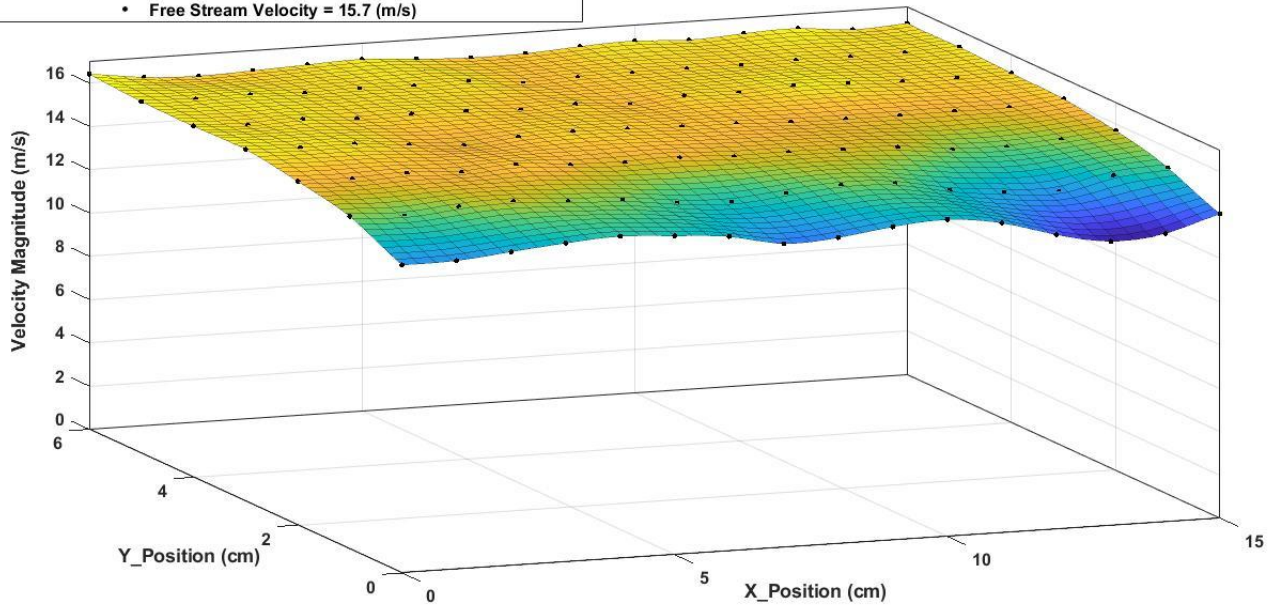
Figure 36: "3D Printed Model", front plane velocity magnitude at 15.7 (m/s)
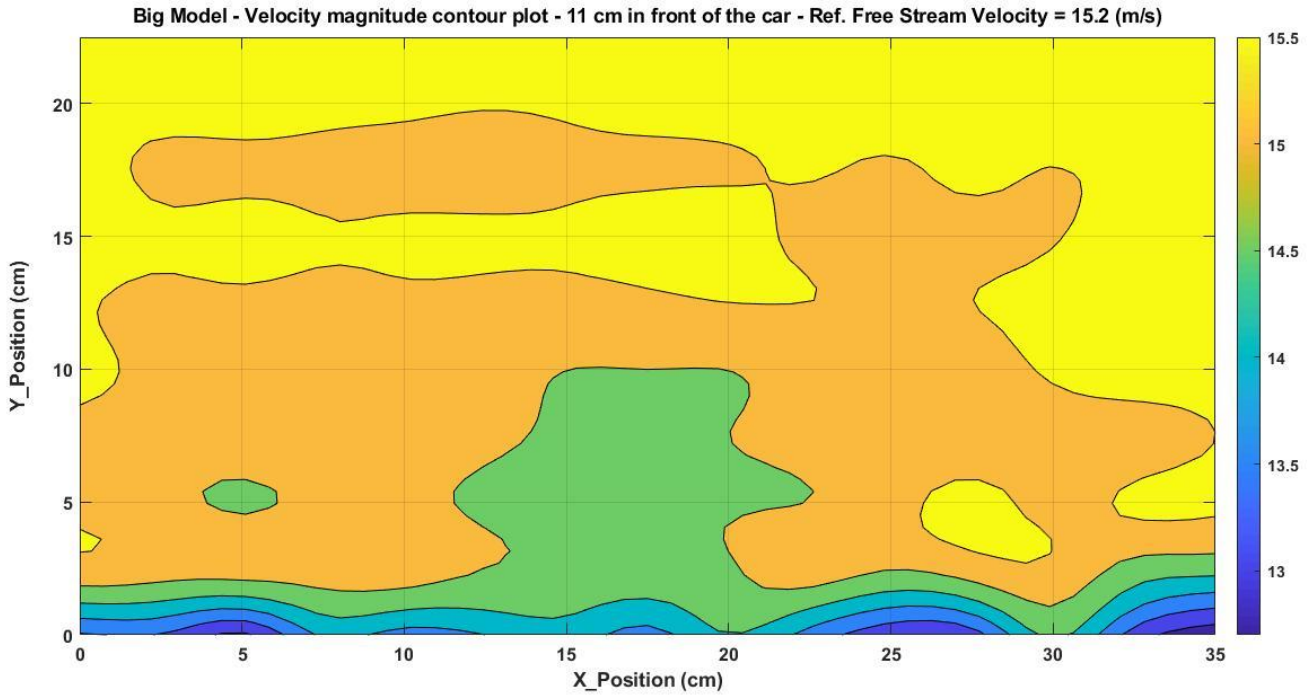
Figure 37: "Big Model", rear plane contour plot, at 15.2 (m/s)
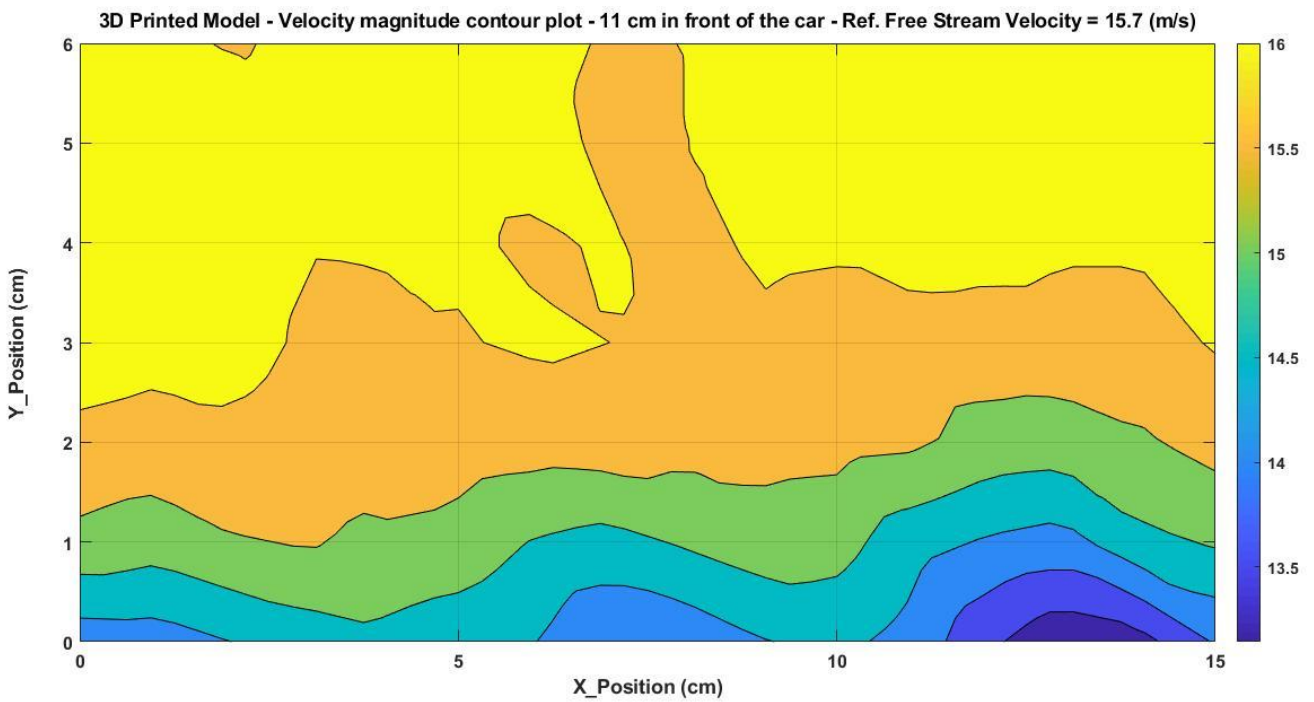
Figure 38: "3D Printed Model", front plane contour plot, at 15.7 (m/s)
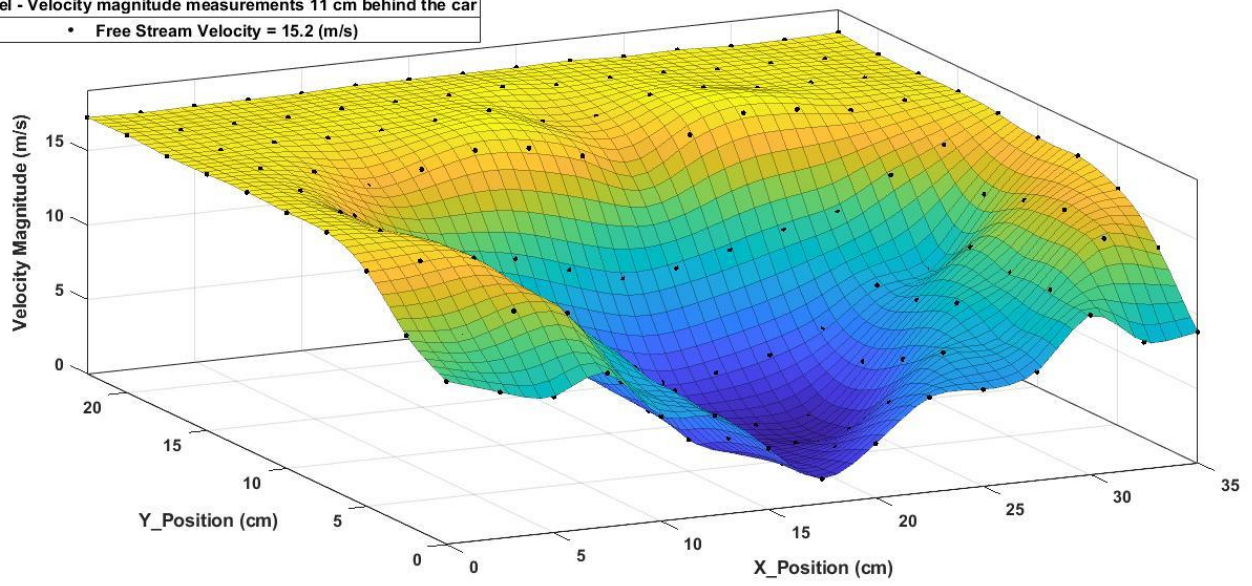
Figure 39: "Big Model", rear plane velocity magnitude at 15.2 (m/s)
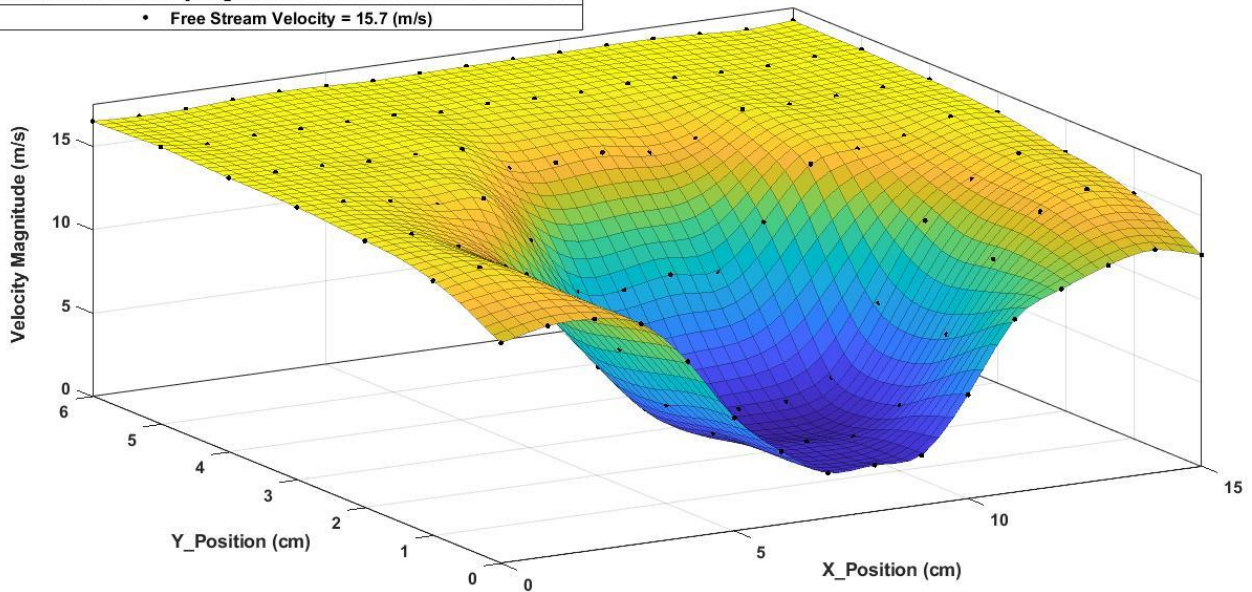
Figure 40: "3D Printed Model", rear plane velocity magnitude at 15.7 (m/s)
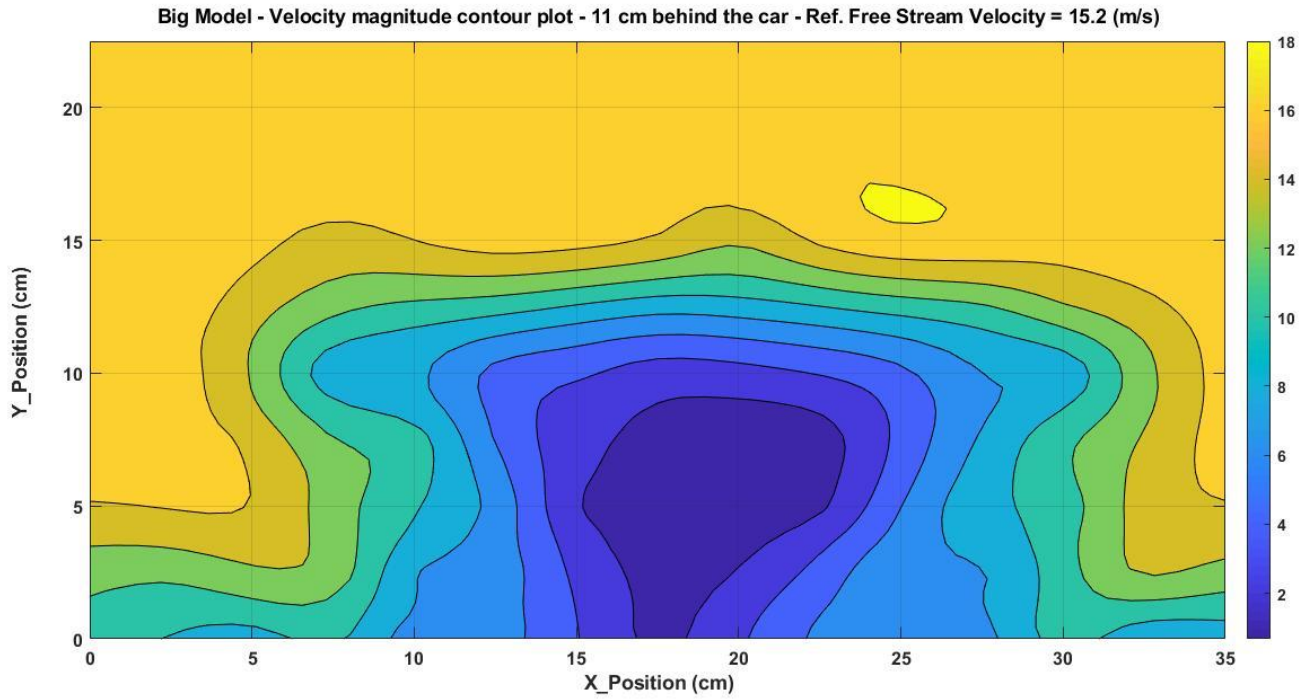
Figure 41: "Big Model", rear plane contour plot, at 15.2 (m/s)
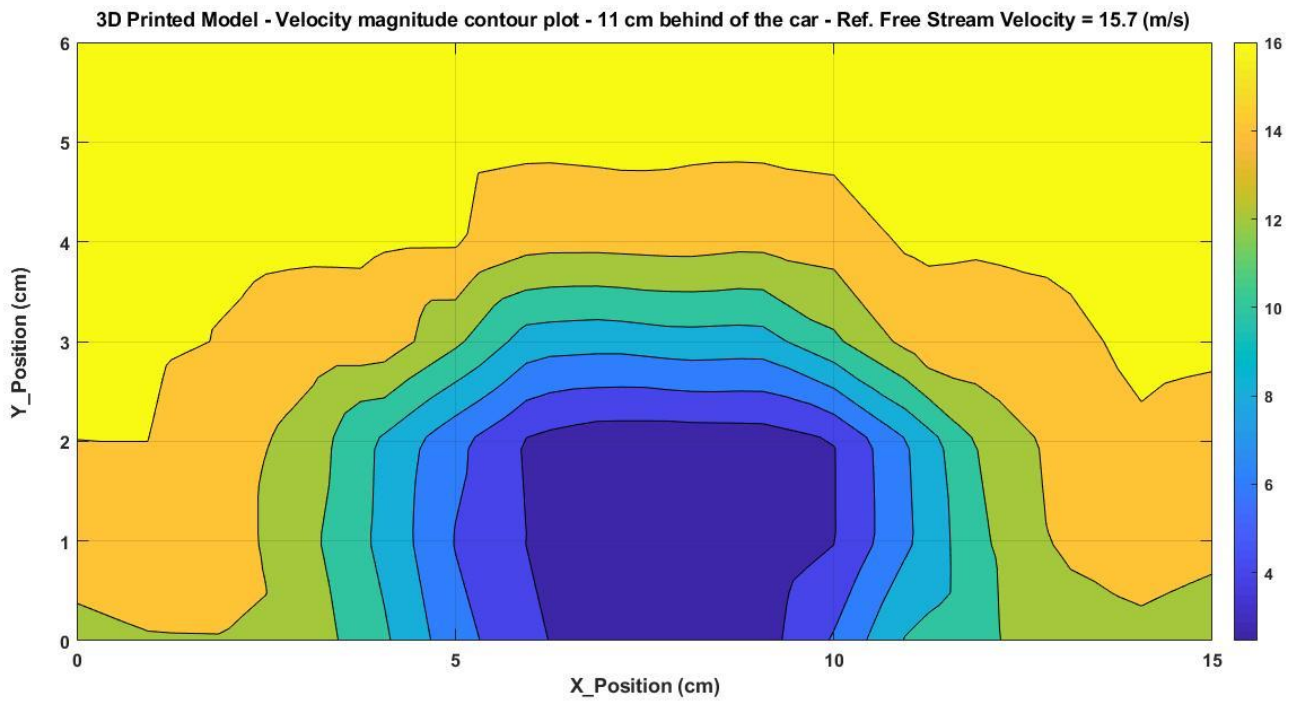
Figure 42: "3D Printed Model", rear plane contour plot, at 15.7 (m/s)

As far as the front planes are concerned the velocity magnitude is almost flat. However, there is disturbance, for the first 2 cm above the "road", because of the boundary layer of the wind tunnel surface.

Concerning the rear planes, the velocity magnitude was as expected, for each one of the experiments and what is seen, is that there is a low velocity region behind the car, which becomes more profound as the free stream speed increases.

2.8 Drag Calculation Method

Since there was no wind tunnel balance in the laboratory drag could not be measured directly. A wind tunnel balance is a device that measures the aerodynamic loads a model experience during a wind tunnel test. A balance is just a multiple axis force transducer. Balances are designed to measure some or all the three forces and three moments a model experience. In aerodynamics terms, these forces and moments are called: Normal, Side, and Axial Force and Pitch, Yaw, and Rolling moment. Balances come in many different designs and configurations. The most common configuration is the external strain gauged balance, which is placed outside the model, inside or outside the wind tunnel chamber test section, but they always introduce some interference in the wind flow. However, the possibility to change test models with almost no effort provides a high flexibility to the wind tunnel facility.

Balances are made of flexures that deflect with load is applied. These flexures are designed to respond to load in a particular axis. Balance that can measure multiple loads and moments have individual flexures that each measure load in one axis. Strain gauges are bonded to these flexures to measure the deflections. Applied loads cause the bonded strain gauges to stretch. When a strain gauge changes length its electrical resistance changes. Individual strain gauges are wired in a whetstone bridge so that these small resistance changes can be measured as voltage signals. As [González, Ezquerro, Lapuerta, Laverón, and Rodríguez, 2011] and his co-authors state the first step before taking valid measurements, is to perform a static calibration and after that it is desirable to perform a dynamic calibration with the help of the already existent typical test models results.

As someone can understand the construction of such an arrangement was not able to happen during the dissertation of this thesis not only because of the complexity but also because of budget limitations.

For this reason, in each one of the experiments, drag was calculated from the momentum equation. The equation states that the sum of forces acting on the air is equal to the change in the momentum of the air, in front and behind the car.

$$\text{Drag} = \dot{m}(U_1 - U_2)$$

In our case, we did not have a single velocity in front and behind the car, we had to transform it an integral form:

$$Drag = \int_A (m \cdot U_{front}) dA - \int_A (m \cdot U_{rear}) dA = \int_A (\rho \cdot V \cdot U_{front}) dA - \int_A (\rho \cdot V \cdot U_{rear}) dA \Rightarrow$$

$$\Rightarrow Drag = \rho \cdot A_i \cdot \left(\sum_{i=1}^{n} (U_{front,i})^2 - \sum_{i=1}^{n} (U_{rear,i})^2 \right)$$

The results of the drag calculations are presented and discussed in the respective section of the thesis.

3. Numerical Study

All the CFD were performed using a computer with an i5-4690k central processing unit with 4 cores, 4 threads and 32GB RAM.

3.1 Mesh Properties

All the meshes where constructed using the ANSA program. In both cases the control volume had the same size as the wind tunnel's test section. For the purpose of this study 6 different meshes were developed in order to conduct the element type, the mesh independence and the boundary layer modeling study which would lead to the final mesh size and element type before proceeding with the simulations of the models vs different free stream velocities.

The two models and the control volumes surrounding them, are presented Figure 43 and Figure 44. The control volume has the same size of the wind tunnel's test section. The blue box, called "size box", around the geometry of the "Big Model" is a setting given by the ANSA program which help the user control the maximum tetra or hexa size at certain locations of the model. The size boxes are placed around the car because this is the area of interest and that is why the user wants to refine the mesh around that region, by setting a low upper limit of cell size. The functionality of the size boxes is better understood following figures where cut sections of the volume mesh are presented.
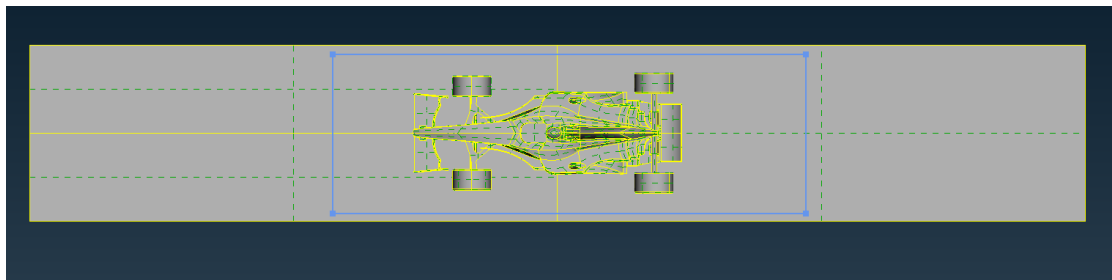
Figure 43: "Big Model" geometry and control volume - Top View
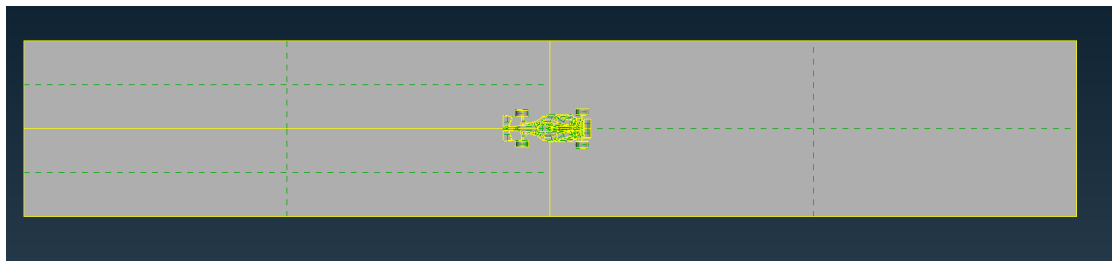
Figure 44: "3D printed model" geometry and control volume - Top View

In the next figure the control volume's surface mesh is presented and it is relatively coarse both in the "Big Model" and the "3D Printed Model". This is done because the geometry is much simpler than the car's geometry.
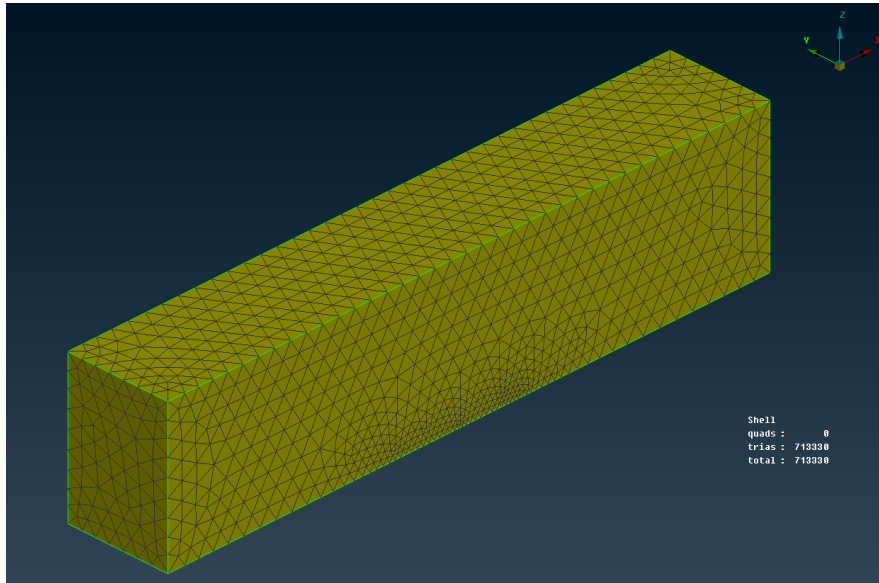
Figure 45: "Big Model" control volume surface mesh

In Figure 46, Figure 47 and Figure 48 different types and sizes of mesh are presented, for the "Big Model". In <u>Figure 46</u> and <u>Figure 47</u> we see the fine and the coarse tetrahedral dominated meshes. Both can be considered as hybrid meshes since both tetras and pentas appear to be part of the volume mesh, but their total number is relatively small to the total tetras. Finally, in <u>Figure 48</u> a middle section of the hexahedral mesh is presented. The term coarse in this figure refers to the fact that the hexahedral mesh performance was compared to the tetrahedral coarse mesh performance since the mesh independence study proved that the coarse mesh of 8 million cells doesn't have big divergence from the fine mesh of 11 million cells, but that will be analyzed afterwards.
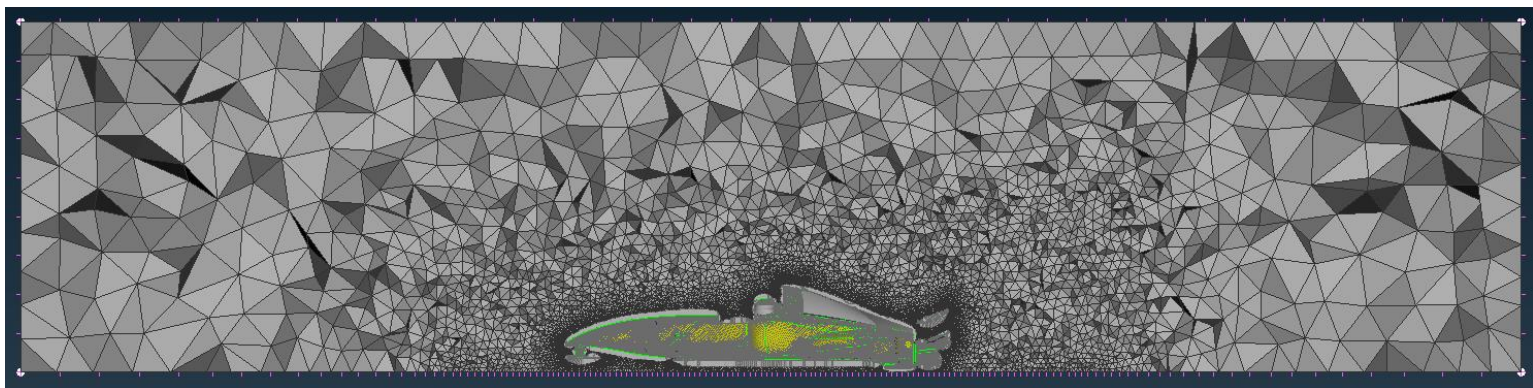
Figure 46: "Big Model" fine tetra volume mesh - 11 million cells - Middle Section
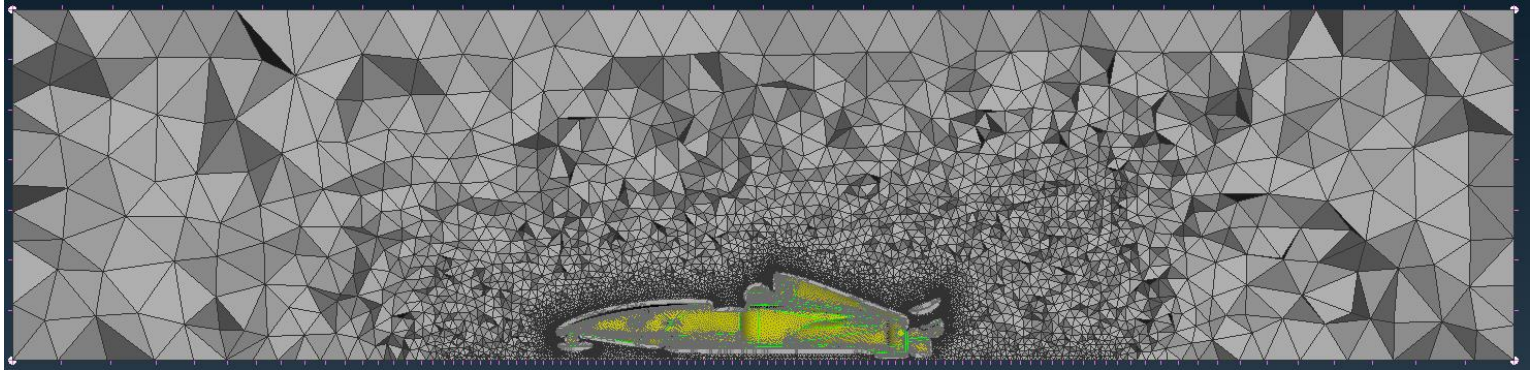
Figure 47: "Big Model" coarse tetra volume mesh - 8 million cells - Middle Section
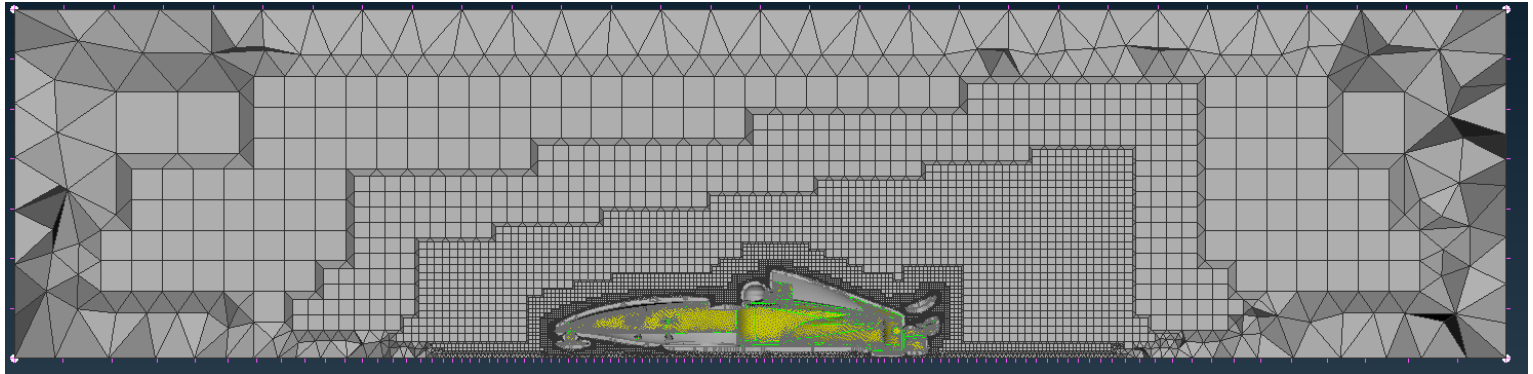
Figure 48: "Big Model" coarse hexahedral volume mesh - 8 million cells - Middle Section

Figure 50 and Figure 51, the fine tetrahedral, coarse tetrahedral and coarse hexahedral meshes of the "3D Printed model", are shown respectively.
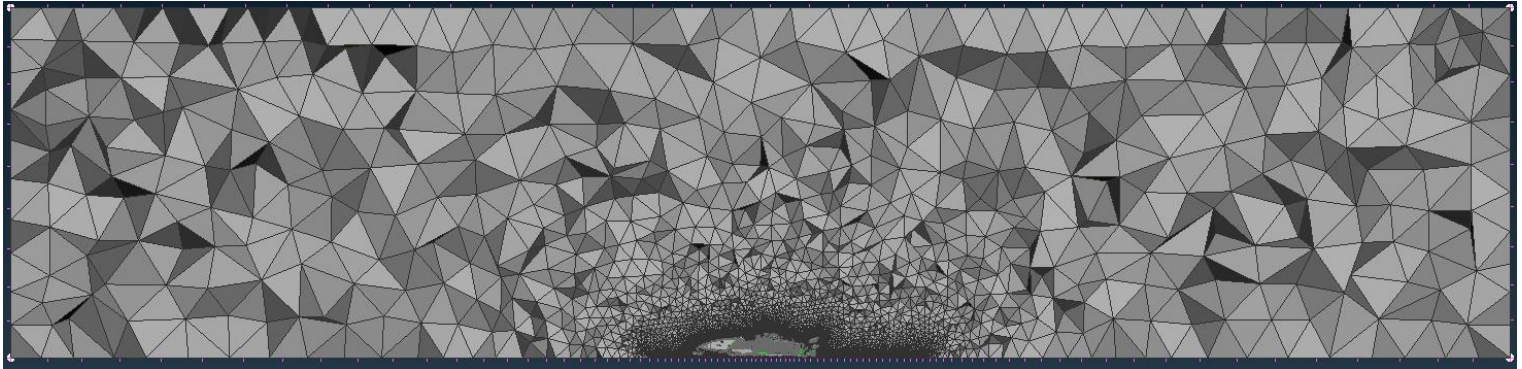
Figure 49: "3D Printed Model" fine tetra volume mesh - 8 million cells - Middle Section
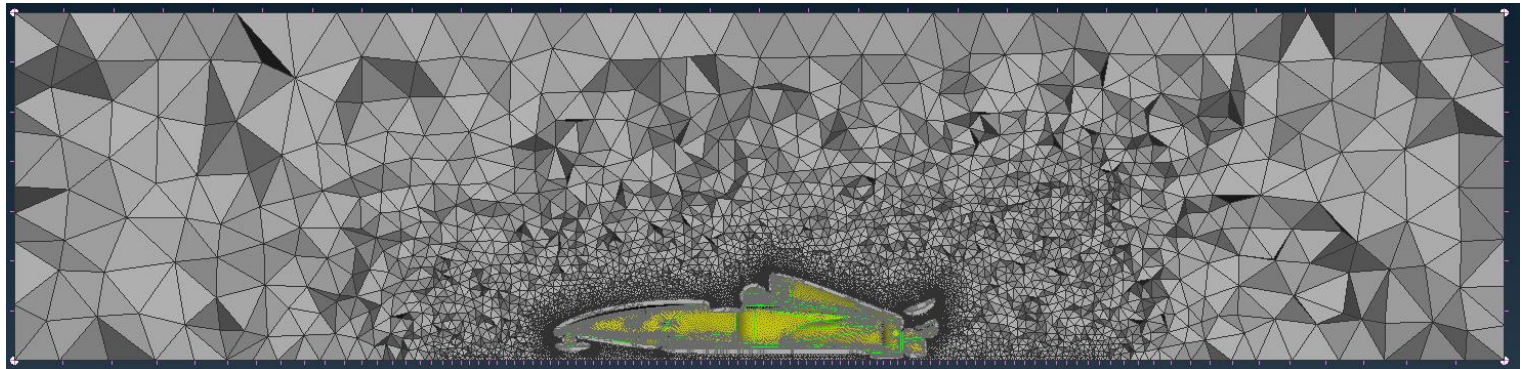
Figure 50: "3D Printed Model" coarse tetra volume mesh - 5 million cells - Middle Section
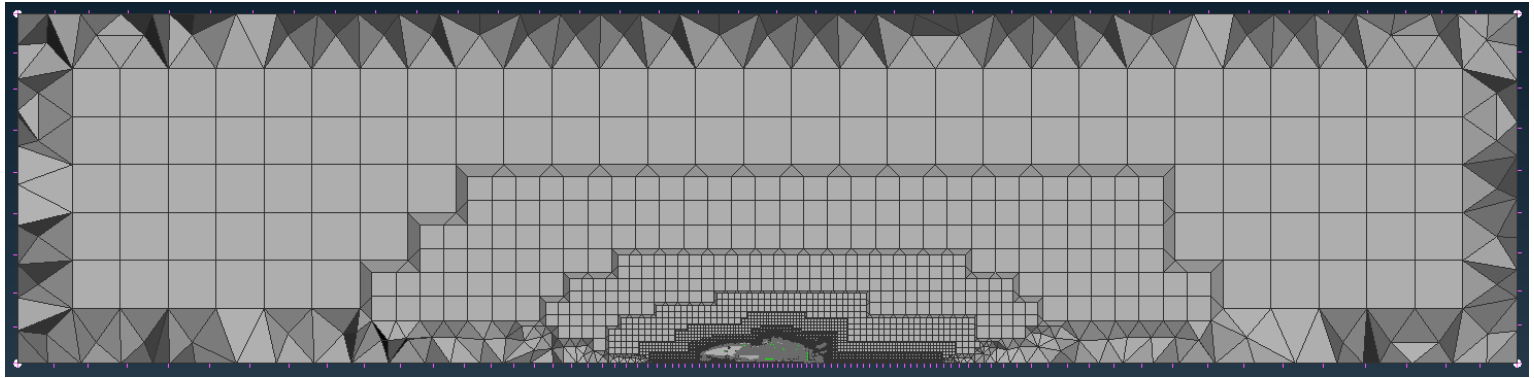
Figure 51: "3D Printed Model" fine hexahedral volume mesh- 5 million cells - Middle Section

In Figure 52, a closer look at the car's mesh is taken.
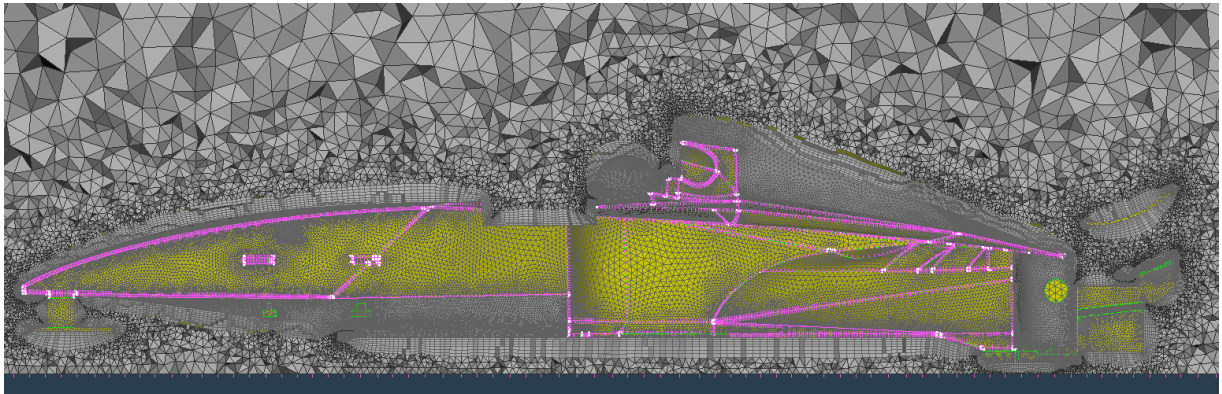
Figure 52: "Big Model" fine tetra volume mesh - Middle Section Zoom

In Figure 53 a check of the first layer height is performed. The actual value that was applied in this case was 0.58 (mm) and by measuring the first layer's height after the layer mesh was performed it is confirmed that the right value was applied.
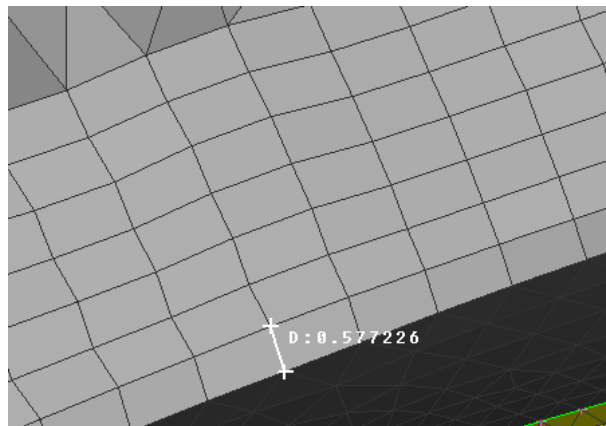
Figure 53: "Big Model" first layer height target check
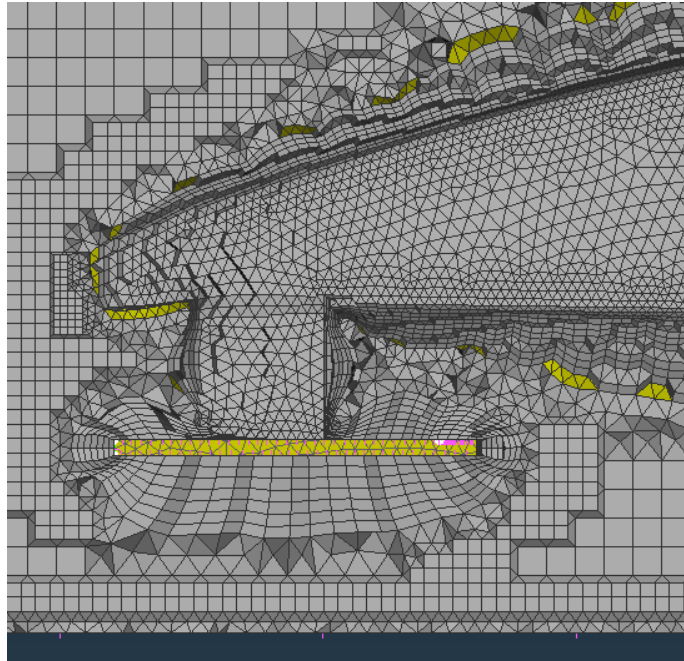
Figure 54: "Big Model" Hybrid Mesh - Transition region between the boundary layer and the hexa dominated control volume through tetras and pyramids

3.2 Mesh Quality Checks

First, a representation of the volume and the layers mesh quality is done. It is reminded that the mesh qualities shown refer to the coarse meshes of the "Big Model" and the "3D Printed Model" and to the fine mesh of the F3 Model. In these meshes a target y+=30 was used for the layers modeling, as the k-ε model was applied and the first layer height was computed by applying a free stream velocity equal to 15.2 (m/s) to the Big and the F3 model and 15.6 (m/s) to the 3D Printed Model. A very fine mesh was used for the F3 model to avoid solution accuracy problems, since no mesh independency study was done as there were no experimental data to compare. More information about the mesh generation is provided in 3.3.

With respect to the skewness criterion regions that were presented inTable 1, the skewness criterion is satisfied for all the cases. Specifically, after observing Figure 55, Figure 57 and Figure 59 it is confirmed that zero elements belong to the bad quality regions between 0.92 and 0.99, while the biggest percent of the elements belongs to ranges below 0.5which are characterized as good quality regions. Finally from Figure 56, Figure 58 and Figure 60 despite the fact that some elements belong to the bad quality class 6, the layers quality is also satisfying the skewness criterion, because the percent of these elements with respect to the total number of the layers elements is below 0.002%.

Solid Skewness (Tetras only) Graph

Classes	Ranges		Elements
Class 1:	< 0.00	0.00%	0
Class 2:	0.00 - 0.10	12.82%	645344
Class 3:	0.10 - 0.20	22.30%	1122708
Class 4:	0.20 - 0.30	25.03%	1259976
Class 5:	0.30 - 0.40	20.49%	1031348
Class 6:	0.40 - 0.50	12.66%	637054
Class 7:	0.50 - 0.60	5.09%	256331
Class 8:	0.60 - 0.70	1.19%	59710
Class 9:	0.70 - 0.80	0.28%	14153
Class 10:	0.80 - 0.90	0.14%	7051
Class 11:	0.90 - 0.92	0.00%	63
Class 12:	0.92 - 0.95	0.00%	0
Class 13:	0.95 - 0.98	0.00%	0
Class 14:	0.98 - 0.99	0.00%	0
Class 15:	0.99 - 1.00	0.00%	0
Class 16:	1.00 - 1.00	0.00%	0
Class 17:	> 1.00	0.00%	0
			Total: 5033738

Figure 55: Big Model - Volume Mesh - Skewness Check

Solid Layers Quality Graph

Classes	Ranges		Elements
Class 1:	< 0.00	0.00%	0
Class 2:	0.00 - 0.25	47.93%	1527432
Class 3:	0.25 - 0.50	30.95%	986378
Class 4:	0.50 - 0.75	15.99%	509461
Class 5:	0.75 - 1.00	5.12%	163235
Class 6:	1.00 - 2.00	0.00%	135
Class 7:	> 2.00	0.00%	0
			Total: 3186641
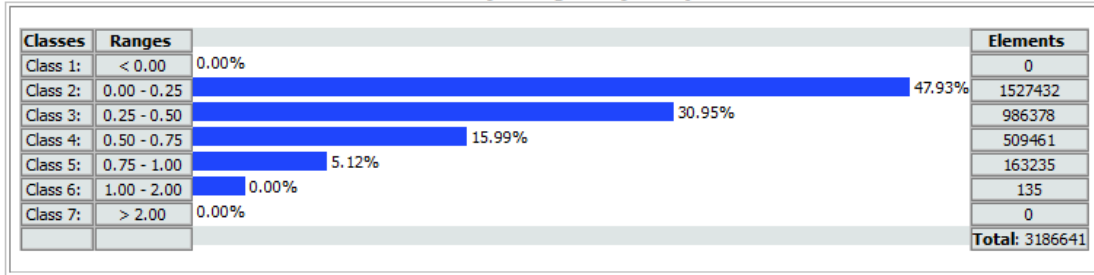
Figure 56: Big Model - Layers Mesh - Skewness Check

Solid Skewness (Tetras only) Graph

Classes	Ranges		Elements
Class 1:	< 0.00	0.00%	0
Class 2:	0.00 - 0.10	12.58%	390483
Class 3:	0.10 - 0.20	22.09%	685519
Class 4:	0.20 - 0.30	25.08%	778569
Class 5:	0.30 - 0.40	20.82%	646354
Class 6:	0.40 - 0.50	12.75%	395881
Class 7:	0.50 - 0.60	5.13%	159081
Class 8:	0.60 - 0.70	1.19%	36984
Class 9:	0.70 - 0.80	0.26%	7982
Class 10:	0.80 - 0.90	0.10%	3090
Class 11:	0.90 - 0.92	0.00%	48
Class 12:	0.92 - 0.95	0.00%	0
Class 13:	0.95 - 0.98	0.00%	0
Class 14:	0.98 - 0.99	0.00%	0
Class 15:	0.99 - 1.00	0.00%	0
Class 16:	1.00 - 1.00	0.00%	0
Class 17:	> 1.00	0.00%	0
			Total: 3103991

Figure 57: 3D Printed Model - Volume Mesh - Skewness Check

Solid Layers Quality Graph

Classes	Ranges		Elements
Class 1:	< 0.00	0.00%	0
Class 2:	0.00 - 0.25	45.11%	855524
Class 3:	0.25 - 0.50	30.97%	587280
Class 4:	0.50 - 0.75	17.66%	334847
Class 5:	0.75 - 1.00	6.25%	118557
Class 6:	1.00 - 2.00	0.01%	133
Class 7:	> 2.00	0.00%	0
			Total: 1896341
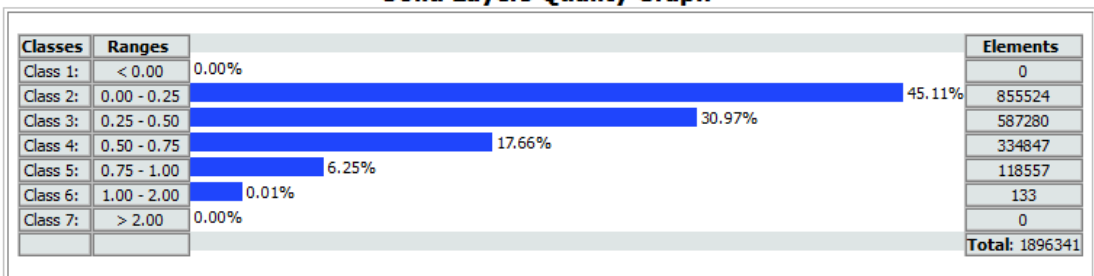
Figure 58: 3D Printed Model - Layers Mesh - Skewness Check

Solid Skewness (Tetras only) Graph

Classes	Ranges		Elements
Class 1:	< 0.00	0.00%	0
Class 2:	0.00 - 0.10	13.28%	1574431
Class 3:	0.10 - 0.20	22.64%	2684783
Class 4:	0.20 - 0.30	25.59%	3034193
Class 5:	0.30 - 0.40	20.56%	2437929
Class 6:	0.40 - 0.50	12.26%	1454110
Class 7:	0.50 - 0.60	4.63%	549219
Class 8:	0.60 - 0.70	0.90%	106989
Class 9:	0.70 - 0.80	0.11%	12893
Class 10:	0.80 - 0.90	0.02%	2418
Class 11:	0.90 - 0.92	0.00%	30
Class 12:	0.92 - 0.95	0.00%	0
Class 13:	0.95 - 0.98	0.00%	0
Class 14:	0.98 - 0.99	0.00%	0
Class 15:	0.99 - 1.00	0.00%	0
Class 16:	1.00 - 1.00	0.00%	0
Class 17:	> 1.00	0.00%	0
			Total: 11856995

Figure 59: F3 Model - Volume Mesh - Skewness Check

Solid Layers Quality Graph

Classes	Ranges		Elements
Class 1:	< 0.00	0.00%	0
Class 2:	0.00 - 0.25	63.93%	4163110
Class 3:	0.25 - 0.50	23.53%	1532363
Class 4:	0.50 - 0.75	10.52%	684947
Class 5:	0.75 - 1.00	2.02%	131790
Class 6:	1.00 - 2.00	0.00%	38
Class 7:	> 2.00	0.00%	0
			Total: 6512248

Figure 60: F3 Model - Layers Mesh - Skewness Check

3.3 Mesh Generation Procedure

All the meshes were generated through the batch mesh manager tool of the ANSA program. Every mesh generation consists of three scenarios (see Figure 61). The first scenario includes the surface meshing of the model. The second includes the creation of the boundary layers and the third, the volume mesh. The order mentioned above is important, as the surface mesh must be completed first, in order to generate the layers and finally the meshing of the remaining volume.
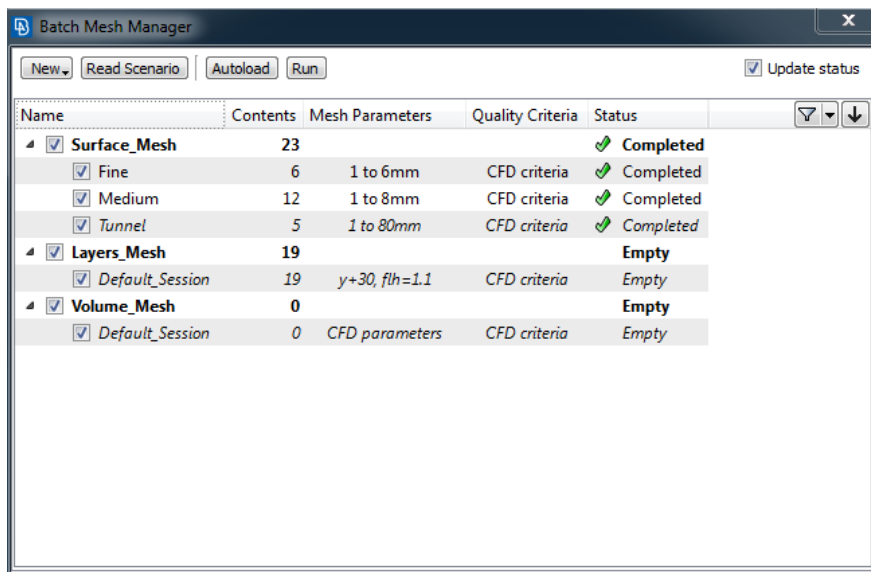
Figure 61: ANSA - Batch Mesh Manager

The surface mesh scenario usually includes different sessions in order to allow progressive surface meshing, from the areas with small element length to the areas of large element length. In this case there are 3 sessions: Fine, Medium, Tunnel. After naming the sessions the next step is the allocation of the geometry's PIDs to each one of them. The PID term describes the group of surfaces that belong to the same aerodynamic device. The allocation criteria are up to the engineer but usually they are two: the complexity of the geometry and the area of interest. For example, the front wing's PID will be placed in the fine session while the rear axle's PID in the medium session as it is easily understood that the axle's geometry is simpler than the front wing's, but also the front wing plays a very important role in the aerodynamic efficiency of the car, so a fine mesh is requested in this region. The surface mesh must be as smooth as possible to allow prism layers to be extruded from the surface of the examined geometry. The next step after the PIDs allocation is the determination of the mesh parameters of each session. In Figure 62 the mesh parameters are presented. The parameters that highly affect the mesh refinement

from one session to another are the minimum and maximum element length and the growth rate.
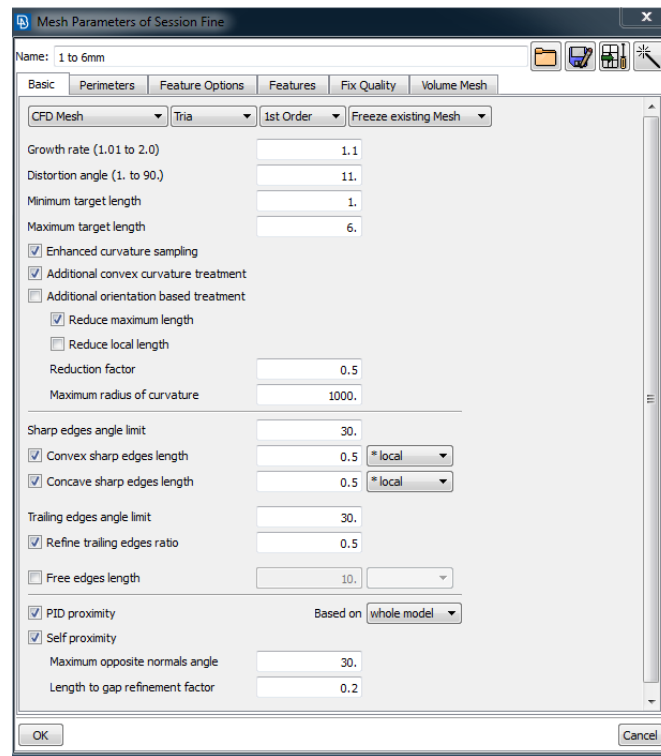
Figure 62: Mesh Parameters Window

The boundary layer mesh is extruded using the Advancing Front method, which extrudes layers consisting of tetrahedral elements from the surface faces into the specified core zone. Therefore, the first layer height and the growth rate must be specified based on the estimated boundary thickness of each case and placed in the respective field of the Layers Session (see Figure 64). To do a relatively accurate estimation of the first layer height and thus of the boundary thickness of the examined model, ANSA y+ calculator is used with a given velocity and the characteristic length of each geometry (see Figure 63). The relationship between the target y+, the free stream velocity and the first layer height were analyzed in 1.4.4.
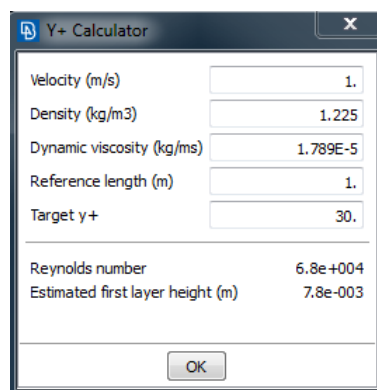
Figure 63: ANSA - y+ calculator
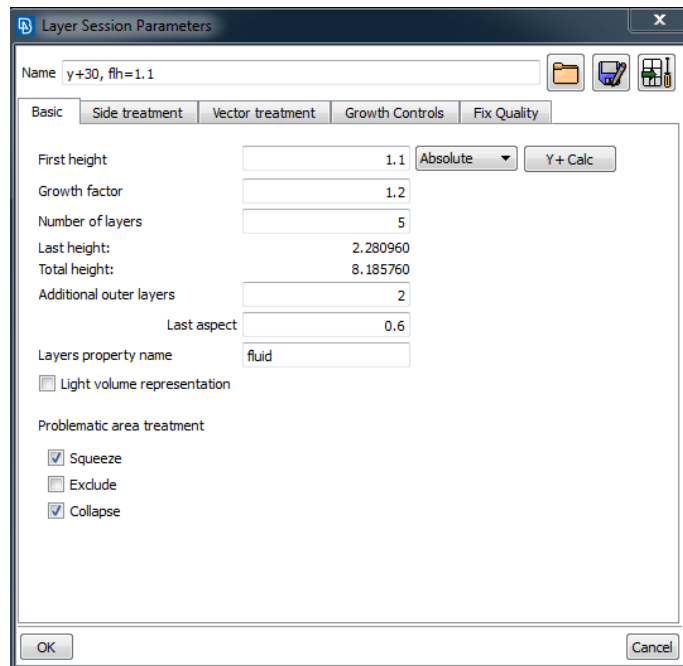
Figure 64: ANSA - Layers Session Parameters

The final stage of the meshing procedure is the generation of the volume mesh which is going to fill in the fluid domain with Tetrahedral or Hexahedral elements. Tetrahedral elements are solid elements which have been extracted from 2D triangular elements.
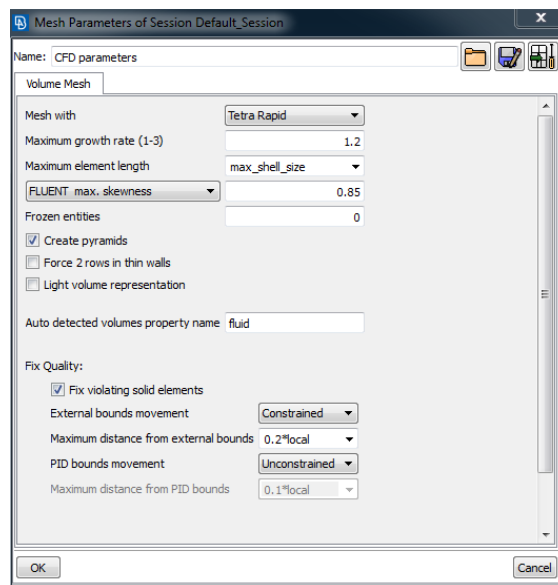
Figure 65: ANSA - Volume Mesh Parameters

Tetra Rapid is a volume meshing algorithm available in ANSA and was used for the creation of the volume mesh for all the models, which uses tetrahedral elements and pyramids if the surface mesh also contains quads. This type of elements is suitable for geometries of thick

Volumes or large domains with a significant variation in length along the surface mesh. This algorithm is specifically designed to handle large size CFD models and is bench marked to be 6 times faster than other algorithms (patented). The Maximum growth rate must be defined, which is the approximate growth factor of volume element size from layer to layer while the generation moves towards the interior of the Volume.

3.4 Simulated Cases Description

The purpose of the study was to compare our CFDs with the wind tunnel experiments, so that means that we had to simulate the "Big Model" and the 3D printed model for the same 5 wind tunnel speeds and compare the drag value to the one drawn from the experimental velocity profiles.

The whole point was to create a simulation formula whose setup and mesh size could be used for the development of aerodynamic devices of micro scale and full-scale formula type models. In order to optimize an aerodynamic package, it is necessary to conduct many comparative simulations in order to construct the design that gives maximum performance. Conducting comparative simulations needs computational time and when the computational resources are limited that means that someone must do a mesh independence and an iteration independence study in order to minimize the time needed to compare between the designs. These actions should also not work against the accuracy of the simulations and for this reason the engineer also should spend time on choosing the right turbulence model, wall functions, solver and the boundary layer refinement, meaning the target y+ and the first layer's height.

For all the above reasons the following CFD tests were done:

1. Iteration dependence for the "Big Model".
2. Mesh independence study for the "Big Model".
3. Mesh independence study for the "3D Printed Model".
4. Hexahedral vs Tetrahedral dominated grid for the "Big Model".
5. Hexahedral vs Tetrahedral dominated grid for the "3D Printed Model".
6. Standard vs Hybrid Initialization for the "Big Model"
7. k-ε vs k-ω comparison for the "Big-Model", using different y+ and first layer height values.
8. k-ε vs k-ω comparison for the "3D Printed", using different y+ and first layer height values.

All these steps helped in the clarification of the best mesh and setup combination.

3.5 Computational Test Matrix

In this section an aggregate matrix which contains all the simulations that were performed during the numerical study with their respective mesh details, boundary conditions and turbulence models is presented in Figure 66.

Study	Case	Model	y+	f/h	Element Type	Number of Elements	Turbulence Model	Inlet: Free Stream Velocity	Inlet: k	Inlet: ε or ω	Outlet: k	Outlet: ε or ω	Initialization Method	Iterations
Iteration Independence	1	Big	30	0.69	Tetras	11 millions	k-ε	15.2	0.313	0.399	0.313	0.399	Standard	4000
	2	Big	30	0.75	Tetras	11 millions	k-ε	13.8	0.264	0.330	0.264	0.330	Standard	4000
Mesh Independence	1	Big	30	0.69	Tetras	11 millions	k-ε	15.2	0.313	0.399	0.313	0.399	Standard	2000
	2	Big	30	0.69	Tetras	8 millions	k-ε	15.2	0.313	0.399	0.313	0.399	Standard	2000
	3	3D Printed	30	0.6	Tetras	8 millions	k-ε	15.2	0.436	1.336	0.436	1.336	Standard	2000
	4	3D Printed	30	0.6	Tetras	5 millions	k-ε	15.2	0.436	1.336	0.436	1.336	Standard	2000
Initialization Method Check	1	Big	30	0.69	Tetras	8 millions	k-ε	15.2	0.313	0.399	0.313	0.399	Standard	2000
	2	Big	30	0.69	Tetras	8 millions	k-ε	15.2	0.313	0.399	0.313	0.399	Hybrid	2000
Element Type Check	1	Big	30	0.69	Tetras	8 millions	k-ε	15.2	0.313	0.399	0.313	0.399	Standard	2000
	2	Big	30	1.1	Hexas	8 millions	k-ε	8.7	0.118	0.133	0.118	0.133	Standard	2000
k-ε Realizable vs k-ω SST	1	Big	30	0.99	Tetras	8 millions	k-ε	10.2	0.156	0.182	0.156	0.182	Standard	2000
	2	Big	30	0.87	Tetras	8 millions	k-ε	11.7	0.198	0.239	0.198	0.239	Standard	2000
	3	Big	30	0.87	Tetras	8 millions	k-ε	11.7	0.198	0.239	0.198	0.239	Standard	2000
	4	Big	30	0.75	Tetras	8 millions	k-ε	13.8	0.264	0.330	0.264	0.330	Standard	2000
	5	Big	30	0.69	Tetras	8 millions	k-ε	15.2	0.313	0.399	0.313	0.399	Standard	2000
	6	Big	1	0.038	Tetras	8 millions	k-ω	8.7	0.118	1.131	0.118	1.131	Standard	2000
	7	Big	1	0.033	Tetras	8 millions	k-ω	10.2	0.156	1.171	0.156	1.171	Standard	2000
	8	Big	1	0.029	Tetras	8 millions	k-ω	11.7	0.198	1.207	0.198	1.207	Standard	2000
	9	Big	1	0.025	Tetras	8 millions	k-ω	13.8	0.264	1.251	0.264	1.251	Standard	2000
	10	Big	1	0.023	Tetras	8 millions	k-ω	15.2	0.313	1.278	0.313	1.278	Standard	2000
	11	3D Printed	30	1	Tetras	5 millions	k-ε	8.9	0.162	0.437	0.162	0.437	Standard	2000
	12	3D Printed	30	0.86	Tetras	5 millions	k-ε	10.5	0.216	0.605	0.216	0.605	Standard	2000
	13	3D Printed	30	0.76	Tetras	5 millions	k-ε	12	0.273	0.787	0.273	0.787	Standard	2000
	14	3D Printed	30	0.64	Tetras	5 millions	k-ε	14.5	0.380	1.142	0.380	1.142	Standard	2000
	15	3D Printed	30	0.6	Tetras	5 millions	k-ε	15.7	0.436	1.336	0.436	1.336	Standard	2000
	16	3D Printed	1	0.033	Tetras	5 millions	k-ω	8.9	0.162	2.703	0.162	2.703	Standard	2000
	17	3D Printed	1	0.029	Tetras	5 millions	k-ω	10.5	0.216	2.803	0.216	2.803	Standard	2000
	18	3D Printed	1	0.025	Tetras	5 millions	k-ω	12	0.273	2.886	0.273	2.886	Standard	2000
	19	3D Printed	1	0.021	Tetras	5 millions	k-ω	14.5	0.380	3.008	0.380	3.008	Standard	2000
	20	3D Printed	1	0.02	Tetras	5 millions	k-ω	15.7	0.436	3.061	0.436	3.061	Standard	2000
First Layer Height Independence	1	Big	30	0.69	Tetras	8 millions	k-ε	8.7	0.118	0.133	0.118	0.133	Standard	2000
	2	Big	30	0.69	Tetras	8 millions	k-ε	10.2	0.156	0.182	0.156	0.182	Standard	2000
	3	Big	30	0.69	Tetras	8 millions	k-ε	11.7	0.198	0.239	0.198	0.239	Standard	2000
	4	Big	30	0.69	Tetras	8 millions	k-ε	13.8	0.264	0.330	0.264	0.330	Standard	2000
	5	Big	30	0.69	Tetras	8 millions	k-ε	15.2	0.313	0.399	0.313	0.399	Standard	2000
	6	Big	1	0.023	Tetras	8 millions	k-ω	8.7	0.118	1.131	0.118	1.131	Standard	2000
	7	Big	1	0.023	Tetras	8 millions	k-ω	10.2	0.156	1.171	0.156	1.171	Standard	2000
	8	Big	1	0.023	Tetras	8 millions	k-ω	11.7	0.198	1.207	0.198	1.207	Standard	2000
	9	Big	1	0.023	Tetras	8 millions	k-ω	13.8	0.264	1.251	0.264	1.251	Standard	2000
	10	Big	1	0.023	Tetras	8 millions	k-ω	15.2	0.313	1.278	0.313	1.278	Standard	2000
F3 Simulations	1	F3	30	0.74	Tetras	18 millions	k-ε	8.7	0.087	0.039	0.087	0.039	Standard	2000
	2	F3	30	0.74	Tetras	18 millions	k-ε	10.2	0.115	0.053	0.115	0.053	Standard	2000
	3	F3	30	0.74	Tetras	18 millions	k-ε	11.7	0.147	0.070	0.147	0.070	Standard	2000
	4	F3	30	0.74	Tetras	18 millions	k-ε	13.8	0.196	0.097	0.196	0.097	Standard	2000
	5	F3	30	0.74	Tetras	18 millions	k-ε	15.2	0.232	0.117	0.232	0.117	Standard	2000
FSAE Car - Straight	1	Amphion	30	0.72	Tetras	28 millions	k-ε	16	0.243	0.108	0.243	0.108	Standard	4800
FSAE Car - Cornering	1	Amphion	30	0.87	Tetras	85 millions	k-ε	-	-	-	-	-	Hybrid	4800

Figure 66: Computational Test Matrix of the Numerical Study

The boundary conditions of the final simulation of the matrix is marked with - because the simulation was initialized using planes with data drawn from previously solved cases. More information is provided in section 3.17.2.

All the results and the comparisons made between the simulations of the computational matrix are presented below.

3.6 Simulation Setup Analysis

In the following section the steps of the simulation setup will be analyzed. The procedure will be described through an example were the "Big Model" is simulated at the free stream velocity of 15.2 (m/s), using the k-e turbulence model. The aim is to provide the reader with all the basic steps that he can take to conduct an aerodynamic simulation, using Fluent, while providing all the information and arguments to support our choices.

Step 1: This is the first stage of the setup after the implementation of the mesh in the program. At first the user clicks on the check button in order to detect any kind of mesh trouble which was not understood during the mesh procedure. Secondly the user clicks on the report quality button which will give an overview of the mesh quality after checking the criteria that were analyzed on the section of the mesh quality. This command also gives the chance to improve the quality of the mesh, only with respect to the cell squish (orthogonality) criterion. So, if any poor areas, with orthogonal quality below 0,165039%, exist, then the user can repair them using the "mesh-repair" TUI command. Unfortunately, if left-handed of negative volume cells, or high skewness and aspect ratios exist and make the problem unsolvable then the user must return to the post processor in order to fix it. What follows the mesh improvement are the solver settings. In this case we choose a pressure-based solver since the density is constant and there are no compression phenomena. The velocity formulation is chosen as absolute since there is no relative motion in our control volume. Finally, the time is set as steady for obvious reasons.
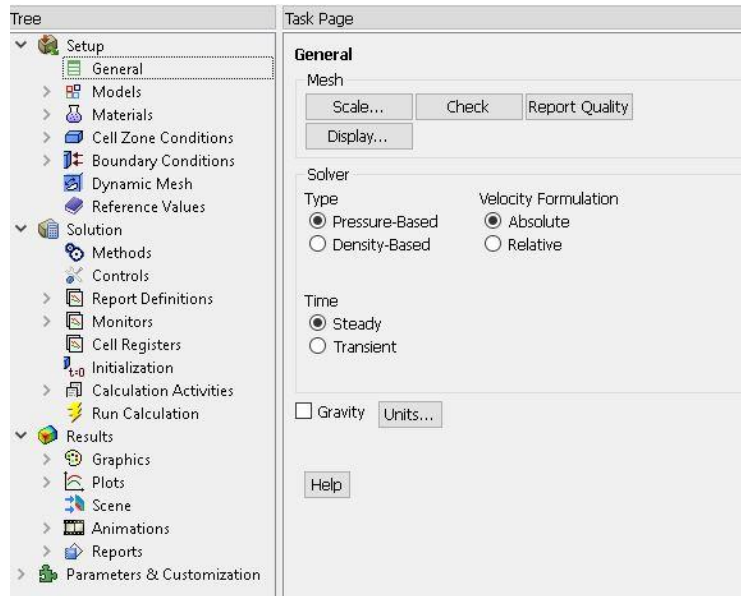
Figure 67: Mesh quality check, improvement and solver setting.

Step 2: In this step the user chooses the turbulence model and the wall functions. The two turbulence models that were compared were the k-e Realizable with Standard wall functions and the k-w SST model, whose differences and functionalities were analyzed before.
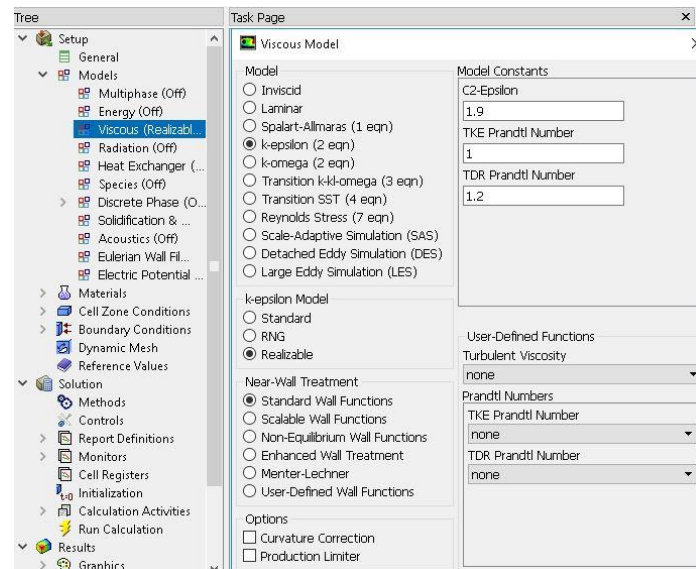
Figure 68: Turbulence Model Choice

Step 3: At this stage, the user can define the boundary conditions at the inlet and the outlet. The computational mesh includes a series of faces which coincide with the boundaries of the physical domain under consideration. The conditions there are prescribed through the boundary conditions [Jasak, 1996]. There are 3 boundary conditions at the inlet and 2 at the outlet. At the inlet, the user has to define the free stream velocity, the turbulent kinetic energy and the

turbulent dissipation rate / specific dissipation rate (if k-ω is applied). At the outlet he has to define only the turbulent kinetic energy and the turbulent dissipation rate/specific dissipation rate, which in reality have the same values as the inlet, since at the outlet the free stream is considered to have reached a free stream, as it has a long distance from the car. The k, e and w values at the boundary are calculated from the following algebraic equations:

$$\text{➤} \quad k = \frac{3}{2} \cdot (U \cdot I)^2$$

where I is the turbulent intensity given by: $I = 0.16 \cdot \text{Re}^{-\frac{1}{8}}$, with Re being the local Reynolds number.

$$\text{➤} \quad \varepsilon = 0.09^{\frac{3}{4}} \cdot k^{\frac{3}{2}} \cdot l^{-1}$$

where l is the turbulent/integral length, estimated by: $l = 0.07 \cdot L$

$$\text{➤} \quad \omega = \frac{\varepsilon}{(k \cdot 0.09)}$$

The characteristic length (L) that was used for all the calculations above was the car's length since the flow was external.
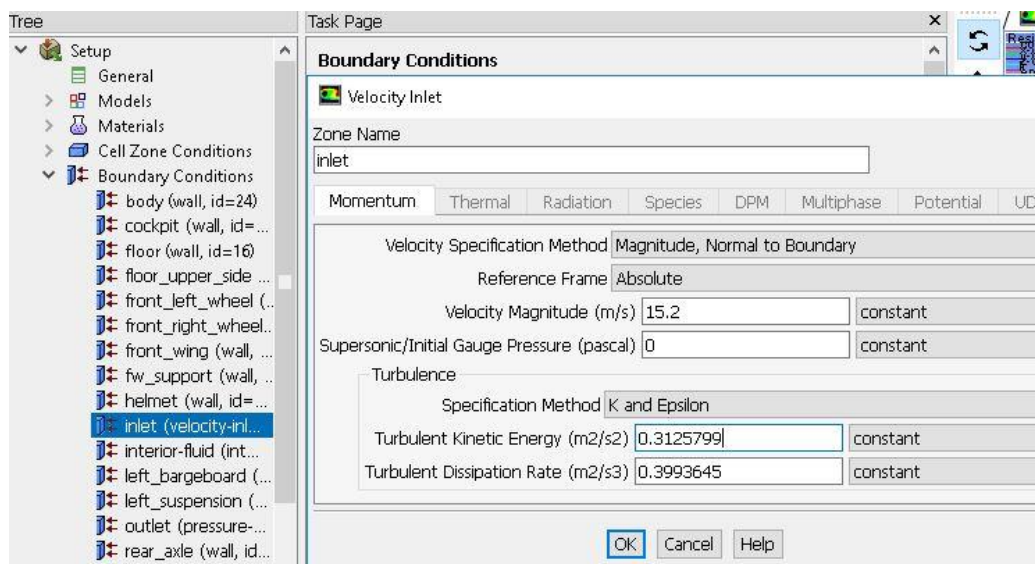
Figure 69: Inlet boundary condition
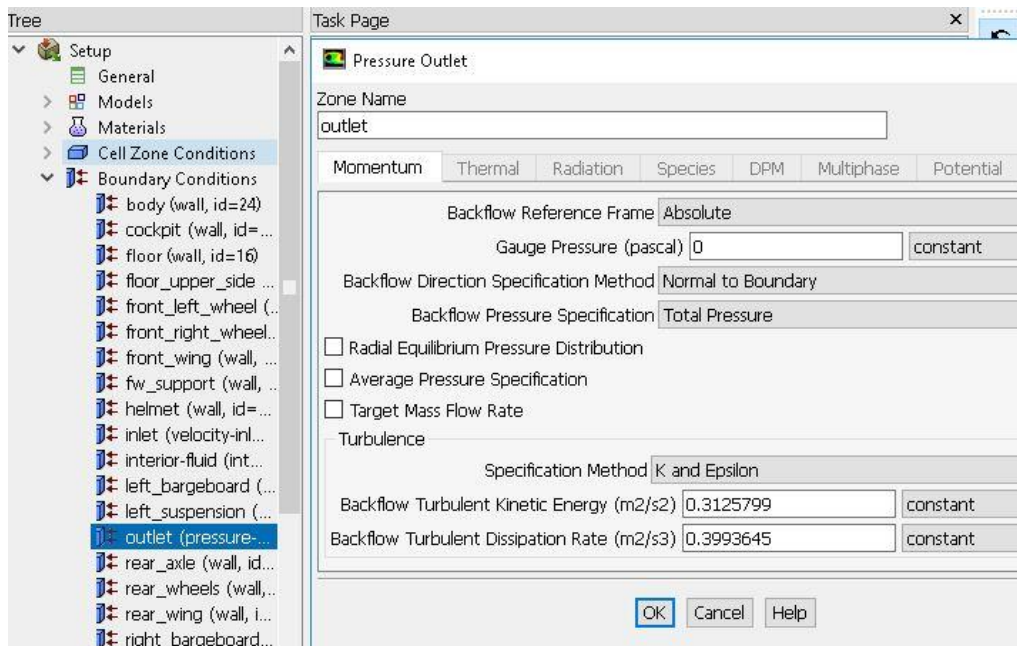
Figure 70: Outlet boundary condition

Step 4: At this step the user selects the solution algorithm, the interpolation method for the gradients calculation and the discretization schemes of the incompressible N.S. equations and the turbulence model equation. In this specific simulation the SIMPLE algorithm was selected as it is the most common CFD algorithm, the green gauss node based for the gradient calculations and the second order upwind in order to achieve higher accuracy.
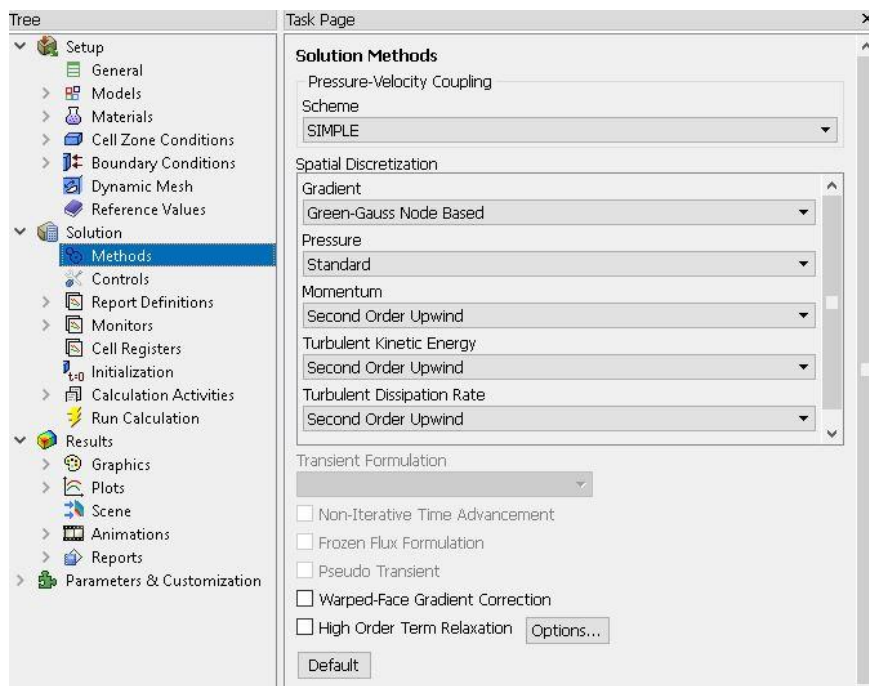
Figure 71: Solution solver and discretization method choice

Step 5: At this stage, the user selects the values of the relaxation factors. As it is seen from the figure below the ω values for the density and the body forces is 1 since there are no body forces in this problem and the density is constant. Since the user is not able to calculate the optimal ω through the mathematical expression that was given in the section were the under-relaxation method is analyzed, he has to perform simulations using different ω values for each equation and choose not only the one that leads faster to a converged solution but also to a realistic result.
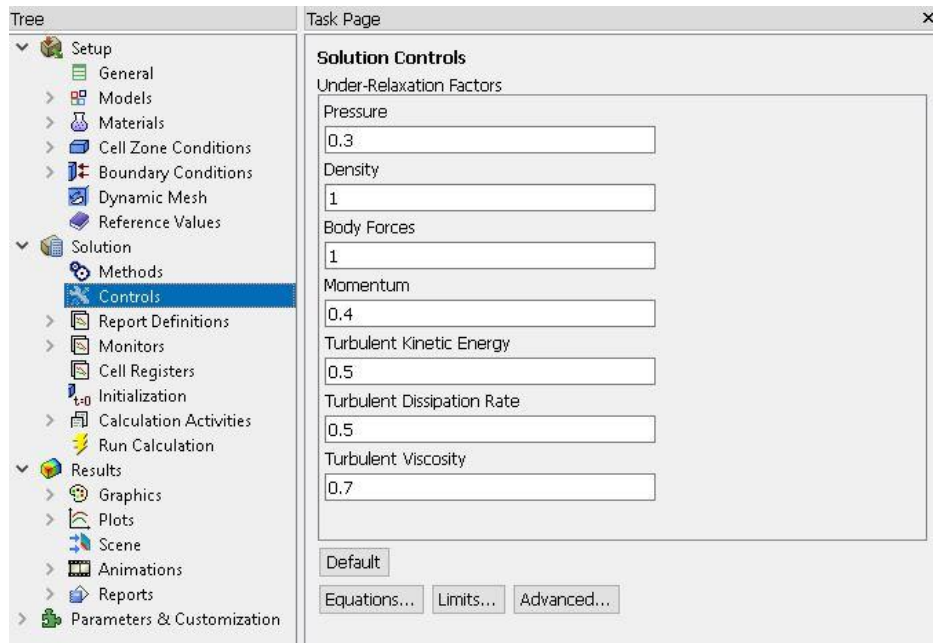
Figure 72: Relaxation factors choice

Step 6: At this step, the user can plot any kind of physical quantity that the program is able to calculate, at the solution's monitor. This is done because the user must keep an eye on not only in the residuals error order but also the divergence of the physical quantities of interest, in order to understand if convergence has been reached. In this simulation the variables of interest are the drag and lift.
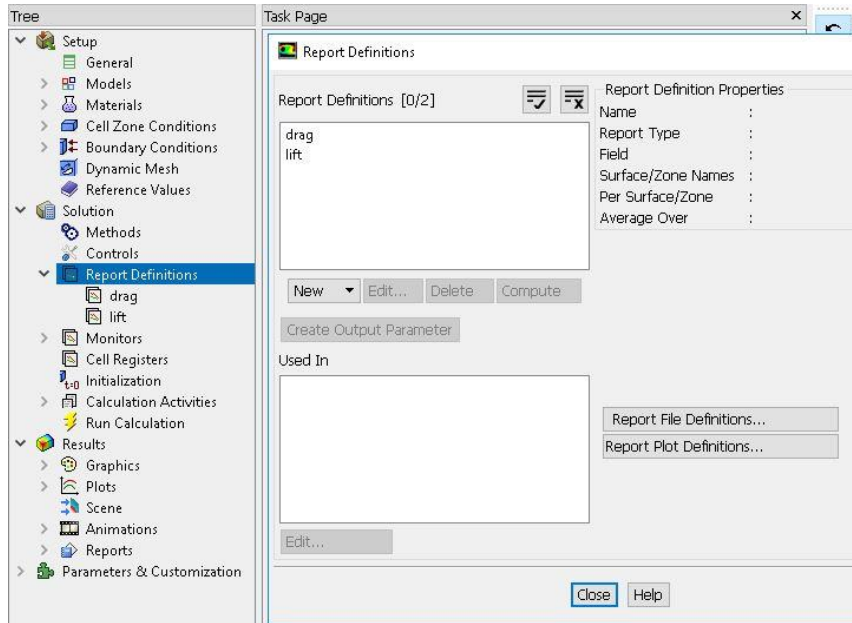
Figure 73: Report definitions plotting

Step 7: The Fluent program has convergence criteria based on the on the residuals of the equations that are solved. Even though we are interested in achieving a minimization of the solution's residual, we considered the solution to be converged when the drag and lift values have very small divergence within a consecutive number of iterations. For this reason, we set a very low residual order for the pressure equation which is difficult to be obtained in this kind of simulations, in order to create a ceaseless bronchus. This action prevents the solution from stopping before the completion of all the iterations that have been specified by the user.
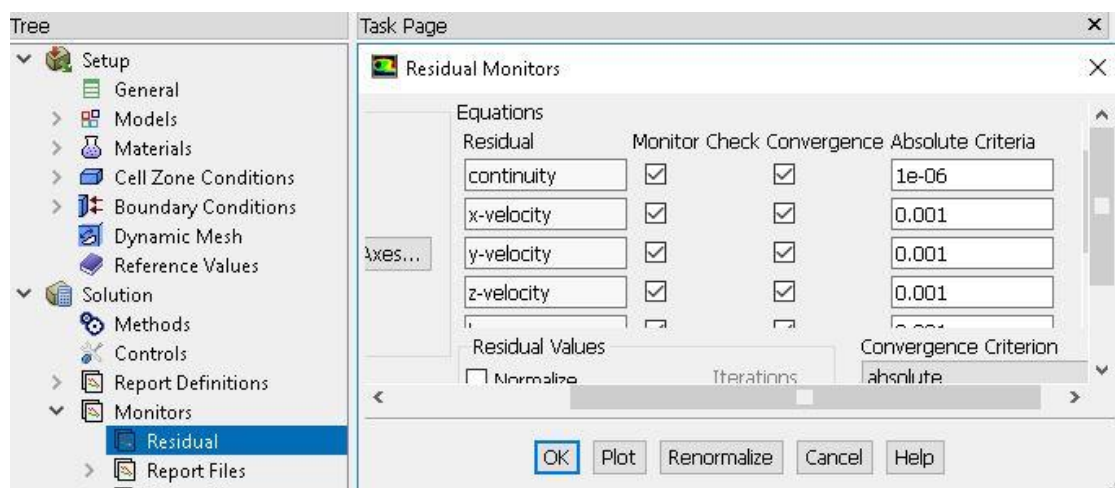
Figure 74: Convergence criteria choice

Step 8: At this stage, the user initializes the solution before proceeding with the solving procedure.
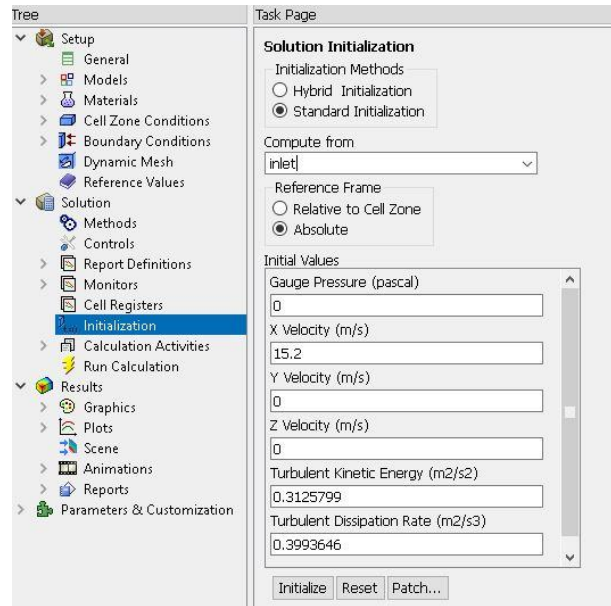
Figure 75: Initialization method choice

Step 9: At this stage, the user sets the total number of iterations that are needed in order to reach a converged solution, but before proceeding with the calculation he also has to click the "Check Case" button in order to detect any kind of setup mistakes or mesh quality problems.
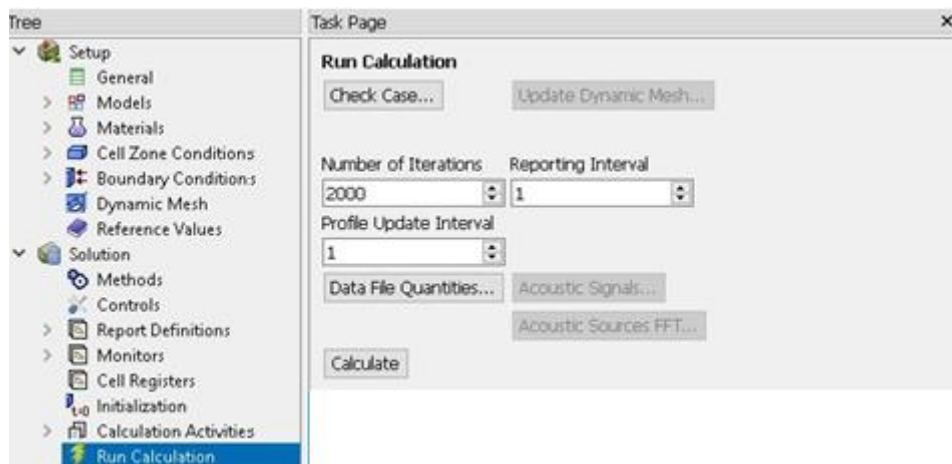
Figure 76: Case check and iterations number choice

If any check case message appears, which informs the user about the skewness exceeding an acceptable limit, then the program advices the user to improve the quality of the mesh in order to avoid a problematic solution. Unfortunately, when the engineer deals with complex geometries of a racecar, such problems might appear, so he should investigate the number of

elements that violate the skewness criterion. According to ANSYS 18.1 Meshing User's Guide and ANSYS Meshing Application Introduction, Appendix A, Mesh Quality, in some circumstances the pressure-based solver in Fluent can handle meshes containing a small percentage of cells with skewness ~ 0.98. So, if the number of cells, with skewness around 0.98, is substantial with respect to the total number of computation cells, then message may be ignored and proceed with the simulation when a pressure-based solver is used. Otherwise, he must go back to the meshing procedure, detect the problematic region and remesh. The percentage limit of the violating cells is not specifically defined by ANSYS but according to relevant experience it should be kept below 0.001%, to avoid numerical diffusion.

3.7 Simulations Convergence Criterion

Unfortunately, in the CFD bibliography there are no specific convergence criteria. The engineer, depending on the problem that he is dealing with, should identify the quantities of interest, which in this problem is the drag and check how the quantity is changing within consecutive iterations. If the change is very small, for example if an average change of 0.00006 (N) is detected between consecutive iterations, then this will result in a 0.12 (N) change after 2000 iteration which also a relatively small change considering the number of iterations, so the engineer can consider his solution to be converged. This argument can also be supported by the residuals plot and of course by the post processing which can help him identify possible solution errors. This approach was adopted for the conduction of the iteration dependence and the mesh independence study, in this thesis. Such methods are also supported by the bibliography [Tips and Tricks, Convergence and Mesh Independence Study, LEAP Australia]

3.8 Iteration Dependence Study

This was another test in favor of the computational time saving. Two separate simulations were conducted for 2 different free stream velocities (10.2 and 15.2 m/s) using the geometry of the "Big Model". The simulations were conducted for 4000 iterations and the following results aroused.
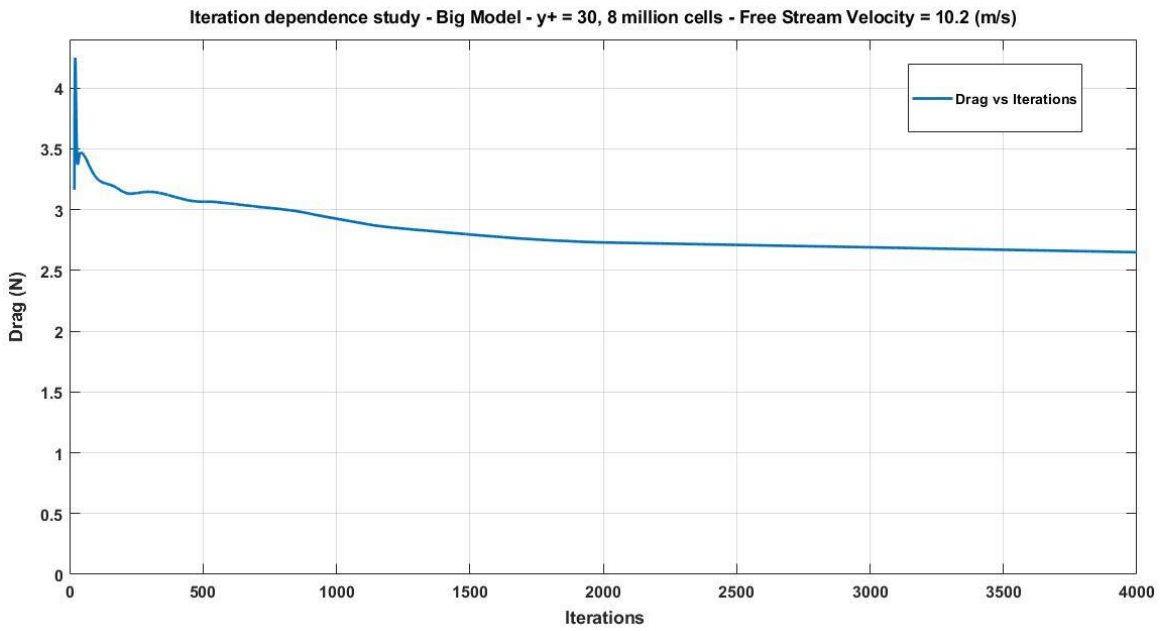
Figure 77: Drag vs Iteration, for 10.2 (m/s), from 0 to 4000 iterations.
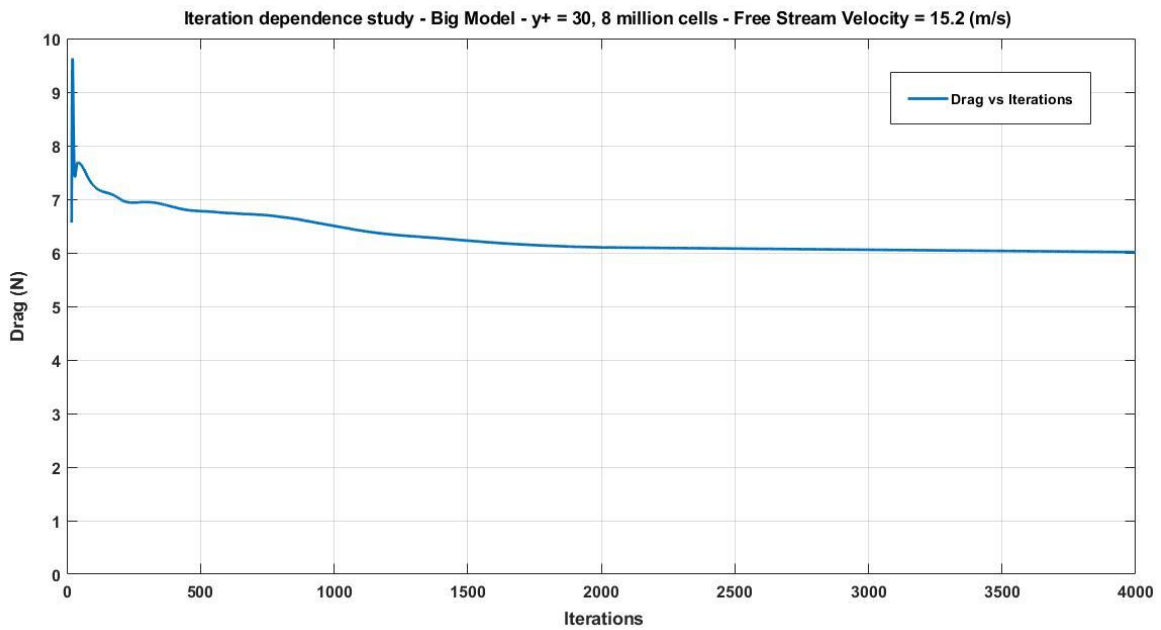
Figure 78: Drag vs Iteration for 15.2 (m/s), from 0 to 4000 iterations.

The conclusion from the plots above is that the drag divergence for the 10.2 (m/s) case was 1.68% and for the 15.6 case 1.65%. The divergence percentage for each of the two cases was calculated by the following equation: $\dfrac{|Drag\_Value_{2000} - Drag\_Value_{4000}|}{Drag\_Value_{4000}} \cdot 100$, where the number indicators refer to the iteration from which the drag value was drawn. The divergence percentage was almost the same for both cases and at the same time relatively small, so the iteration number for all the simulations was chosen to be 2000. The computational time was 8 hours for the first 2000 iterations and 14 hours for the 4000 iterations, using a mesh size around 8.5 million cells. This resulted in a 43% computational time reduction.

3.9 Mesh Independence Study

The purpose of this study was to choose the mesh size that would be applied to the 2 geometries in order to save computational time during the final simulations, for the different free stream speeds and the comparison of the CFD drag values to the drag measured in the wind tunnel. In the following tables all the information about the surface and the volume mesh is provided.

Table 7: Surface mesh properties

Surface Mesh - Number of Elements		
Geometry	**Coarse**	**Fine**
Big Model	539130	740508
3D Printed Model	516834	713330

Table 8: Volume mesh properties

Volume Mesh - Number of Cells		
Geometry	**Coarse**	**Fine**
Big Model	8223844	11362075
3D Printed Model	5125223	8355550

The mesh size difference for both models is around 3 million cells. The free stream velocity at which the different meshes were simulated was 15.2 (m/s) while the k-ε model for all 4 simulations was used. The following results came out of the 4 simulations.
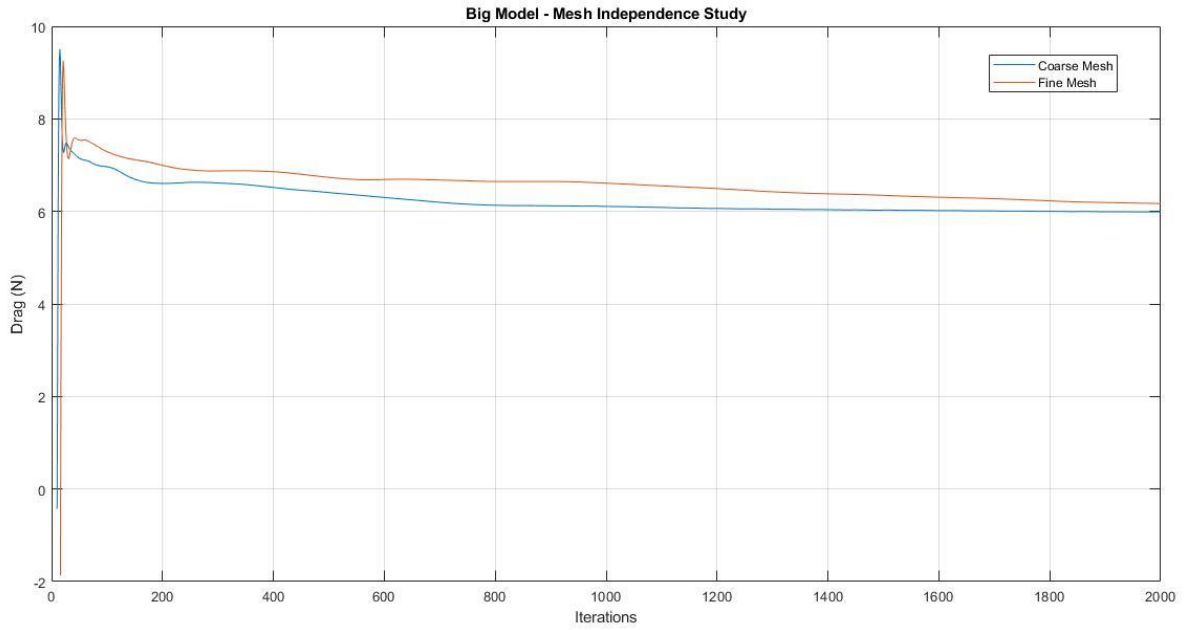
Figure 79: Coarse vs Fine Mesh - Big Model
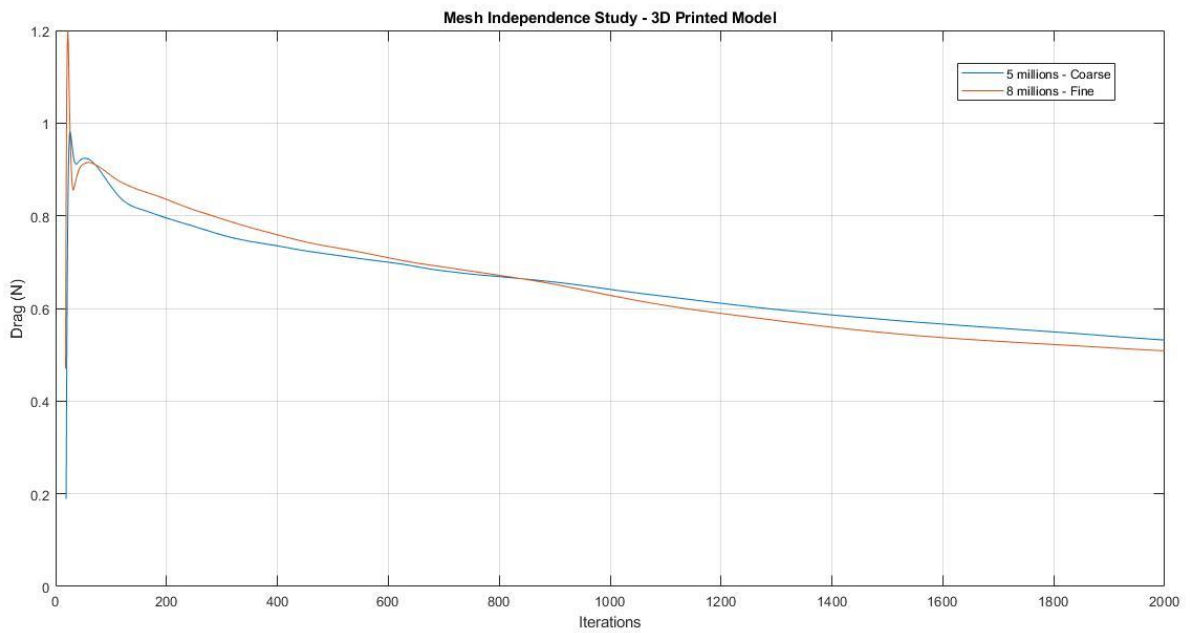
Figure 80: Mesh Independence Study – 3D Printed Model

Both in the "Big Model" and the 3D Printed Model the drag after 2000 iterations, between the coarse and the fine mesh changes by 1.13% and 2.2%. The discrepancy percentage was

calculated using the following equation: $\dfrac{\left|Drag_{fine} - Drag_{coarse}\right|}{Drag_{fine}} \cdot 100$ and the reason why the

drag value of the fine mesh is put on the denominator is the fact that the fine mesh is expected to give a more reliable and accurate result than the coarse mesh. As it also seen from Figure 79 and Figure 80, the change in the drag value is very small so in both cases the coarser meshes were chosen in order to simulate the models for different free stream velocities. In terms of computational time, the 5 million cells of the 3D Printed Model needed 3.5 hours in order to converge while the 8 million cells of the Big Model 8 hours, using the k-ε and 12 hours using the k-ω. All the simulations were conducted using the k-ε Realizable Model and a y+=30.

3.10 Initialization Dependence Study

As it is understood, from Figure 75, the user has two choices. He can either initialize the solution by applying the variable values that were given at one boundary to all the cell centroids, using the standard initialization or he can use the hybrid initialization. The difference is that by applying the hybrid initialization command, the solver starts an initial solution of the flow field while keeping the pressure variable constant and solving for the other variables, for a specific number of iterations (the default number of iterations is 10). Based on the solver's guide the standard initialization is chosen for cases where the flow field can be easily described and predicted through algebraic equations and the hybrid initialization in cases where that is not possible. In this case the standard initialization seemed more suitable since at the inlet the free stream flow can be easily predicted. To verify this argument the same simulation was done using the two methods. For both simulations the Big Model with a mesh of 8 million cells was used. The free stream velocity was 15.2 (m/s) while the k-ε model was used. After gathering the results, two different plots were created. The first plot represents the drag value difference during the first 30 iterations and the second the difference during rest of the 1970 iterations.
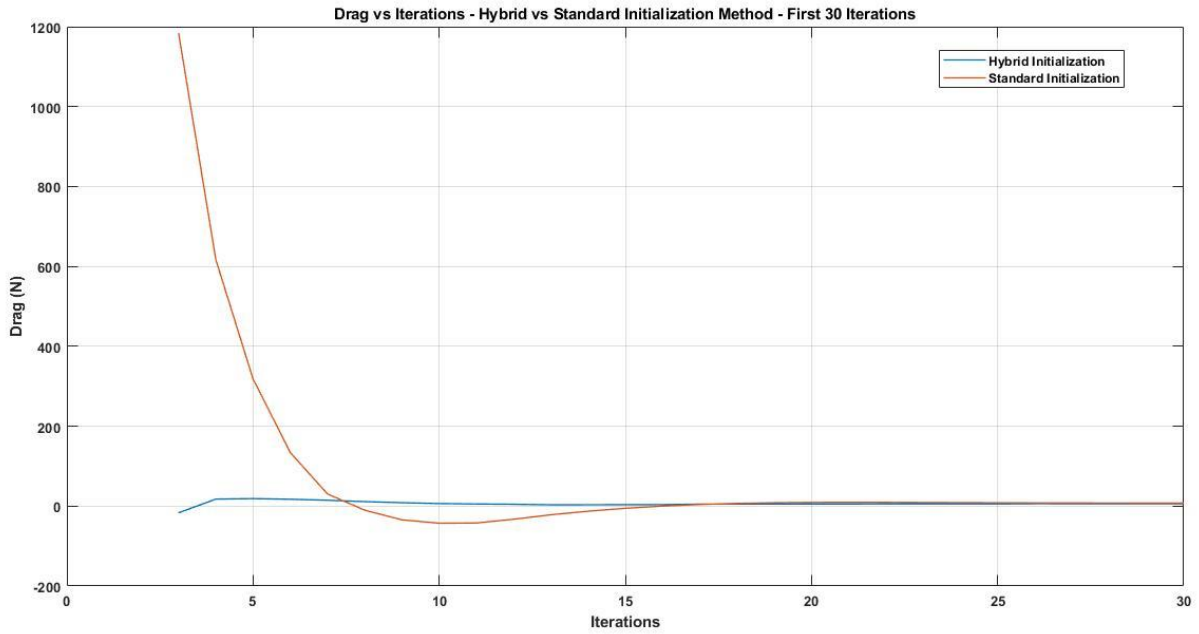
Figure 81: Hybrid vs Standard Initialization Method - First 30 iterations

From Figure 81 it is understood that both methods give unrealistic drag values considering the size of the model, with the Standard method containing 41% bigger error than the Hybrid method, with respect to the drag value, at which both CFD cases converge. The error estimation for each case was done using the following equation: $e_i = \dfrac{|x_i - 5.68|}{5.68} \cdot 100$.
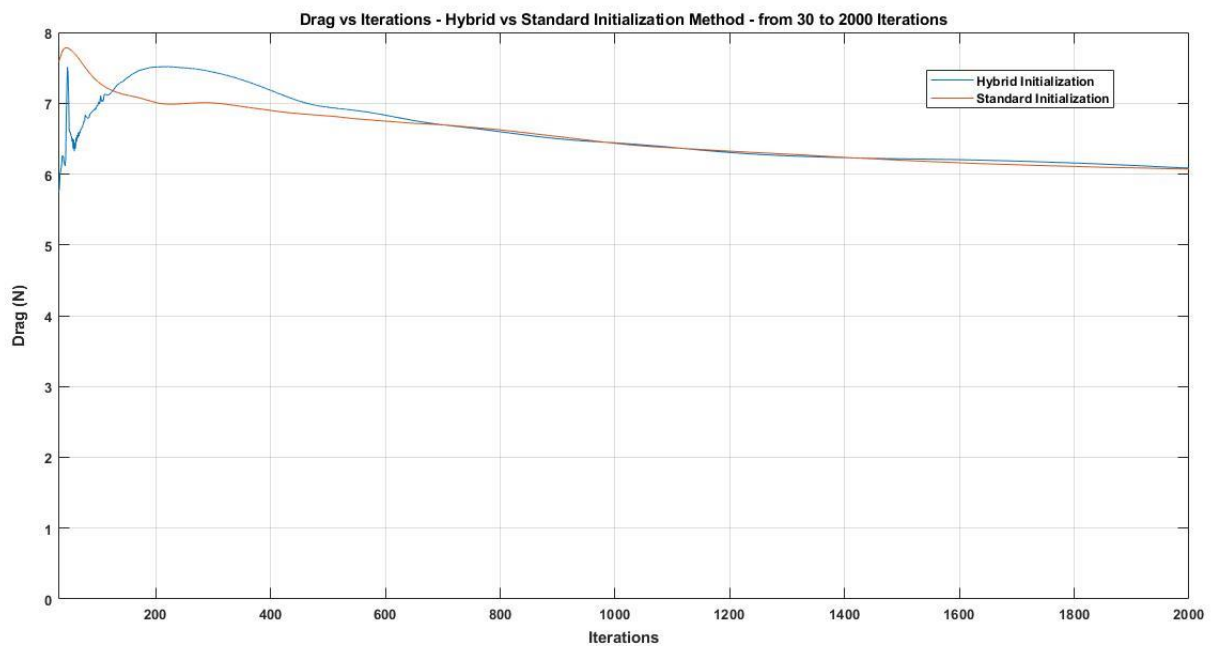
Figure 82: Hybrid vs Standard Initialization Method - Final 1970 iterations

From Figure 82 it is understood that after the 30 iterations both solutions have reached a realistic value for drag and as the solution continuous, they converge to the same value. The drag value of the Big Model at the 2000 iteration was 5.68 (N) for both methods. The conclusion is that either method could be used but since the experiment verified the argument over the standard method, all the simulations were conducted using this method.

3.11 Hexahedral vs Tetrahedral Mesh

Hexahedral meshes having the same size with tetrahedral dominated control volumes tend to yield better accuracy and faster convergence. For this reason, we performed a simulation with a hexahedral dominated volume of the "Big Model" and compared it to the tetrahedral mesh. Both meshes contained about 8 million cells and the simulation time for 2000 iteration was almost 8 hours for both, since the k-ε model was used. The comparison between the two meshes is done in the following figure:
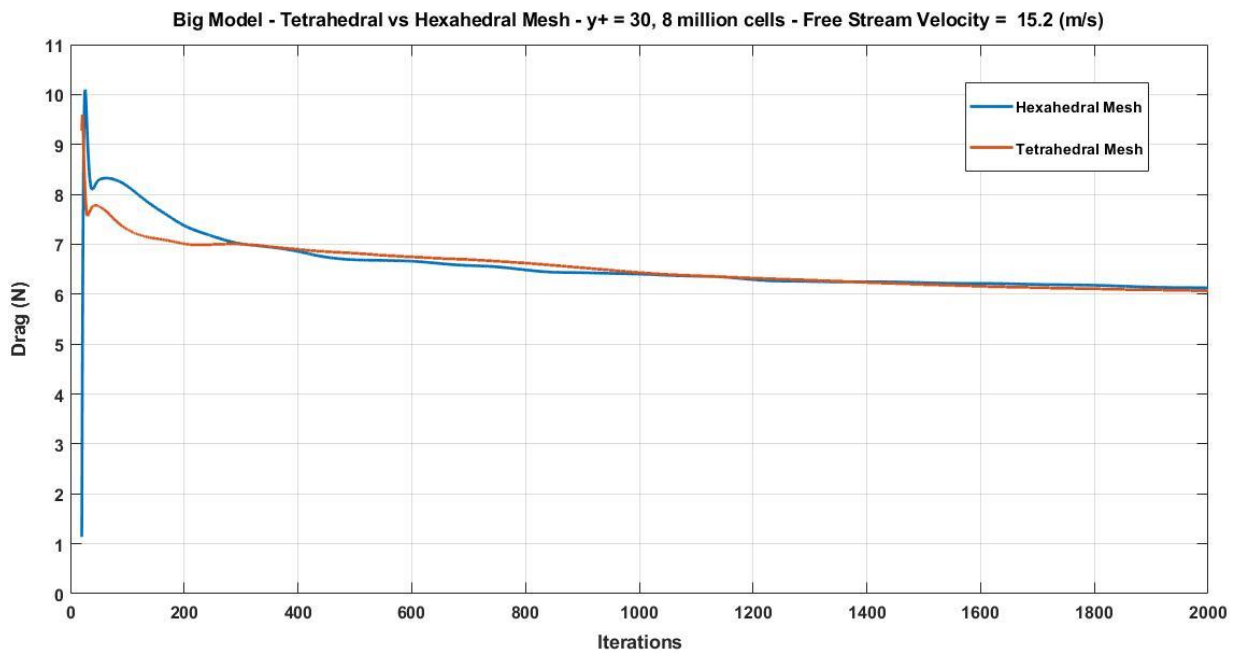
Figure 83: Hexahedral vs Tetrahedral Mesh CFD results comparison

The only difference between the 2 meshes is that the hexahedral mesh over-predicts the model's drag for the first 250 iterations but after this point, up until the 2000 iteration where the simulation is considered converged, the behavior between the two is identical. Before making a conclusion about which element type should be used, the similar behavior of the two meshes should also be investigated through the post processing, by analyzing the physics of the flow field. In the following figures a comparison between the total pressure, the static pressure and

the velocity magnitude is done in order to confirm that there was no difference between the two types of mesh:
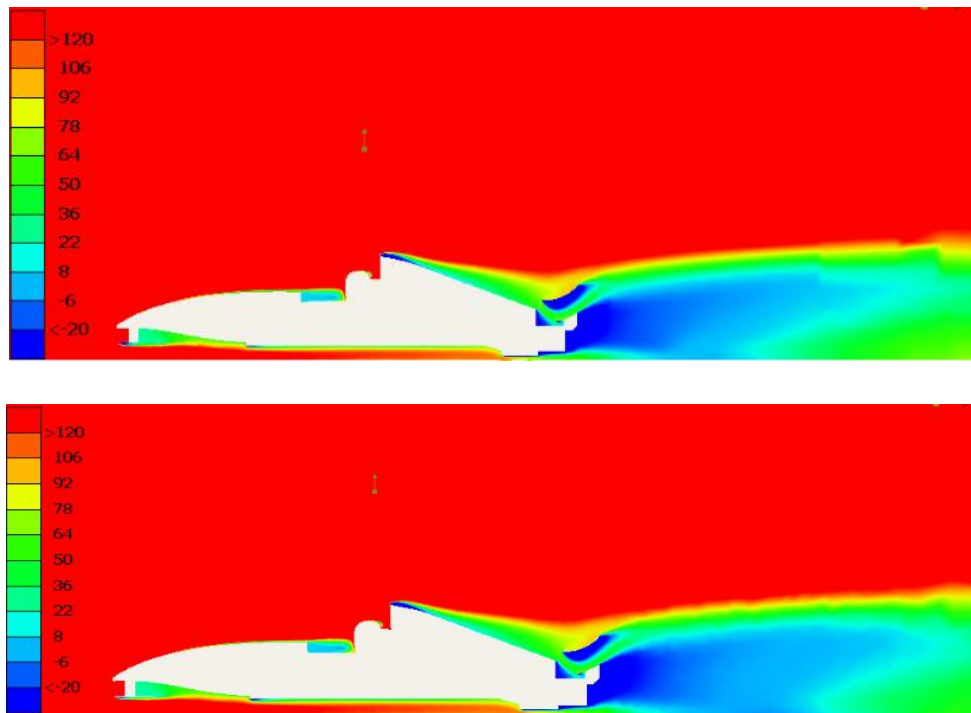
Figure 84: Total pressure symmetry cut planes comparison – Hexahedral Mesh (Top) vs Tetrahedral Mesh (Bottom)
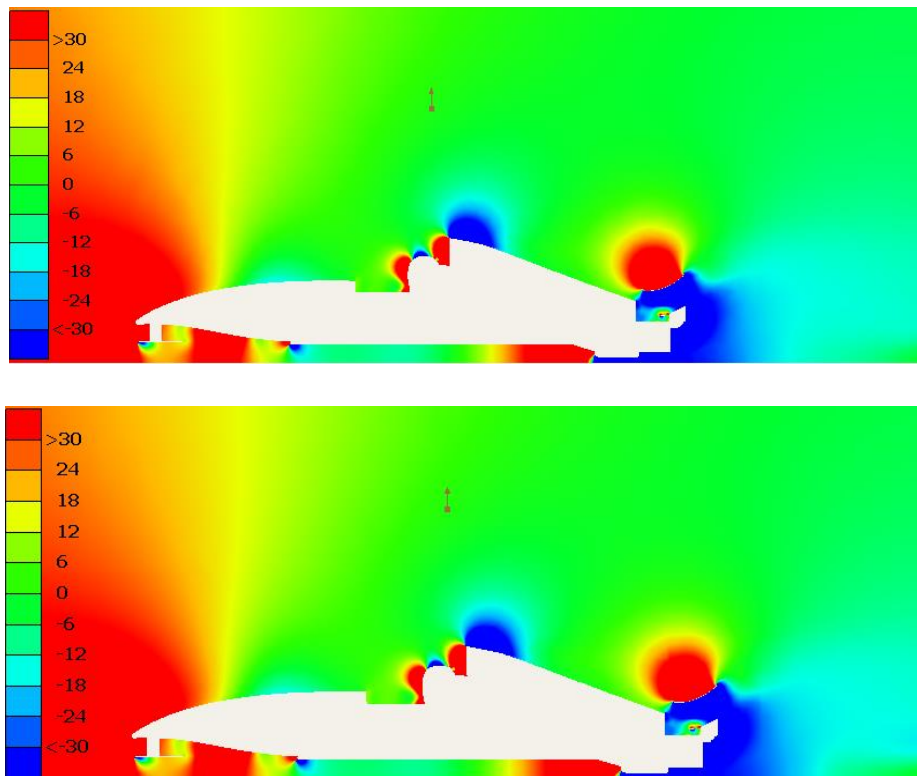
Figure 85: Static Pressure symmetry cut planes comparison – Hexahedral Mesh (Top) vs Tetrahedral Mesh (Bottom)

At this point no emphasis will be given on the aerodynamic efficiency and the weak areas of model because this is not the point of the simulation. Both the total and the static pressure planes are the same in both cases and if specific areas of the model either below or behind the car, are investigated. Since the lowest ride height of the car is experienced, the pressure field is the same in the stagnation point that is created before the fluid enters the diffuser. Behind the car the size and the magnitude of the car's wake are also identical in the two cases.

3.12 k-ε and k-ω comparison

The two equation models were compared for five free stream velocities and for both geometries. This resulted in a total number of 20 simulations. The boundary conditions for the turbulence models at the inlet and the outlet were the following:

Table 9: Turbulence Model Values for the boundaries

Turbulence Model Parameters			
Big Model			
Free Stream Velocity (m/s)	k (m^2/s^2)	ε (m^2/s^3)	ω (1/s)
8.7	0.118	0.133	1.131
10.2	0.156	0.182	1.171
11.7	0.198	0.239	1.207
13,8	0.264	0.330	1.251
15.2	0.313	0.399	1.278
3D Printed Model			
Free Stream Velocity (m/s)	k (m^2/s^2)	ε (m^2/s^3)	ω (1/s)
8.9	0.162	0.437	2.703
10.5	0.216	0.605	2.803
12	0.273	0.787	2.886
14.5	0.380	1.142	3.008
15.7	0.436	1.336	3.061

After the completion of the simulations the following results were obtained:

Table 10: "Big Model" k-ε Realizable and k-ω SST results

Big Model - Different first layer height, y+=30 (k-e), y+=1 (k-w)			
Free Stream Velocity (m/s)	WT Drag (N)	CFD Drag (N)	
		k-ε	k-ω
8.7	1.56	2.00	1.95
10.2	2.08	2.76	2.7
11.7	2.66	3.63	3.51
13.8	4.16	5.08	4.95
15.2	5.06	6.17	5.93

Table 11: "Big Model" k-ε Realizable and k-ω SST results divergence

Big Model– Results Divergence		
WT vs k-ε %	WT vs k-ω %	k-ε vs k-ω %
28	25	2
33	30	2
36	32	3
22	19	3
22	17	4
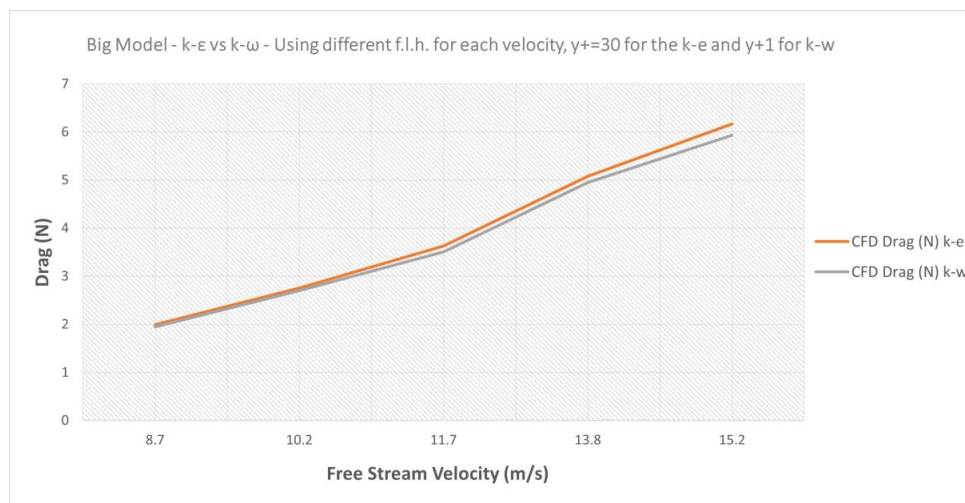
Figure 86: k-ε Realizable vs k-ω SST model results comparison for the "Big Model"

Table 12: "3D Printed Model" k-ε Realizable and k-ω SST results

3D Printed Model - Different first layer height, y+=30 (k-e), y+=1 (k-ω)			
Free Stream Velocity (m/s)	WT Drag (N)	CFD Drag (N)	
		k-ε	k-ω
8.9	0.24	0.16	0.15
10.5	0.29	0.22	0.21
12.0	0.36	0.29	0.27
14.5	0.64	0.43	0.40
15.7	0.69	0.51	0.46

Table 13: "3D Printed Model" k-ε Realizable and k-ω SST results divergence

3D - Results Divergence			
Free Stream Velocity (m/s)	WT vs k-ε %	WT vs k-ω %	k-ε vs k-ω %
8.9	33	38	6
10.5	24	28	5
12.0	19	25	7
14.5	33	38	7
15.7	26	33	10
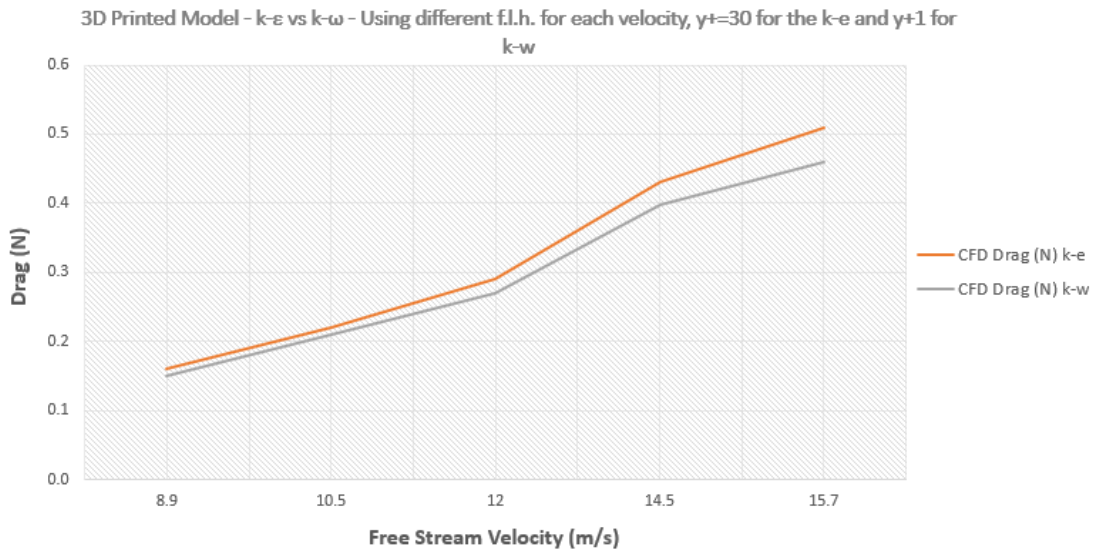
Figure 87: k-ε Realizable vs k-ω SST model results comparison for the "3D printed Model"

The conclusion concerning the k-ε and the k-ω models is the same in both cases. There is a very small divergence between the two, 3% for the "Big Model" and 7% for the "3D Printed Model", with the k-ε over predicting the drag in both cases. Since the difference between the two was substantial the k-ε model is chosen for comparative simulations because for the same number of iterations the simulations using the k-ε model lasted for 8 hours while the k-ω simulations for 12.

Since we cannot draw the conclusion just from the drag comparisons it was important to do a post processing between a k-ε (y+=30), a k-ω (y+=1) and k-ω (y+=30) simulation for the same free stream velocity (13.8 m/s) and compare the flow fields. All the figures below have been collected from the post processing of the "Big Model".
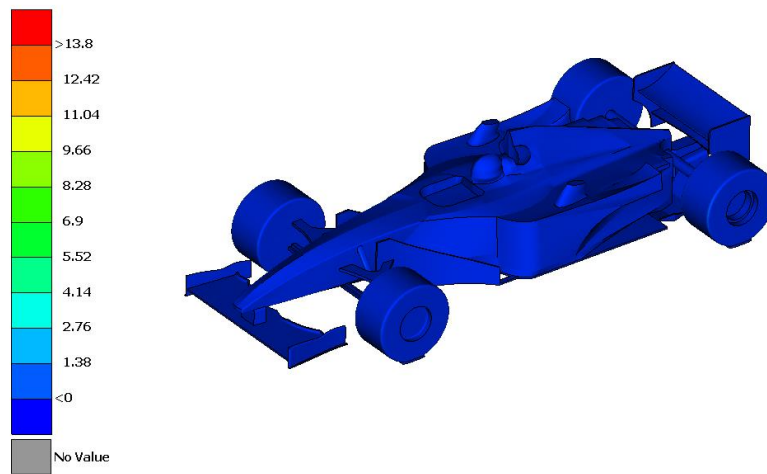
Figure 88: Big Model, using y+1 and k-ω - Velocity Magnitude (m/s)
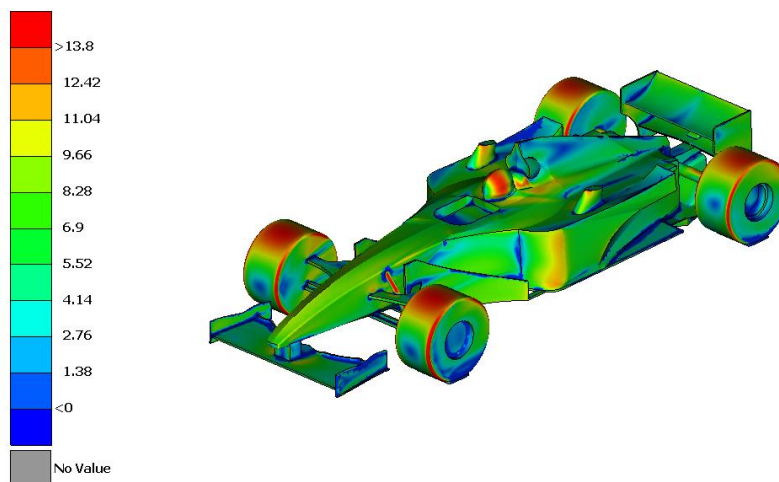
Figure 89: Big Model, using y+30 and k-ε - Velocity Magnitude (m/s)
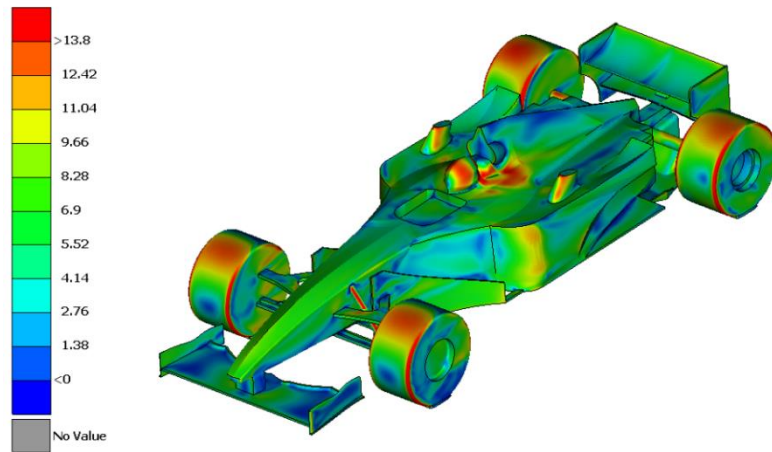
Figure 90: Big Model, using y+30 and k-ω - Velocity Magnitude (m/s)

From Figure 88 it is understood that the application of a very low y+ value results in a solution very close to the wall and that's why the velocity magnitude on the car's surface is zero. This is the real condition in any case since the user is applying the no-slip condition on the wall, but when using a y+>30, that results in a first layer height placed outside the viscous sub-layer. So Figure 89 and Figure 90 represent the velocity magnitude some mm above the wall.

In Figure 91, Figure 92 and Figure 93 the wall shear stress of the 3 compared cases are presented. Watching Figure 91 we understand the k-ω SST model predicts better the separation regions on the front wing, the rear wing the bargeboards and to the bodywork area in front of the rear wing. These areas are spotted with the blue color which in the k-ω SST case have a value closer to zero. Zero wall shear stress means separation. On the other hand, in Figure 92 the over prediction of the wall shear stress by the k-ε model is confirmed since the same areas have a higher value ranging between 0 and 0.3 Pascal.

Comparing Figure 92 and Figure 93 we understand that the k-ε model with Standard wall function and the k-ω SST model for a common y+=30 produce almost the same results as far as the wall shear stress is concerned.
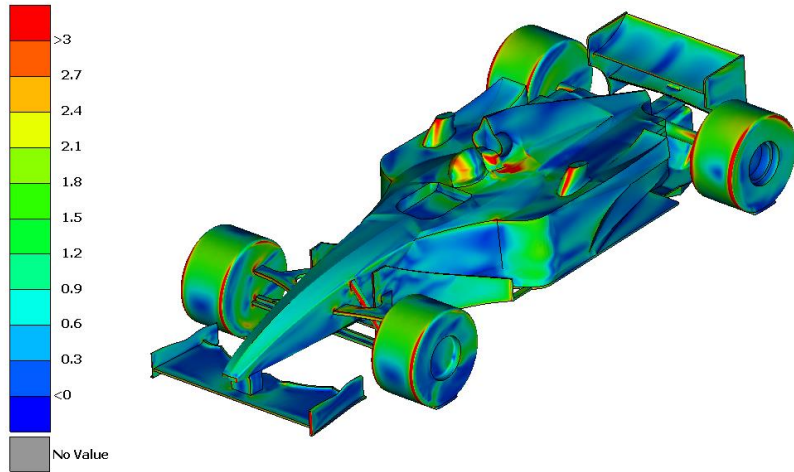
Figure 91: Big Model, using y+1 and k-ω - Wall Shear Stress (Pa)
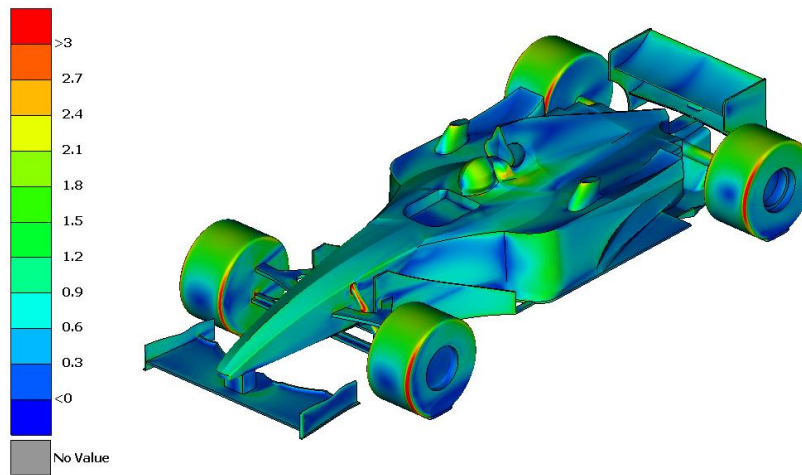
Figure 92: Big Model, using y+30 and k-ε - Wall Shear Stress (Pa)
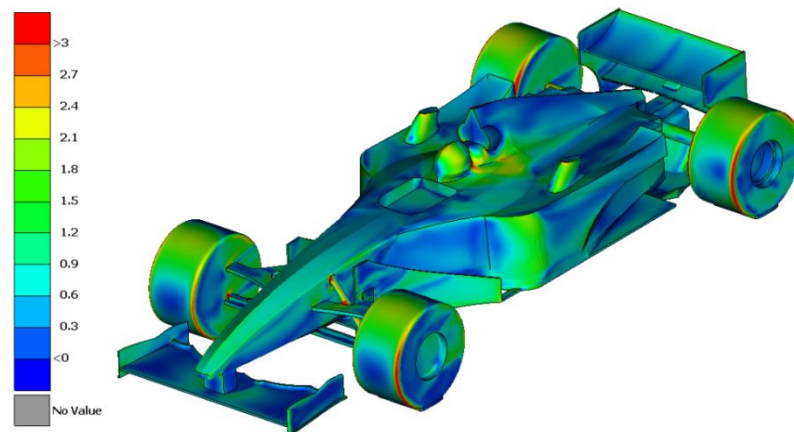
Figure 93: Big Model, using y+30 and k-ω - Wall Shear Stress (Pa)
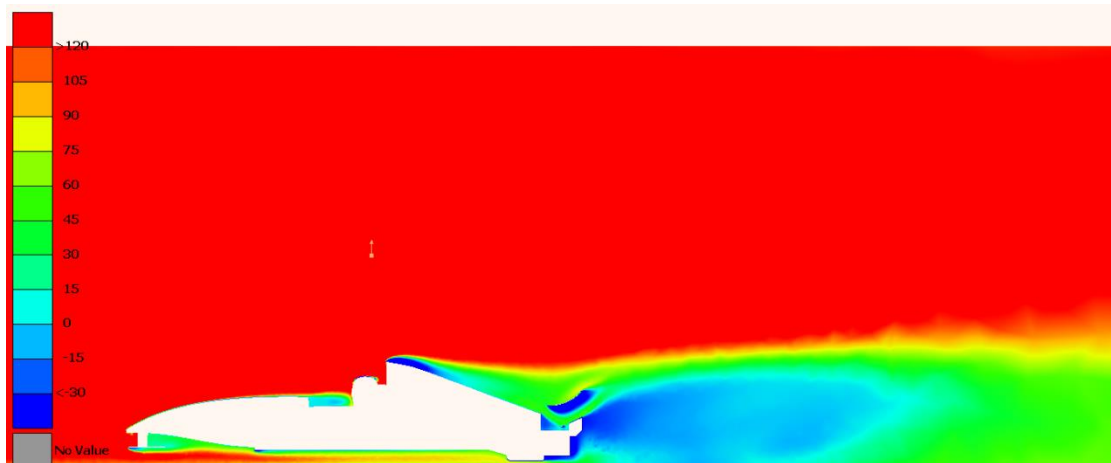
Figure 94: Big Model, using y+1 and k-ω - Total Pressure
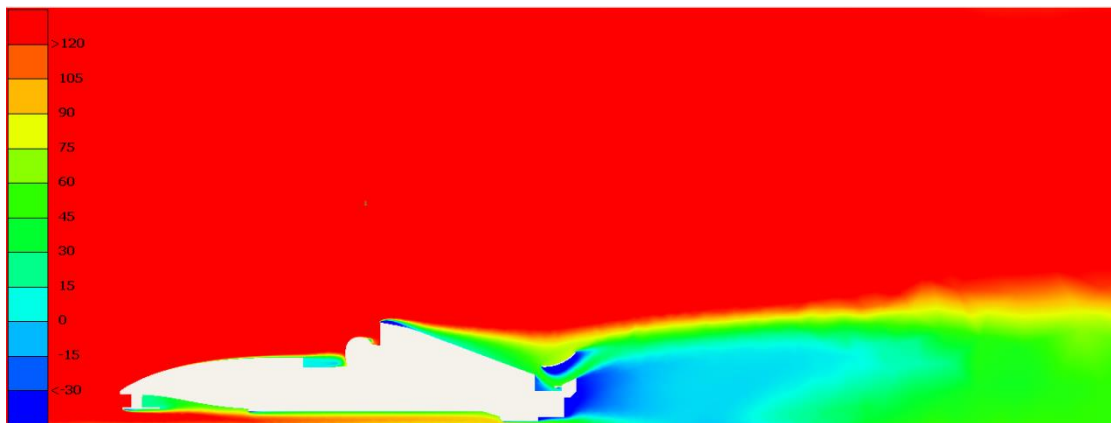
Figure 95: Big Model, using y+30 and k-ε - Total Pressure
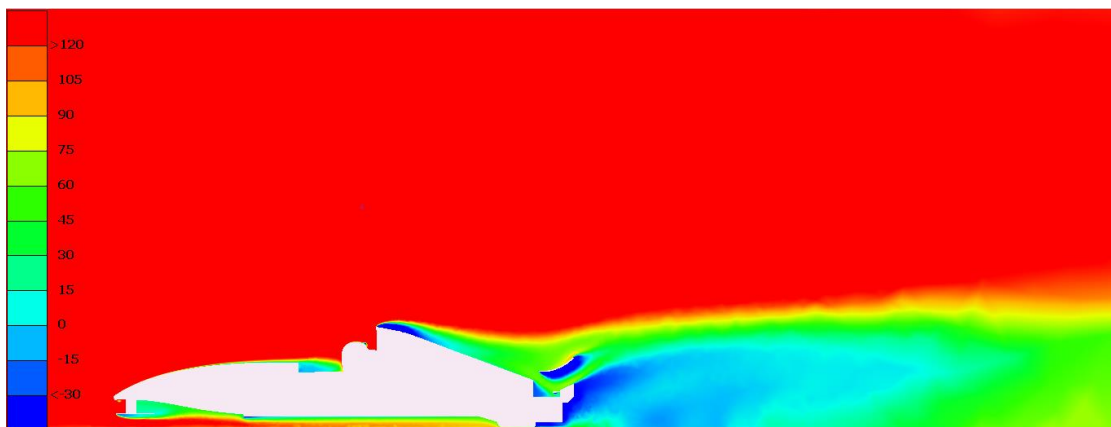
Figure 96: Big Model, using y+30 and k-ω - Total Pressure

The total pressure sections at the middle of the car, are similar in each one of the above simulations. The low energy region behind the car has almost the same expansion and this is something that proves the small divergence between the drag values, calculated by the k-ε and the k-ω models. Moreover, the pressure difference between the upper and the lower side is small, which is something that explains why the model is not producing any downforce.
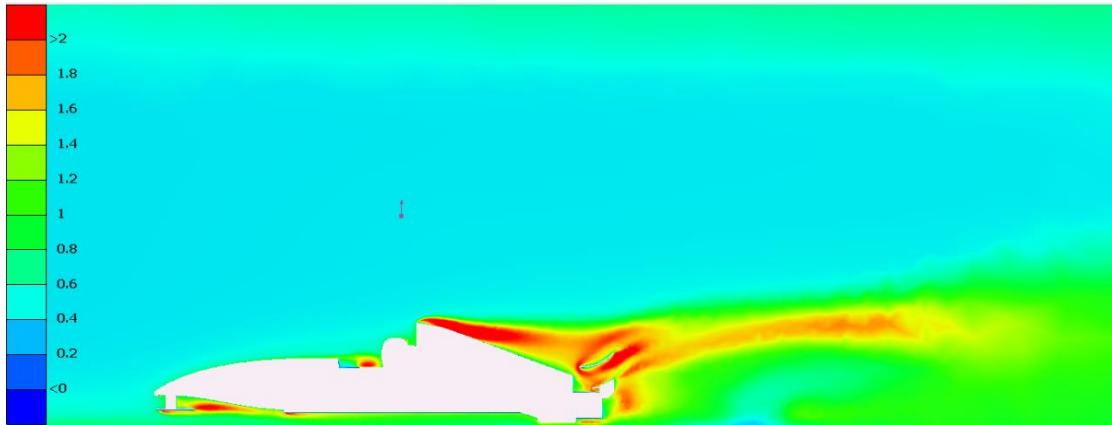
Figure 97: Big Model, using y+1 and k-ω - Turbulent Intensity
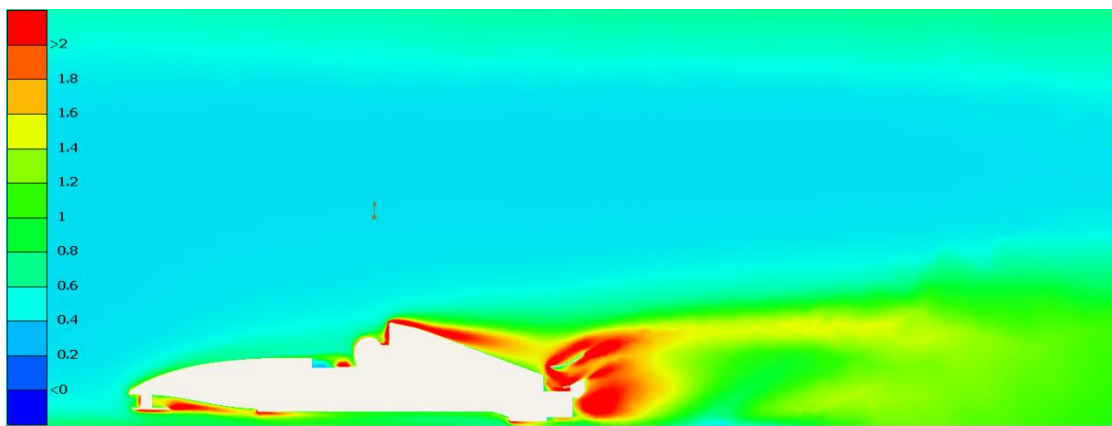
Figure 98: Big Model, using y+30 and k-ε - Turbulent Intensity
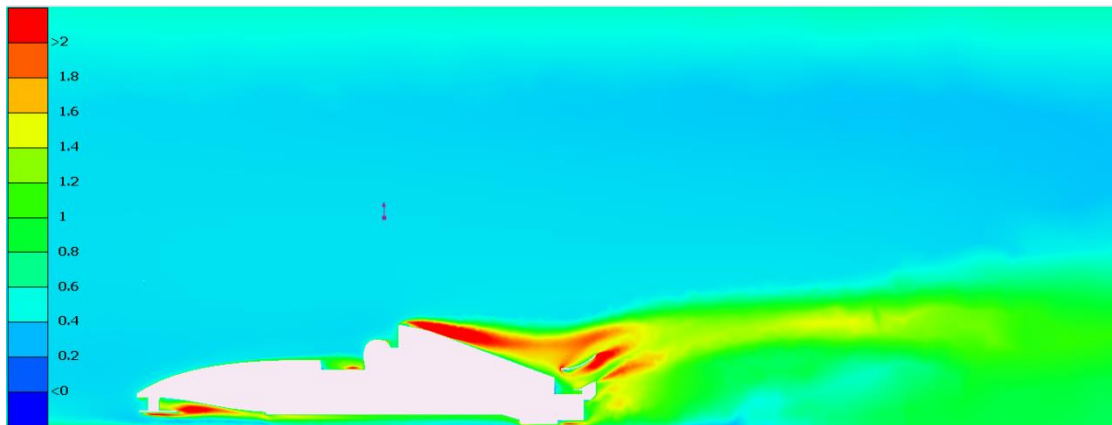
Figure 99: Big Model, using y+30 and k-ω - Turbulent Intensity

Studying the turbulent intensity plot in Figure 98, the k-ε shows a much higher intensity both in the regions around the rear wing's element, but also right behind the rear wing's support, which is not seen in the cases where the k-ω model is applied. Another important observation is that turbulent intensity has a value between 0.4 and 0.6 in the region in front of the car. This happens because of the boundary layer development on the "road" surface, which, when the car

is running on track, does not exist. The good thing is that it proves the disturbance of the boundary layer when taking the lower measurements in front of the car with the anemometer. Moreover, we see that the disturbance rises to a height which almost at the limit of the car's ride height but not below the 10% of the ride height.
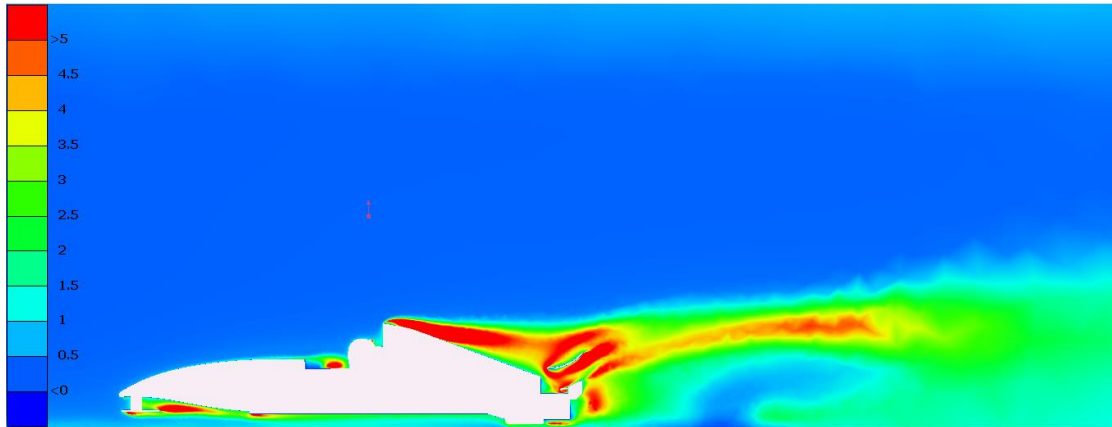
Figure 100: Big Model, using y+1 and k-ω - Turbulent Kinetic Energy
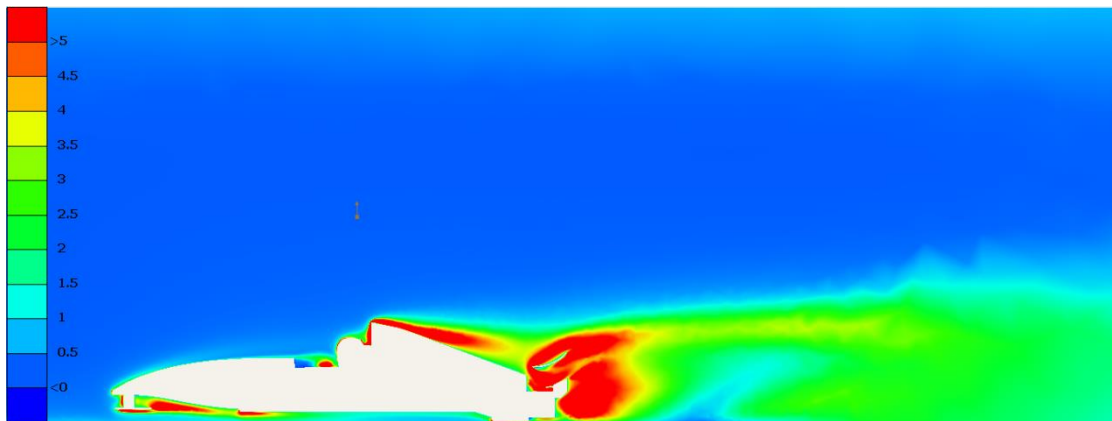
Figure 101: Big Model, using y+30 and k-ε - Turbulent Kinetic Energy
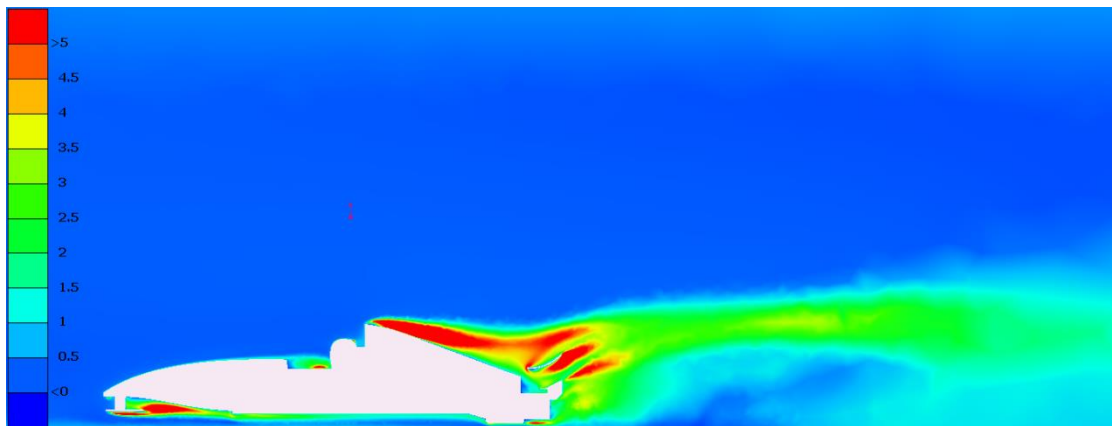
Figure 102: Big Model, using y+30 and k-ω - Turbulent Kinetic Energy

The turbulent kinetic energy is proportional to the turbulent intensity so the behavior of the flow concerning the turbulence is also imprinted in the above plots. Another observation that can be spotted is the k-ω model presents an expanded low turbulence region behind the car, which in the case of the k-ε is roughly spotted.

3.13 Control Volume Equilibriums Check

In order to further check the validity of the 20 simulations, which were conducted for the comparison of the k-ε and the k-ω turbulence models by using the coarser tetrahedral dominated meshes for each model, y+=30 for the k-ε, y+=1 for the k-ω and a different first layer height (see section 1.4.4, for more information). For each free stream velocity, the mass flow rate, static pressure and total pressure equilibriums were calculated. The results for each model are presented in the tables below:

Table 14: Mass flow rate, Static and Total pressure equilibriums at the boundaries - Big Model

Big Model				
k-ε Realizable - Standard Wall Functions				
Speed	**Boundary**	**Mass Flow Rate (kg/s)**	**Static Pressure (Pa)**	**Total Pressure (Pa)**
8.7	Inlet	3.73	10.82	57.11
	Outlet	3.73	0	47.23
10.2	Inlet	4.37	14.8	78.43
	Outlet	4.37	0	64.93
11.7	Inlet	5.02	19.26	102.99
	Outlet	5.02	0	85.4
13.8	Inlet	5.92	26.76	143.24
	Outlet	5.92	0	118.86
15.2	Inlet	6.52	32.14	173.47
	Outlet	6.52	0	144.11
k-ω SST				
8.7	Inlet	3.73	10.56	56.86
	Outlet	3.73	0	47.12
10.2	Inlet	4.37	14.32	77.96
	Outlet	4.37	0	64.73
11.7	Inlet	5.02	18.63	102.35
	Outlet	5.02	0	85.15
13.8	Inlet	5.92	25.31	141.8
	Outlet	5.92	0	118.34
15.2	Inlet	6.52	30.7	172.01
	Outlet	6.52	0	143.55

Table 15: Mass flow rate, Static and Total pressure equilibriums at the boundaries - 3D Printed Model

3D Printed Model				
k-ε Realizable - Standard Wall Functions				
Speed	**Boundary**	**Mass Flow Rate (kg/s)**	**Static Pressure (Pa)**	**Total Pressure (Pa)**
8.9	Inlet	3.81	3.87	52.31
	Outlet	3.81	0	48.61
10.5	Inlet	4.5	5.23	72.66
	Outlet	4.5	0	67.65
12	Inlet	5.14	6.67	94.74
	Outlet	5.14	0	88.36
14.5	Inlet	6.22	9.42	138.02
	Outlet	6.22	0	128.99
15.7	Inlet	6.73	10.88	161.65
	Outlet	6.73	0	151.22
k-ω SST				
8.9	Inlet	3.81	3.85	52.29
	Outlet	3.81	0	48.63
10.5	Inlet	4.5	5.16	72.58
	Outlet	4.5	0	67.67
12	Inlet	5.14	6.51	94.58
	Outlet	5.14	0	88.38
14.5	Inlet	6.22	9.18	137.77
	Outlet	6.22	0	129.02
15.7	Inlet	6.73	10.54	161.3
	Outlet	6.73	0	151.25

Looking at the tables above it is understood that the conservation of mass is satisfied in every case and the total pressure is also reduced across the control volume due to the friction losses that occur at the wind tunnel's walls and because of the air-model interaction. All the static and total pressure values above are given in relation to the operating pressure of the simulations which is the atmospheric pressure which is equal to 103.225 (Pa).

The pressure drop measurements were also taken in the wind tunnel with and without the presence of Big Model. The measurements were taken for a relevant range of wind tunnel speeds in comparison to results presented above. The pressure drop measurements in wind tunnel are presented below.

Table 16: Wind tunnel - Test Section's Inlet and Outlet pressure drop measurements

Wind Tunnel Speed (Hz)	Free Stream Velocity (m/s)	DP with Big Model (Pa)	Dp empty wind tunnel (Pa)
10	3	2	0.0
20	6	6.5	2.0
30	9	14	4.0
40	12	25	7.0
50	15	38	11.0

The results from Table 16 are compared to the CFD inlet and outlet pressure drops, even though there is a slight difference in the free stream's velocity range in order to investigate their relationship.

Pressure Drops Comparison

$y = 0.256x^{1.8358}$

$y = 0.1581x^{1.9536}$

$y = 0.9x - 3.3$

$y = 0.0397x^2 + 0.1857x - 0.8$

Legend:
- Big model (exp)
- Big Model (CFD)
- Wind Tunnel (exp)
- Power (Big model (exp))
- Power (Big Model (CFD))
- Linear (Wind Tunnel (exp))
- Poly. (Wind Tunnel (exp))
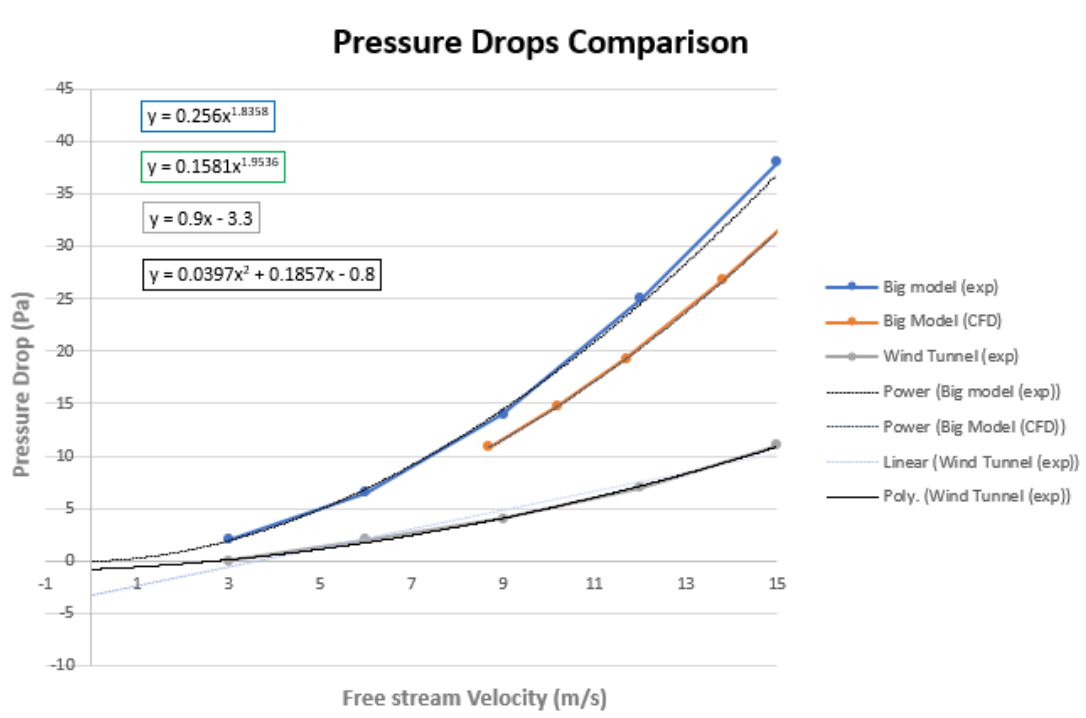
Figure 103: Pressure Drops Comparison, Wind Tunnel (With and without the Big Model) vs CFD with the Big Model

From Figure 103 it is understood that the CFD and the wind tunnel pressure drop measurements have a very good agreement since both are second order equations with respect to the free stream velocity, but also their values are close. The fact that the CFD line is below the wind tunnel's line is a matter of the free stream velocities difference. Finally, the line representing the pressure drop in the wind tunnel can be approximated linearly since the pressure drop for the different free stream velocities is much smaller due to the fact the flow is no longer affected by the Big Model's blockage.

3.14 First Layer Height Dependency Check

Bearing in mind the boundary layer theory and the fact that the layer's thickness changes with the variation of air velocity it was necessary to calculate the first layer height for all the free stream velocities for both models and investigate how it affects the solution. All the information about the f.l.h. can be obtained by the following tables:

Table 17: "Big Model" first layer height with respect to the target y+ and the free stream velocity

Big Model		
Free Stream Velocity (m/s)	y+ = 30 f.l.h. (mm)	y+ = 1 f.l.h. (mm)
8.7	1.10	0.038
10.2	0.99	0.033
11.7	0.87	0.029
13.8	0.75	0.025
15.2	0.69	0.023

Table 18: 3D Printed Model first layer height dependency with respect to the target y+ and the free stream variance.

3D Printed Model		
Free Stream Velocity (m/s)	y+ = 30 f.l.h. (mm)	y+ = 1 f.l.h. (mm)
8.9	1.00	0.033
10.5	0.86	0.029
12	0.76	0.025
14.5	0.64	0.021
15.7	0.60	0.020

Considering the f.l.h. calculation method and tables above, it is obvious that the f.l.h. value is proportional to the y+ and inversely proportional to the free stream velocity. This is the reason why the f.l.h. values that correspond to y+=1, are one order of magnitude lower than those corresponding to y+=30. The f.l.h. values corresponding to y+=30 are going to be used with the k-ε model and those corresponding to y+=1 with the k-ω model. Choosing a y+ value below 5 brings the first layer height very close to the wall and for this type of problems, the k-ω SST model gives a better prediction for the separation due to the viscosity limiter. The viscosity limiter limits the viscosity when the f.l.h. is close to the wall, where the shear is high. That means that the wall shear stress is going to reduce faster, so it is more likely to get separation. This explains why the k-ω SST model is expected to perform better than the k-ε Realizable

model with Standard wall functions, in areas close to the wall, where the k-ε over predicts the wall shear stress.

In order to check the how the solution is affected by the changing f.l.h. the following simulations were performed and compared:

1. Simulation of the "Big-Model", using the k-ε Realizable model with Standard wall functions, with a different f.l.h. value depending on the free stream velocity.
2. Simulation of the "Big-Model", using the k-ε Realizable model with Standard wall functions, with the same f.l.h. value (f.l.h.=0.69) for all the different free stream velocities.
3. Simulation of the "Big-Model", using the k-ω SST model with a different f.l.h. value depending on the free stream velocity.
4. Simulation of the "Big-Model", using the k-ω SST model with the same (f.l.h.=0.69) for all the different free stream velocities.

After collecting the data from the simulations, the following results were obtained:

Figure 104: k-ε model simulations comparison
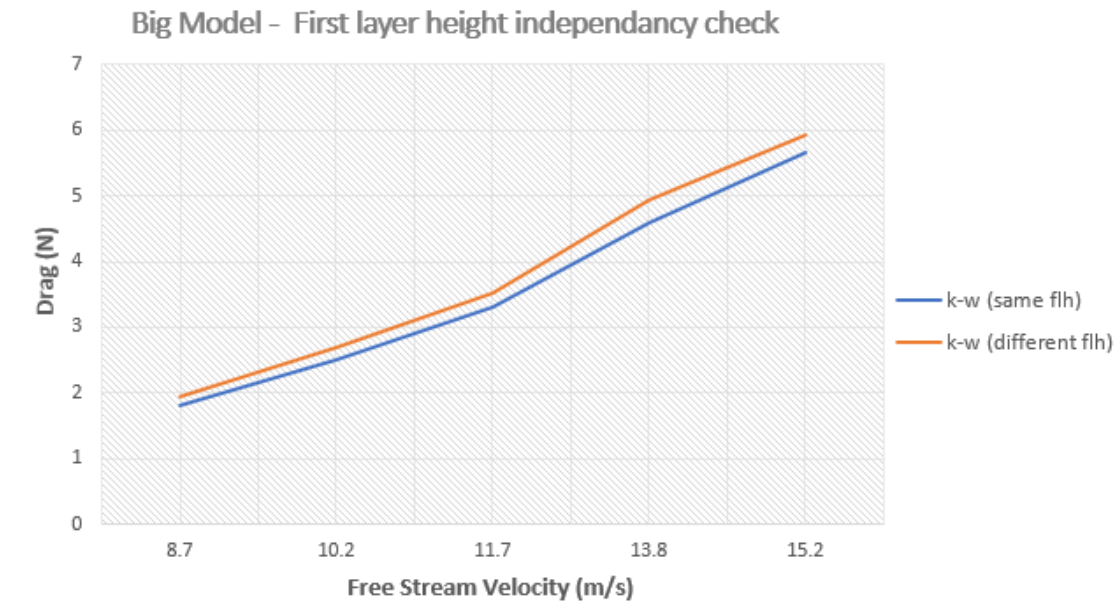
Figure 105: k-ω SST model simulations comparison

As it is understood in the case of the k-ε model using different values for the first layer height made no difference in the actual result of the drag values and there was no difference in the convergence time also. In the case of k-ω SST simulations comparison there is a slight difference between them but still the f.l.h. did not seem to affect the results.

3.15 Formula 3 Model Simulation

Remembering that the aim of the study was to validate the CFD tools that can be used for the investigation of full-scale Formula type cars, the next step after all the previous studies was to create a 33% scale up model of the Big Model. The size of this model was very close to that of a Formula 3 or FSAE car, so the Formula 3 name was chosen, so that no confusion was created with the studies of Centaurus Racing Team's 5th racecar that follow.

The model was tested for the same free stream velocities as the "Big Model" and the purpose was to compare the drag scaling factor between these two and the scaling factor that was produced by the comparison between the Big Model" and the 3D Printed Model. With the term drag scaling factor the average number with which the drag values of the "Big Model" need to be multiplied in order to give the drag values of the F3 model.

In the following figure and table, the results from the simulations of the Formula 3 model are presented. All the simulations were conducted using the k-ε Realizable model with Standard wall functions, y+ = 30 and the same f.l.h.:
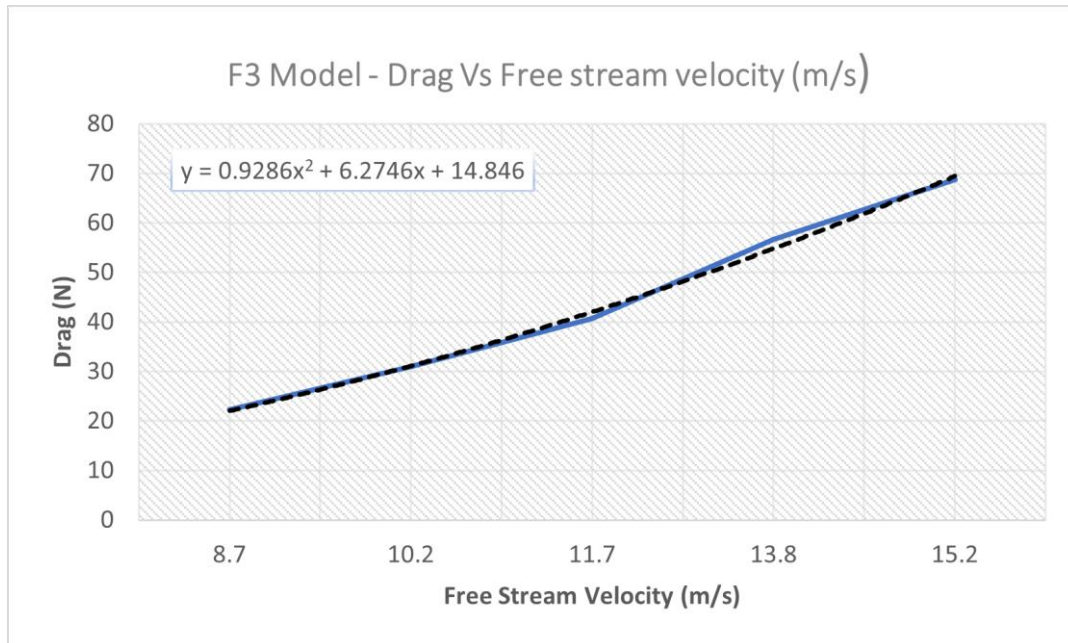
Figure 106: F3 Model – Drag vs Free stream velocity plot

From Figure 106 it is proved that the drag equation is of second order with respect to the free stream velocity. More information concerning the actual drag values that correspond to each one of the free stream velocities of interest can be drawn from table 15.

Table 19: F3 Model Simulation Results

F3 Model Simulation Results	
Free Stream Velocity (m/s)	CFD Drag (N)
	F3 Model
8.7	22.32
10.2	31.00
11.7	40.73
13.8	56.64
15.2	68.73

An analytical comparison between drag scaling factors of the F3 Model, the Big Model and the 3D Printed Model is presented at the CFD Results section.

3.16 Solution Residuals Monitor

Defining convergence by looking at the residuals values is only a small part of ensuring that we have a valid solution. For a steady state simulation, the engineer needs to ensure that the solution's residual values have reduced to an acceptable value typically 10^{-4} or 10^{-5}, in order to reinforce his argument that the solution has converged.
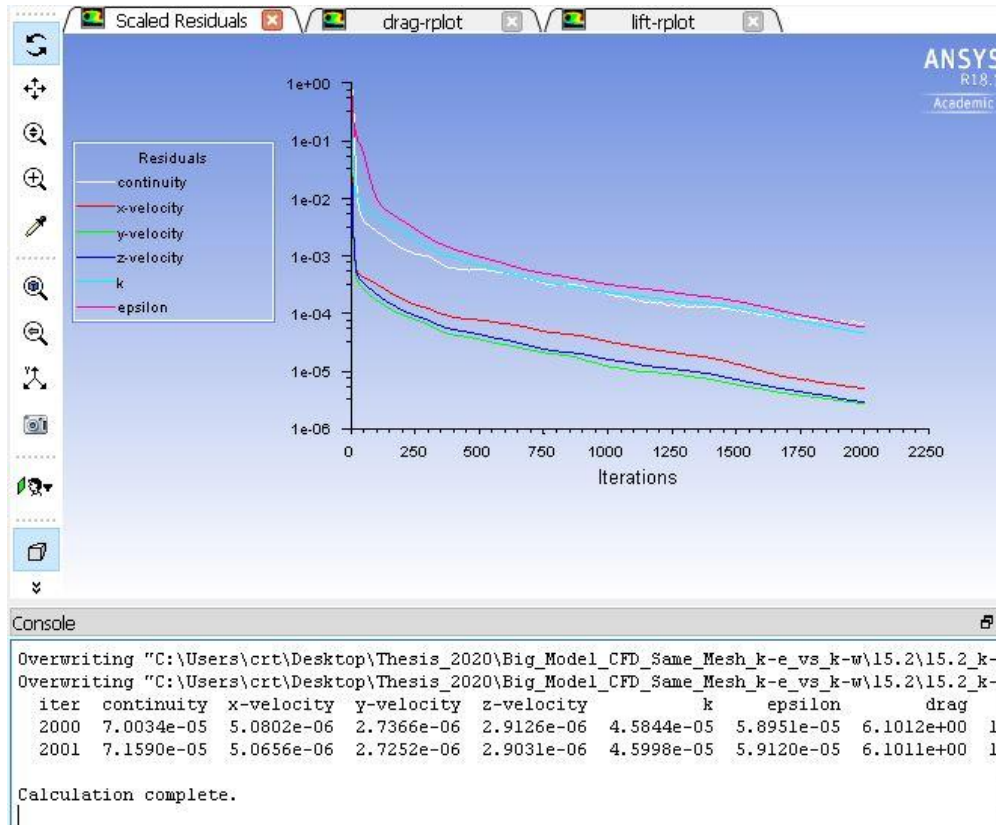
Figure 107: Residuals monitors

The residuals plot presented above confirms that the residuals have reached the desirable error order. This is also confirmed by the residual plot presented by [Simon, 2016] in his Master Thesis, p.92, Figure 18, where he shows that the residuals of the governing equations have levelled out below 1 % but emphasizes on the fact that the residuals are only a first indication of the accuracy of the simulation.

3.17 Special Case Studies

The reason why two extra cases, outside the frame of this study, are going to be analyzed is the fact that the purpose of this study was to validate some CFD tools, which could be used for the development of the aerodynamics of a race car. The same type of meshes and turbulence models that were studied before were used by the aerodynamics department in Centaurus Racing for academic research. The difference is that the package is 100% developed through CFD. This is done due to limited resources, because even if a scale model of the actual race car was constructed, so that the students were able to implement different 3D printed designs on it and compare their measurements to the CFD results, that would still raise the cost due to the 3D printing but also because the necessary equipment doesn't exist in order to measure the downforce. Moreover, it was important to show how much more information can be drawn from the CFD post processing in contradiction with a wind tunnel experiment in order to compare designs.

3.17.1 FSAE car travelling at a straight with constant speed

Most of the CFD simulations for the development of the aerodynamic package are done at a flat ride height while the car is travelling through a straight with constant speed. This is the easiest way to compare designs, but it might not be the most effective considering that during the endurance and the autocross event the time that the car spends on the straight is relatively small considering the number of turns of the track.

Figure 108: Formula Student Germany 2012 – Autocross Track

The most effective way to compare designs is by choosing different yaw, pitch and roll angles and simulate all the designs for each condition. The goal is to choose the design that gives the best performance in the previously mentioned conditions, simultaneously. This will help the

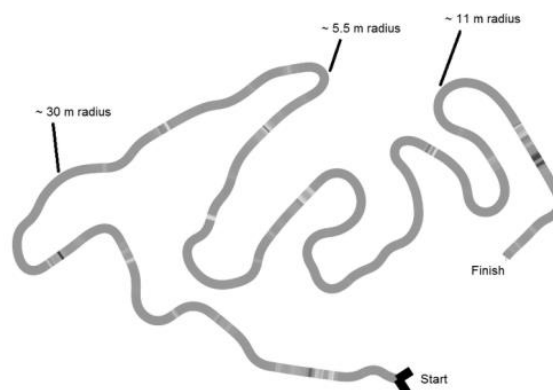teams find the right aerodynamic balance at the corner entry and exit. This type of comparison takes time not only because of the number of simulations but also because of the post processing that has to be performed, so the most time effective way of comparing, especially for newly created aerodynamic department of students is in straight-line.

Straight-line CFD computational time can be further minimized by simulating the model in symmetry and reducing the mesh size by 50%. This approach required one more boundary condition which is described as symmetry plane boundary condition. This condition implies that the component of the gradient normal to the boundary should be fixed to zero. The components parallel to it are projected to the boundary face from the inside of the domain [Jasak, 1996].

Such a case will be presented in the results section were a representation of the post processing areas of interest is going to be shown.

3.17.2 FSAE car travelling through a corner

The main goal of this study is the investigation of an FSAE type car's behavior and it's interaction with the air, while travelling through the corner of the skid pad track, which is one of the dynamic events of the FSAE competition.

Traditionally a turning car is modeled as having a yaw angle with respect to the direction of heading [Katz,1995]. If the curved path assumed through the corner has a small degree of curvature compared to the vehicle slip angle, one might argue that this approach should give a fair approximation of the case of a turning car.

The reason why this situation was investigated, is the fact that our simulations are steady state, and the skid pad event is a steady cornering condition. Through this simulation our team would be able to understand how much side force is produced and the aero balance is changing in comparison to the car's body slip. The variation of the car's aero-balance data would then be imported to the yaw moment diagram code, which is used by the suspension department in order to see if the lateral acceleration is increased. Knowing the aero performance through a corner could help us do targeted changes to our designs in order to optimize the airflow management.

3.17.2.1 Problem Breakdown:

Before proceeding with the research and the construction of the physical model, it is important to define the problem's constants and variables. The simulation was going to be a steady state condition with Amphion traveling through a corner, which would have the same radius (9.181m) with the Skid Pad event's track layout, with a steering angle of 15 degrees, roll angle of 1 degree and with a translational velocity of 13 m/s:

Problem Variables:

> ➢ Body slip (Vehicle Slip Angle/ Yaw angle at the center of the car)

Problem Constants:

> ➢ Corner Radius
> ➢ Steering Angle
> ➢ Roll Angle
> ➢ Air Angular Velocity
> ➢ Car's Translational Velocity

Geometry Changes: For each different cornering case the car was rotated around the body center axis, for a given body slip angle. After the end of the simulation a check of the C.O.P. and the C_l, C_s and C_d values was performed.

3.17.2.2 Research Assumptions:

Vehicle slip angle is necessary for the turning of a front steer car and can be defined as the angle between the direction that a vehicle is heading, and the direction of its instantaneous velocity. This angle will then be responsible for a yaw angle, the angle with which air hits the car, with respect to its longitudinal center line. In general, a yaw angle can be introduced by both side winds and gusts. In this case it was assumed that the free stream velocity of the air with respect to the car, is only induced by the vehicles' velocity itself, so that the yaw angle is equal to the vehicle slip angle. The angle between the car longitudinal axis, and the direction of the instantaneous velocity, induced by the vehicles' velocity itself, so that the yaw angle is equal to the vehicle slip angle. The above definition of the slip angle is shown in Figure 109 where it is called "slip angle at the center of the car".
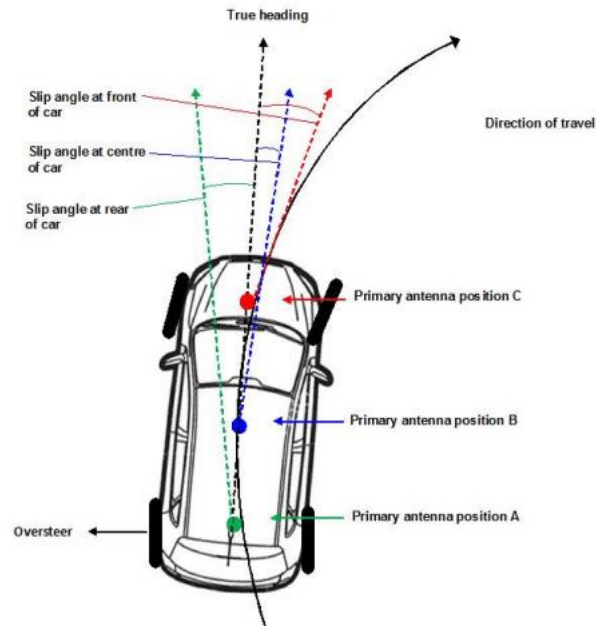
Figure 109: Representation of the vehicle's slip angle

3.17.2.3 Simulation setup development:

At first, several numerical simulations were done in order to find the right steady state cornering flow's boundary conditions, so that an "ill conditioned" problem would be avoided. In order to save time a simplified geometry was chosen.

Obviously, the geometry consisted of the nosecone, the front wheels, a simplified version of the suspension and a circular tunnel. The car's distance from the tunnel's center was equal to 9.181m. The side walls had to have enough clearance from the car so that they did not affect the flow around the car. The distance of the side walls was 1.5 times the car's length. The theory for the straight condition, says that the side wall's distance from the simulated geometry should be equal to the geometry's length, so we chose 1.5 times that length, to avoid blockage effect. Despite the previous comment, in cases where the data from the CFD are compared to data drawn from the wind tunnel the control volume should have the same size as the wind tunnel's test section, so keeping a clearance equaling 1.5 time the vehicle's length from the side wall, cannot always be applied, so blockage will also affect the CFD results. In Figure 110 and Figure 111 the geometry properties of the control volume and the test model are presented respectively.
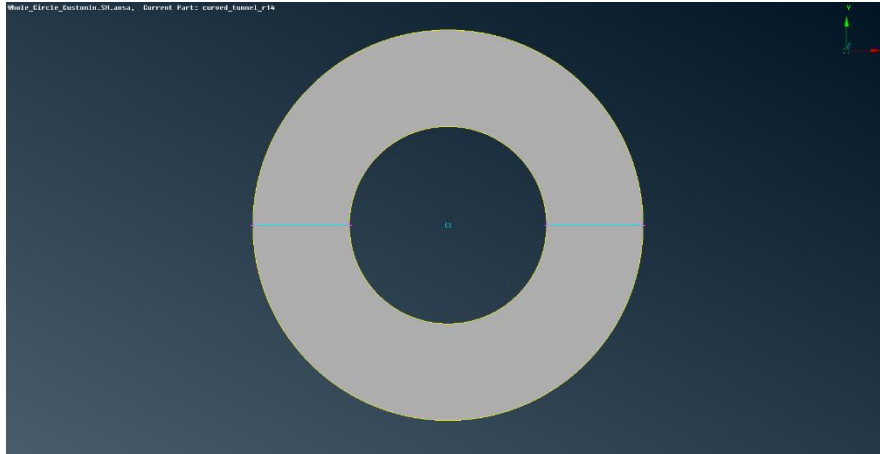
Figure 110: Cornering model's control volume for the first experiment
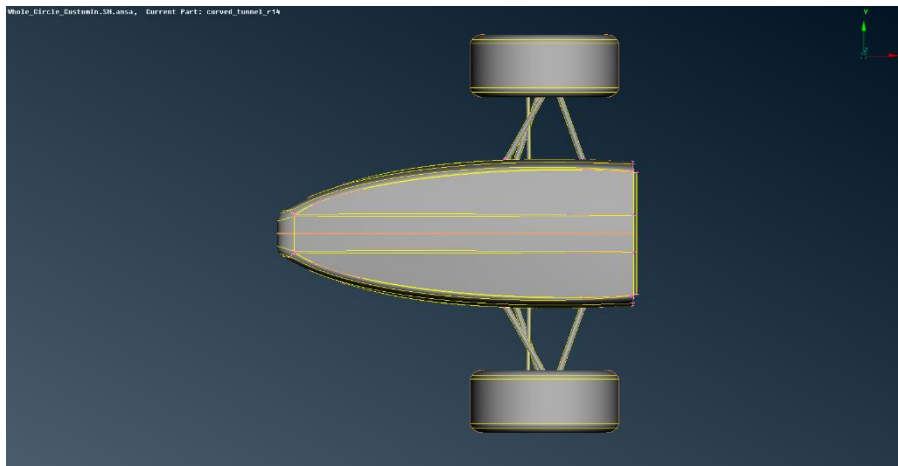
Figure 111: Amphion's simplified geometry – Top View

The position of Amphion's simplified geometry in the control volume can be seen in Figure 114.

3.17.2.4 Boundary conditions determination:

During a straight tunnel CFD, the vehicle is steady, except of its wheels and the road below it, while the air is moving towards it. The same thing happens here, but with a small difference. The difference is that the air should have a rotational velocity which would result in a vehicle's translational velocity equal to 13 (m/s), because this is the maximum speed that this car could achieve during the skidpad event. After dividing the translational velocity with the corner radius, the air's angular velocity (1.434 rad/sec) was calculated. The next step was to find the way in which this boundary condition was going to be applied to the air inside the control volume. For this reason, Fluent's guide was studied in order to see how the Moving Reference Frame works. In this case a Single Reference Frame was applied because there is only one frame rotating around a specified axis. The second thing that had to be changed was the way in

which the stationary walls in the physical model, were defined. Fluent's guide suggests that in order to set a wall as stationary in the absolute frame, the user should set it as a moving wall whose angular velocity in reference to axis, around which our fluid rotates, is 0 rad/sec. Finally, another important change in the setup was the velocity formulation. Since the all the fluid in the control volume is rotating, then a change in the velocity formulation, from absolute (default setting) to relative, should be applied. This setup change changes the velocity components in the momentum equations and instead of using absolute velocities it uses relative velocity components.

After applying those changes to the setup, the first simulation was ready to be run. The initialization method that was chosen, was the hybrid since no inlets or outlets existed. After 2000 iterations and since no problems were indicated by the solver the simulation was stopped. In the post processing a serious problem was detected which affected the pressure and velocity field around the geometry, significantly. After checking the streamlines path by increasing their pseudo-time duration it was realized that the nosecone's streamlines, after completing a circle around the tunnel, started gathering above the car.

This problem indicated that a change to the tunnel's geometry should be done. An inlet and outlet should be introduced, so that the car's wake did not affect the flow in front of it. Moreover, the inlet and outlet introduction meant that the right boundary conditions had to be set, so that initialization errors, which could affect the quality of the results, were eliminated.

The tunnel's geometry changed in the following way:
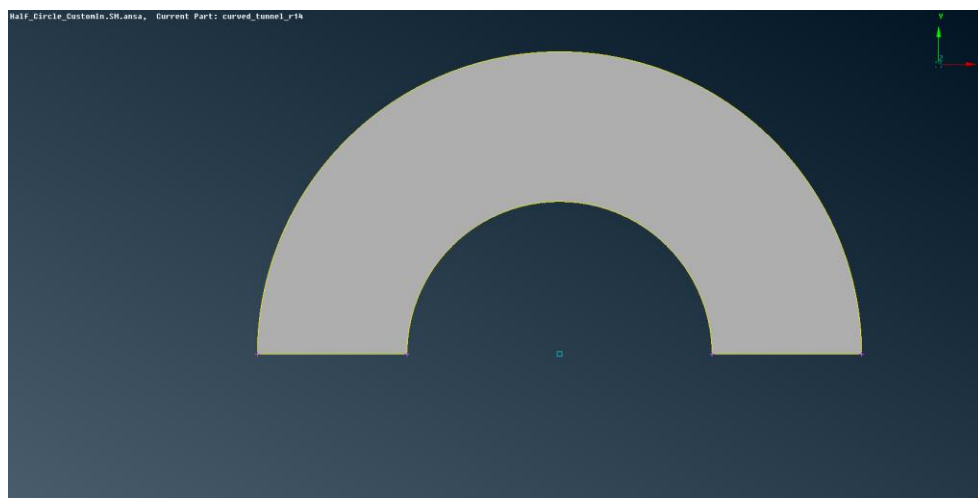
Figure 112: Half circle control volume

3.17.2.5 Reversed flow and fluid rotation problems:

At that point, a big challenge was faced concerning the boundary conditions. At the beginning, the simulation was initialized, using the standard method, while keeping the default values for the turbulent kinetic energy and the dissipation rate. After starting the simulation, the monitor indicated reversed flow problems which were followed by hugely oscillating residuals, so there was no doubt that the results were going to be misleading. The post-processing showed that the fluid was not rotating in a proper way and the fluid's velocity vectors at the pressure outlet had the following form:
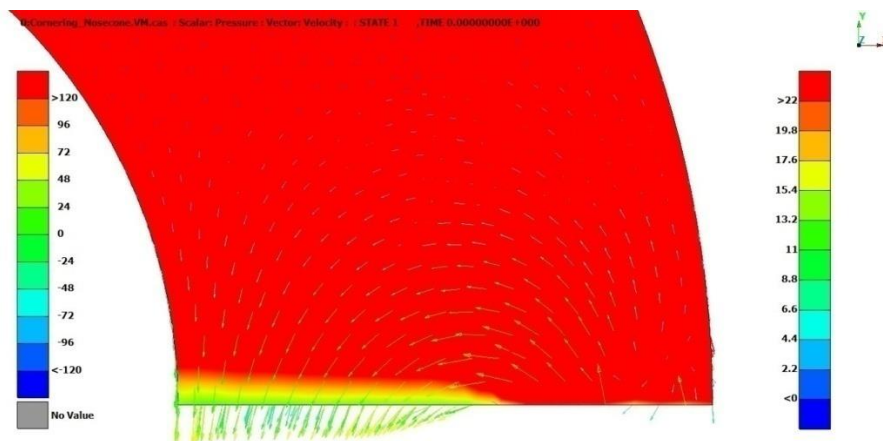
Figure 113: Reversed flow problems at the outlet

In order to overcome the problem with the fluid's rotation, the initialization method was changed. The inlet's condition could not be accurately predicted, so the standard initialization was not going to give the linear velocity profile that was expected, instead it was creating a large error. From that point on the fluid started rotating properly but the reversed flow problems still existed. As the solution proceeded the reversed flow problem still existed.

3.17.2.6 Inlet and outlet planes generation for data interpolation:

In order to overcome the reversed flow problem, the idea was to introduce a custom inlet and outlet inside a circle tunnel and rotate the air inside so that a better and more linear velocity and pressure profile was achieved at the boundaries.
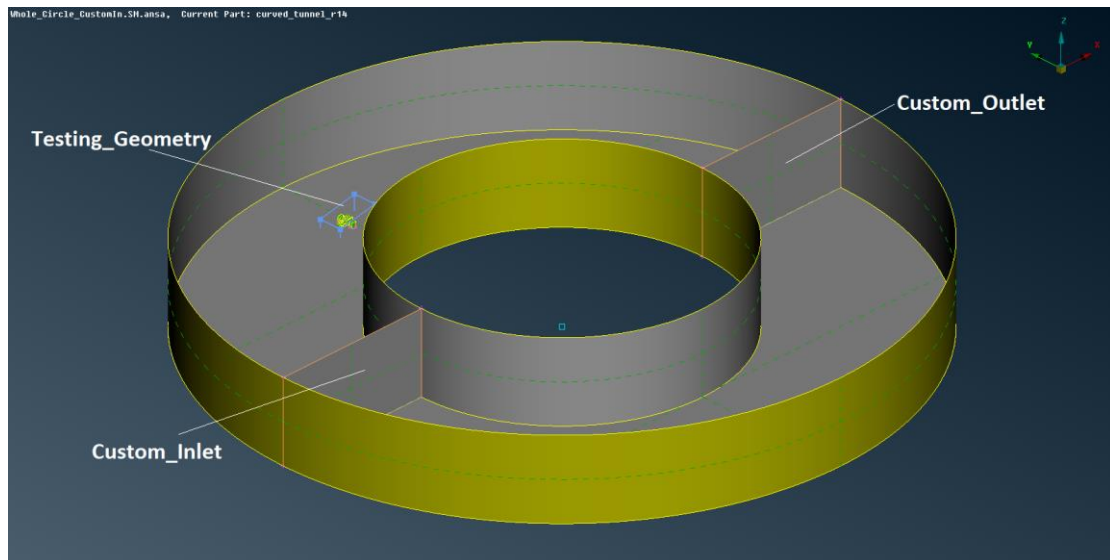
Figure 114: "Custom" inlet and outlet planes creation

In order to keep the custom outlet's pressure and velocity fields completely unaffected we decided not to use any geometry inside the tunnel, so imagine Figure 114 without the simplified geometry. After conducting 2000 iterations the following information was extracted, for the respective planes:

- Axial Velocity
- Tangential Velocity
- Radial Velocity
- Turbulent Kinetic Energy
- Turbulent Dissipation Rate

These values were interpolated to the inlet and the outlet of the previous simulation. The simulation was initialized again by the hybrid method. At the first 40 iterations the monitor was indicating again the reversed flow problem but only to a few faces of the discretized boundary, but afterwards the problem resolved. After 3500 iterations the lift and drag values started to converge. Then the flow field was investigated through post processing to check for any unphysical phenomena.

The post processing did not show anything unexpected so that suggested that this setup was working, and the next step was to introduce the whole car's geometry inside the control volume.

3.17.2.7 Control volume's dimension determination:

For the simulation of the whole car the same setup was used with the only difference being that there were 40 more stationary walls and thus 40 more boundary conditions. Another change in the boundary conditions was the rotation of the front wheels. Since the car has 15 degrees steering angle the wheels are rotating around two different axes whose direction can be defined by the vectors that pass through the centers of the front rims. The simulation run smoothly, but during the post processing a disturbance in outlet's velocity magnitude was detected:
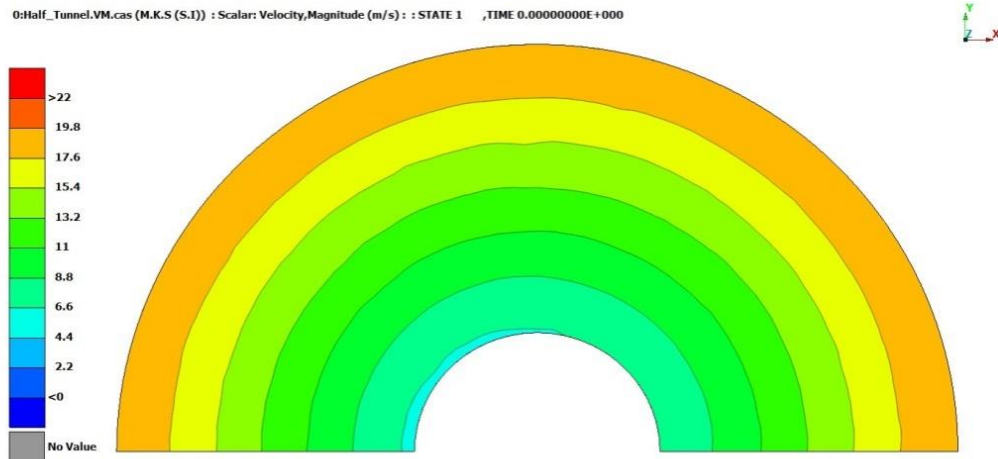
Figure 115: Velocity Magnitude of half circle control volume
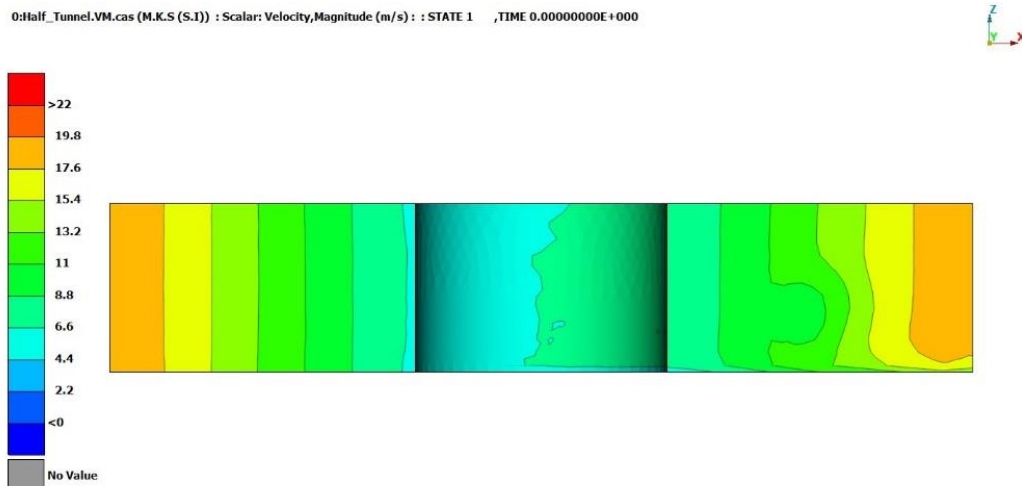
Figure 116: Boundary Velocity Profile Distribution - Left Inlet - Right Outlet

From Figure 116 it is seen that the outlet's velocity magnitude is not as linear as the inlet. The flow has not reached free stream conditions since the outlet is affected by the car's wake and that could affect the aerodynamic efficiency of the car itself. This is a common problem in cases where the outlet is not far away from the simulated geometry. So further changes in the control volume were done, by extending the outlet to 270 degrees. After the end of the simulation, the velocity distribution at the tunnel and the outlet was the following:
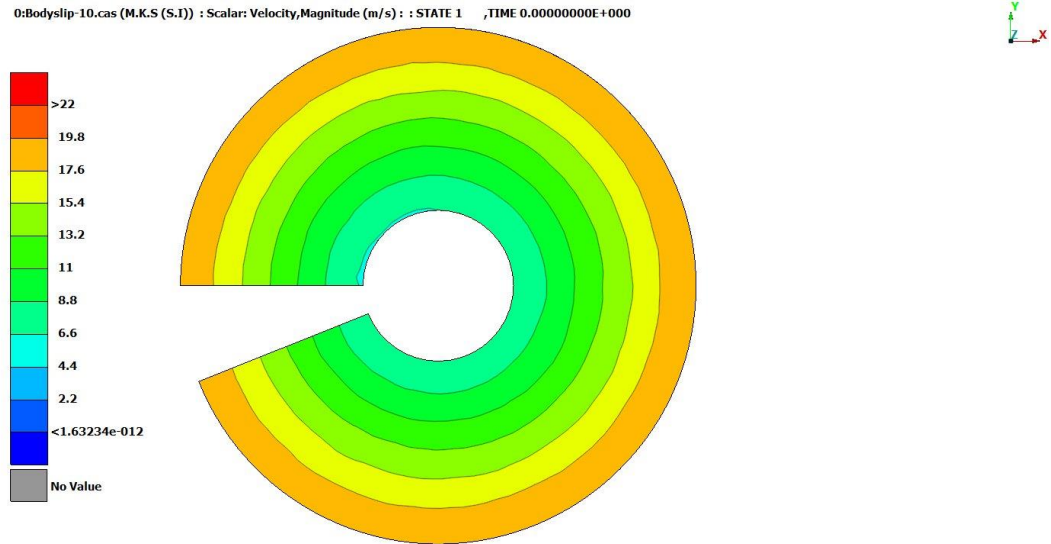
Figure 117: 270-degree control volume – velocity magnitude

Figure 118: 270-degree control volume – outlet's velocity magnitude

The outlet's velocity distribution is still not as linear as the inlet's but obviously the distribution is better in comparison to the 180-degree tunnel. Moreover, a disturbance due to the boundary layer development on the road is detected, which also needs further investigation.

3.17.2.8 Cornering simulations

All the simulations were performed using the 270-degree control volume. Five simulations were performed and the only changing variable was the car's body slip. At this point it would be important to mention that, since Amphion's aero package was developed through simulations of the car in a straight tunnel, these simulations were not used for the comparison of the different designs. They were done for the development of $C_l \cdot A$ vs $C_d \cdot A$ vs Centre of Pressure 3D Map and a C.O.P. vs Body slip plot. These data would be integrated in the lap time simulator to see how the vehicle's lap time is affected both at the skid pad and the endurance event. Designing an aerodynamic package based on cornering simulations would be ideal but even though it needs a lot of experience, it also needs a lot of computational power. In Figure 119 a representation of the control volume is done, while in Figure 120 the steering angle and the roll angle of the car (15 degrees and 1 degree respectively) are shown. These angles are kept constant while the car is travelling through the left circle of the Skid Pad.
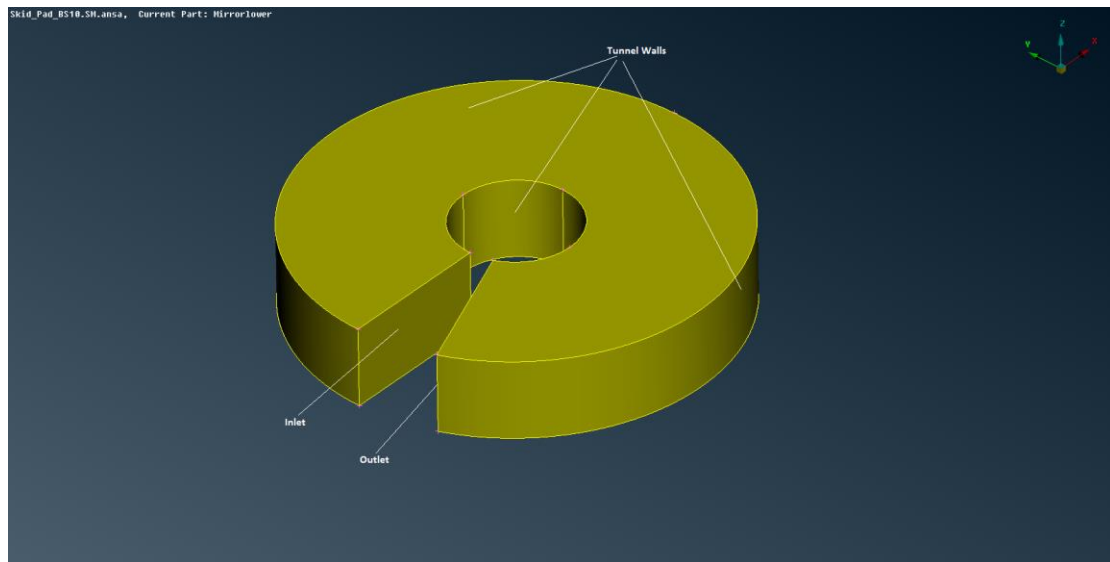
Figure 119: Cornering model control volume
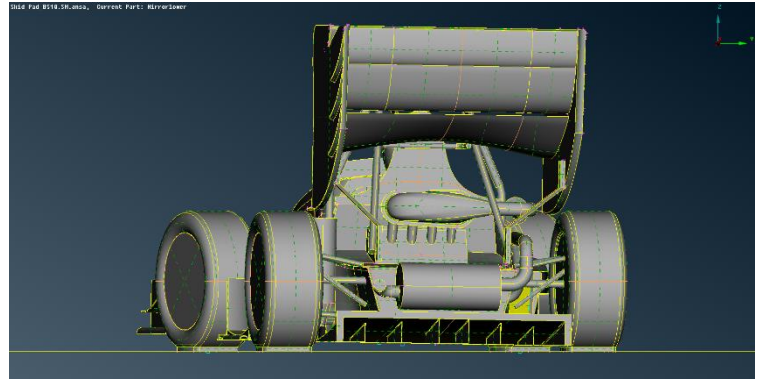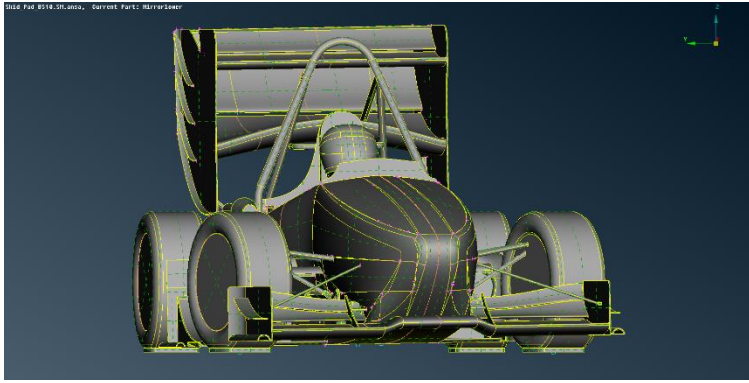
Figure 120: Amphion positioned in the control volume

The five simulations correspond to 5 different body slip angles: -10, -5, 0, 5, 10, with the negative values indicating and understeering behavior and the positive values, an oversteering behavior. The change is understood from Figure 121:

0 degrees
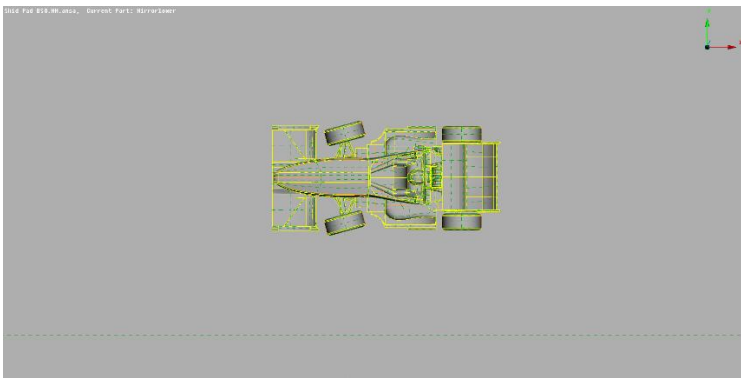
5 degrees
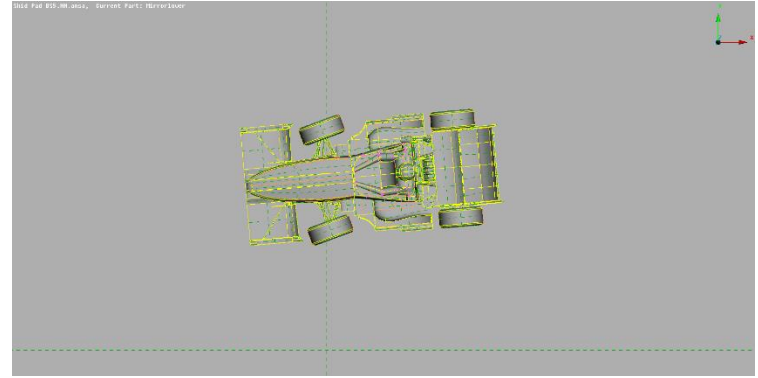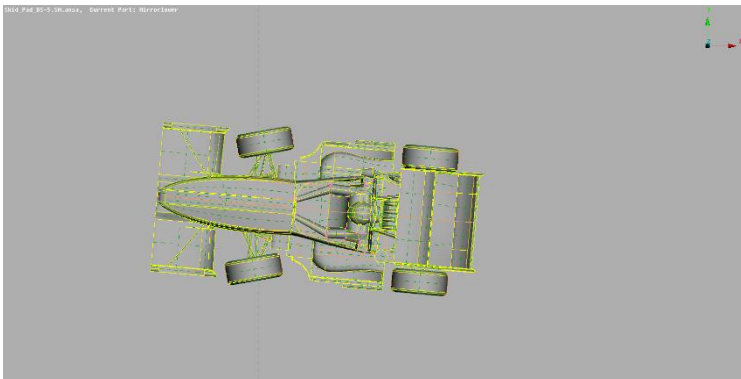
-5 degrees
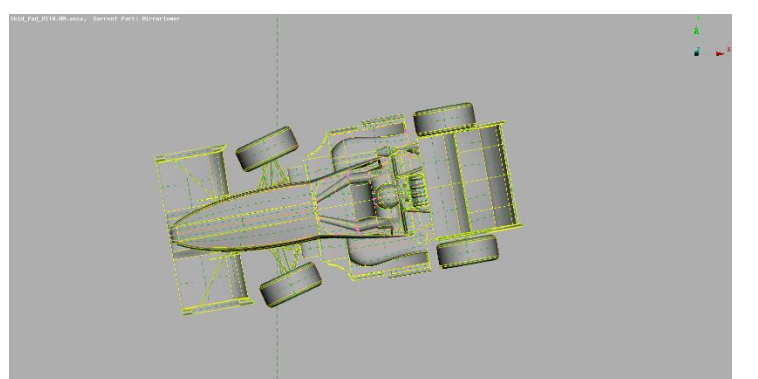
10 degrees
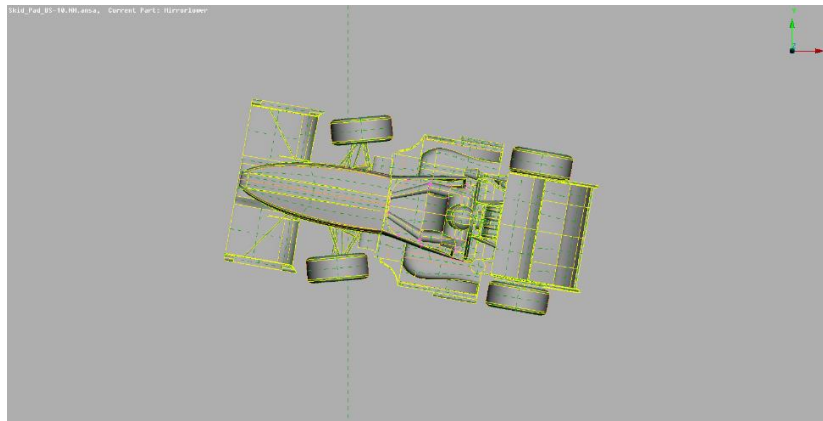
Figure 121: Body slip Variations

Finally, the mesh used for the CFD was the finest mesh that has been presented up until now. This happens because the geometry is much more complex, and the car is simulated as a whole, since no symmetrical model can be developed for this case. Also, the control volume is larger. From Figure 122 and Table 20: Cornering model mesh properties, information about the size of the surface and the volume mesh is given:
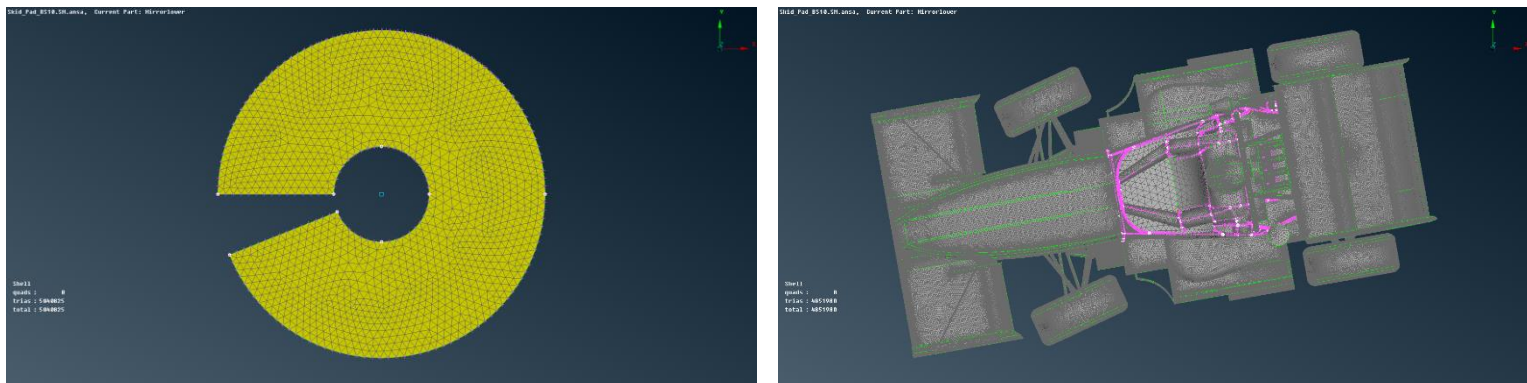
Figure 122: Cornering model control volume and car surface mesh

Table 20: Cornering model mesh properties

Scenario	Type of Elements/Cells	Number of Elements
Surface Mesh	Trias	5.040.825
Volume Mesh	Tetras	85.455.622

To understand the computational cost for the solving an 85 million cells mesh, a hyper computer allocating 28 cores needed 15 hours for the solution to converge, after 4800 iterations.

The results of the five simulations will be shown together with some post processing images in **4.4.2.2**.

3.18 Case Setup Checks

In this section a summary of all the necessary steps for the setup of the k-ε and the k-ω simulations will be given. The manuals presented below can help the user check whether he has done all the steps for the simulation setup of a racecar which is travelling at a straight with constant speed.

Table 21: Simulation setup for non-moving road and tire's, using the k-ε Realizable model.

FLUENT SETUP CHECKS		
STEPS	COMMANDS	SELECTION
1	General-Mesh	Check
2	General-Mesh	Improve
3	General-Solver Type	Pressure-Based
4	General-Velocity Formulation	Absolute
5	General-Time	Steady
6	Models-Viscous	k-e Realizable Standard Wall Functions (y+=30)
7	Boundary Conditions-Inlet	Velocity Inlet - Speed - Specification Method (k-ε)
8	Boundary Conditions-Outlet	Pressure Outlet - Specification Method (k-ε)
9	Operating Conditions	Operating Pressure=101325 Pa
10	Solution Methods-Scheme	SIMPLE
11	Solution Methods-Discretization-Gradient	Green Gauss Node Based
12	Solution Methods-Discretization-Pressure	Standard
13	Solution Methods-Discretization-Momentum	Second Order Upwind
14	Solution Methods-Discretization-Turbulent	Second Order Upwind
15	Solution Methods-Discretization-Turbulent	Second Order Upwind
16	Solution Controls-Pressure	0.3
17	Solution Controls-Density	1
18	Solution Controls-Body Forces	1
19	Solution Controls-Momentum	0.4
20	Solution Controls-Turbulent Kinetic Energy	0.5
21	Solution Controls-Turbulent Dissipation Rate	0.5
22	Solution Controls-Turbulent Viscosity Ratio	0.7
23	Solution Controls-Limits-Turbulent Viscosity	10^9
24	Monitors-Residuals-Continuity	10^(-6)
25	Solution Initialization	Standard-Absolute-From Inlet
26	Calculation Activities-Autosave	Iterations=400 - Only the Latest
27	Run Calculation	Check Case

Table 22: Simulation setup for non-moving road and tire's, using the k-ω SST model.

FLUENT SETUP CHECKS		
STEPS	**COMMANDS**	**SELECTION**
1	General-Mesh	Check
2	General-Mesh	Improve
3	General-Solver Type	Pressure-Based
4	General-Velocity Formulation	Absolute
5	General-Time	Steady
6	Models-Viscous	k-ω SST (y+=30) / (y+=30)
7	Boundary Conditions-Inlet	Velocity Inlet - Speed - Specification Method (k-ω)
8	Boundary Conditions-Outlet	Pressure Outlet - Specification Method (k-ω)
9	Operating Conditions	Operating Pressure=101325 Pa
10	Solution Methods-Scheme	SIMPLE
11	Solution Methods-Discretization-Gradient	Green Gauss Node Based
12	Solution Methods-Discretization-Pressure	Standard
13	Solution Methods-Discretization-Momentum	Second Order Upwind
14	Solution Methods-Discretization-Turbulent	Second Order Upwind
15	Solution Methods-Discretization-Turbulent	Second Order Upwind
16	Solution Controls-Pressure	0.3
17	Solution Controls-Density	1
18	Solution Controls-Body Forces	1
19	Solution Controls-Momentum	0.4
20	Solution Controls-Turbulent Kinetic Energy	0.5
21	Solution Controls-Turbulent Dissipation Rate	0.5
22	Solution Controls-Turbulent Viscosity Ratio	0.7
23	Solution Controls-Limits-Turbulent Viscosity	10^9
24	Monitors-Residuals-Continuity	10^{-6}
25	Solution Initialization	Standard-Absolute-From Inlet
26	Calculation Activities-Autosave	Iterations=400 - Only the Latest
27	Run Calculation	Check Case

Table 23: Simulation setup for moving road and tire's, using the k-ε Realizable model.

FLUENT SETUP CHECKS		
STEPS	**COMMANDS**	**SELECTION**
1	General-Mesh	Check
2	General-Mesh	Improve
3	General-Solver Type	Pressure-Based
4	General-Velocity Formulation	Absolute
5	General-Time	Steady
6	Models-Viscous	k-e Realizable Standard Wall Functions (y+=30)
7	Boundary Conditions-Inlet	Velocity Inlet - Speed - Specification Method (k-ε)
8	Boundary Conditions-Outlet	Pressure Outlet - Specification Method (k-ε)
9	Boundary Conditions-Road and Tire Patches	Moving Wall - Translational (Absolute)
10	Boundary Conditions-Front Wheels	Moving Wall - Rotational (Absolute)
11	Boundary Conditions-Rear Wheels	Moving Wall - Rotational (Absolute)
12	Operating Conditions	Operating Pressure=101325 Pa
13	Solution Methods-Scheme	SIMPLE
14	Solution Methods-Discretization-Gradient	Green Gauss Node Based
15	Solution Methods-Discretization-Pressure	Standard
16	Solution Methods-Discretization-Momentum	Second Order Upwind
17	Solution Methods-Discretization-Turbulent	Second Order Upwind
18	Solution Methods-Discretization-Turbulent	Second Order Upwind
19	Solution Controls-Pressure	0.3
20	Solution Controls-Density	1
21	Solution Controls-Body Forces	1
22	Solution Controls-Momentum	0.4
23	Solution Controls-Turbulent Kinetic Energy	0.5
24	Solution Controls-Turbulent Dissipation Rate	0.5
25	Solution Controls-Turbulent Viscosity Ratio	0.7
26	Solution Controls-Limits-Turbulent Viscosity	10^9
27	Monitors-Residuals-Continuity	$10^{(-6)}$
28	Solution Initialization	Standard-Absolute-From Inlet
29	Calculation Activities-Autosave	Iterations=400 - Only the Latest
30	Run Calculation	Check Case

4. Results and Discussion

4.1   Experimental Results

In the following section the results of the Drag, the Coefficient of Drag and the Reynolds Number, which were calculated using the raw data drawn from the wind tunnel experiments, are presented:

Table 24: Drag Measurements for the Big Model

WT Values - Big Model			
Speed (m/s)	**Drag (N)**	**C_d**	**Re**
8.6	1.60	0.91	426762
10.2	2.10	0.87	500341
11.7	2.66	0.84	573921
13.8	4.16	0.94	676933
15.2	5.06	0.95	745607

Table 25: Drag Measurements for the 3D Printed Model

WT Values - 3D Printed Model			
Speed (m/s)	**Drag (N)**	**C_d**	**Re**
8.9	0.25	1.25	141744
10.5	0.32	1.15	167226
12.0	0.39	1.07	191116
14.5	0.66	1.25	230932
15.7	0.71	1.14	250043

The drag data are compared in the following plot:
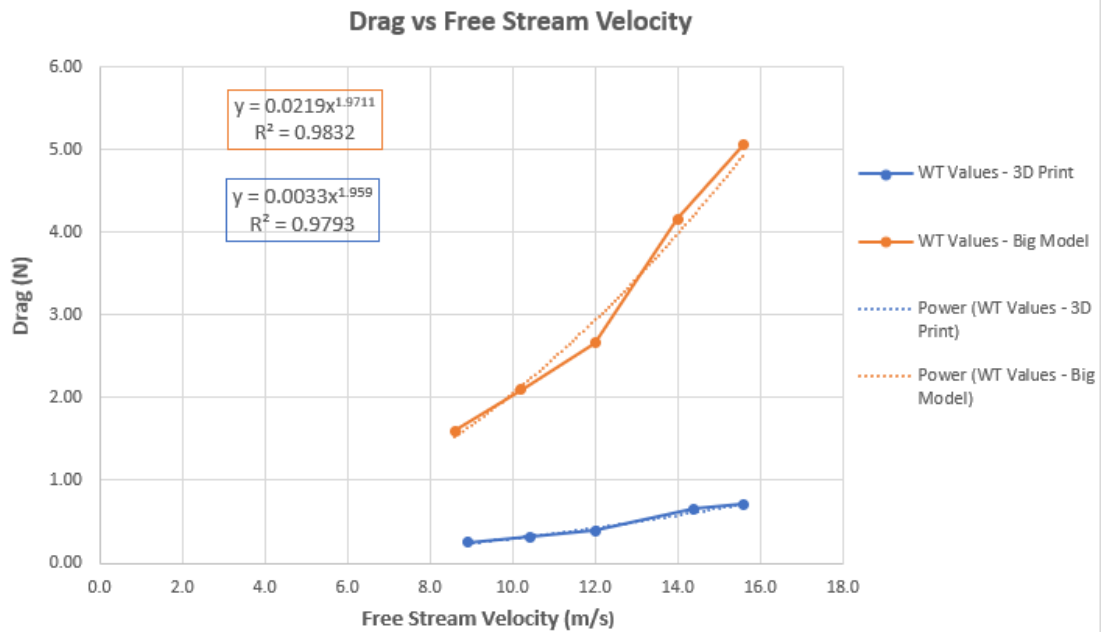
Figure 123: Drag comparison between the Big and the 3D printed model

What is understood is that in both cases the drag equation is a second order equation which is something that corresponds to reality since drag increased with the square of velocity if the drag coefficient remains constant. In both cases the Reynolds Number is above 10^5 , which suggests that our flow is turbulent. The Reynolds number is a dimensionless value that measures the ratio of inertial forces to viscous forces and describes the degree of laminar or turbulent flow. The critical Reynolds number for the transition from a laminar to a turbulent boundary layer during a subsonic flow over a flat plate is 10^5.Finally, the coefficient of drag is around 0.9 for the big model and above 1 for the 3D printed model. A general value for the coefficient of drag for a passenger car lies between 0.3-0.6 and for a racing car vary between 0.7 and 1.1, as shown from Figure 124and Figure 125.The experimental C_d values are also in agreement with the experimental C_d values of the 25% scale model of the Brno university, as presented by Lukas Frystak, p.113 - Table 8.10.

Configuration	Description	C_D	C_L	C_D/C_L
	No aerodynamic devices	0.63	0.29	0.46
	Underbody channels (diffusers)	0.65	-0.79	-1.21
	Underbody channels, wings	0.66	-1.28	-1.94
	Underbody channels, wings with side fins	0.68	-1.56	-2.29
	Underbody channels, wings with side fins and flaps	0.90	-2.34	-2.60
	Underbody channels, multi-element wings	0.98	-2.58	-2.63
	Resized underbody, revised multi-element wings	1.30	-3.70	-2.85

Figure 124: Drag and Lift coefficients of a FSAE car with different aerodynamic packages
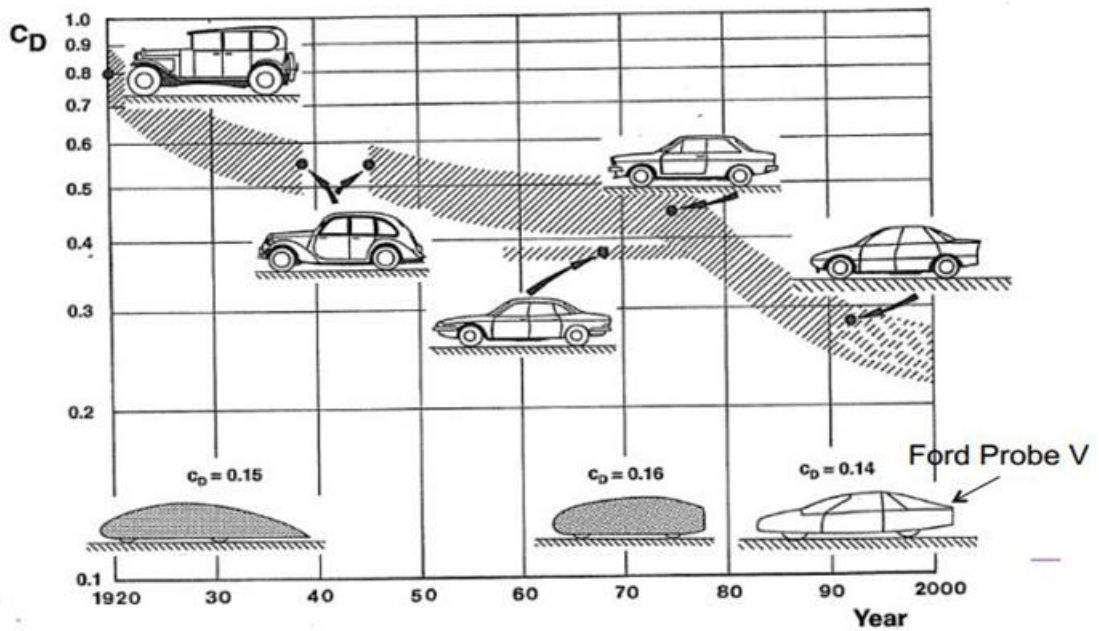
Figure 125: History of production car's CD reduction through the years

The difference is that racing cars produce 3 times more downforce (at the same speed) than the passenger car [Katz, 1996] which corrects the overall aerodynamic efficiency. In our case the C_d values correspond to the range of a race car but since they produce no downforce at all that means that their aerodynamic efficiency is bad, but that is not something that should worry us at this stage because our purpose is to validate our CFDs in order to trust our simulation tools and be able to optimize the aerodynamic package of a racing car. Since there was no equipment to measure the lift in the wind tunnel the results of the lift from the CFD simulations which were conducted using the k-ε Realizable turbulence model and a y+=30, are provided in the tables below in order to prove that the models actually produce lift rather than downforce:

Table 26: Lift Results from the CFD of the "Big Model"

Big Model	
Speed (m/s)	**Lift (N)**
8.7	0.37
10.2	0.48
11.7	0.62
13.8	0.83
15.2	0.99

Table 27: Lift Results from the CFD of the "3D Printed Model"

3D Printed Model	
Speed (m/s)	**Lift (N)**
8.9	0.05
10.5	0.072
12	0.091
14.5	0.12
15.7	0.14

4.2 CFD Results Comparison and scaling factors evaluation

After the comparison of the k-ε and k-ω simulations of the Big and the 3D printed model the k-ε was chosen as more suitable for the development of comparative simulations for the evaluation of the drag produced by a model, since the divergence was very small between the two, but the simulation converged 4 hours earlier when the k-ε was applied. For this reason, the results from the k-ε simulations were used for the evaluation of the scaling factors between the models.

4.2.1 F3 model, Big Model and "3D Printed Model" scaling factors evaluation

In the following section the comparison between the CFD results of the F3 model, the Big Model and the "3D Printed Model" are presented.

Table 28: Formula 3 vs Big Model CFD data

F3 vs Big Model - Drag Scaling Factor			
Free Stream Velocity (m/s)	CFD Drag (N)		
	F3 Model	Big Model	Scaling factor
8.7	22.32	2.00	11.18
10.2	31.00	2.76	11.24
11.7	40.73	3.63	11.22
13.8	56.64	5.08	11.15
15.2	68.73	6.17	11.14

Table 29: Big Model vs 3D Printed Model CFD data

Big Model vs 3D Printed Model - Drag Scaling Factor			
Free Stream Velocity (m/s)	CFD Drag (N)		
	Big Model	3D Printed Model	Scaling factor
8.7	2.00	0.16	12.47
10.2	2.76	0.22	12.54
11.7	3.63	0.29	12.52
13.8	5.08	0.43	11.81
15.2	6.17	0.51	12.10

The average scaling factor between the F3 and the Big Model is 11.19 and between the Big Model and the 3D Printed Model 12.29. The scaling factors have relatively small divergence, considering that the 3d Printed Model and the Big Model are 66% and 33% scaling of the F3 model respectively. In order to conclude on whether the CFD simulations can provide the engineer with accurate information the CFD scaling factor between the Big Model and the 3D

Printed Model has to be compared to the respective wind tunnel scaling factor. This information can be drawn from Table 30.

Table 30: Big Model vs 3D Printed Model CFD data

Big Model vs 3D Printed Model - Drag Scaling Factor			
Free Stream Velocity (m/s)	Wind Tunnel Drag (N)		
	Big Model	3D Printed Model	Scaling factor
8.7	1.56	0.24	6.50
10.2	2.08	0.29	7.17
11.7	2.66	0.36	7.39
13.8	4.16	0.64	6.50
15.2	5.06	0.69	7.33

The average value of the wind tunnel scaling factor is 7. This suggests that the CFD simulations are over predicting the drag of the "Big Model" and under predicting the drag for the 3D Printed model. This is a result of the fact that the boundary layer thickness is larger at the wind tunnel than the one developed in the CFDs and that might be a result of the fact that the wind tunnel's surface roughness is higher than the surface of the control volume of the CFDs. It should be mentioned that a definite conclusion on whether the wind tunnel or the CFD is right can be drawn with certainty, because the wind tunnel measurements also might contain a certain amount of error.

4.3 Wind tunnel and CFD Comparison

In the following section a comparison between the CFD and the wind tunnel drag calculations will be made. At first the "Big Model" wind tunnel and CFD results are compared in Figure 126.
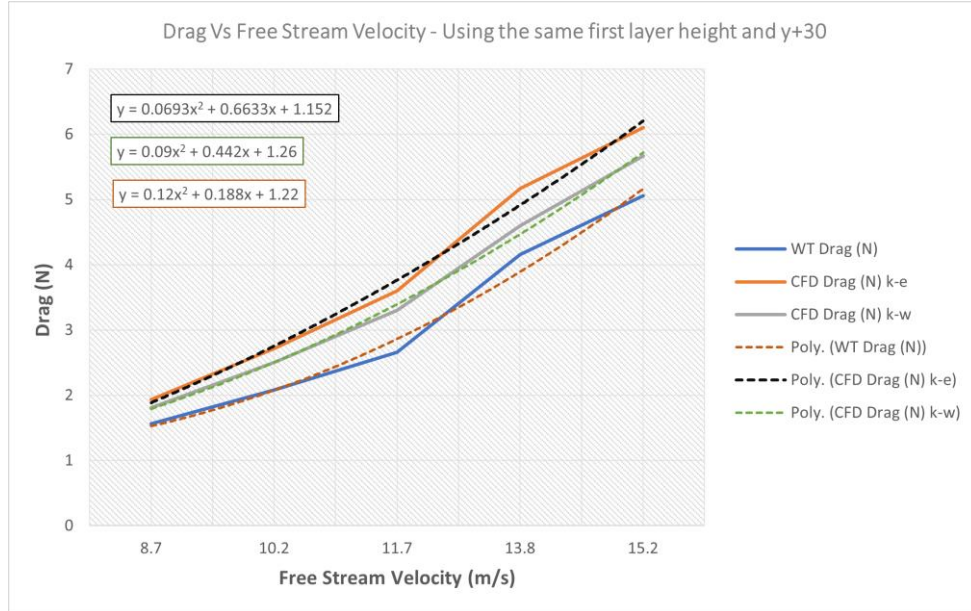
Figure 126: Wind tunnel measurements vs CFD of the "Big Model" comparison

The conclusion here is that in both cases the CFD simulations are over predicting the drag produced by the model. Any of the above cases seems to have a drag peak at 13.8 (m/s) and that might occur due to separation but that can only be proven through the post processing. Finally, the results validity is confirmed by the fact that in all three cases drag is a second order equation with respect to the free stream velocity.
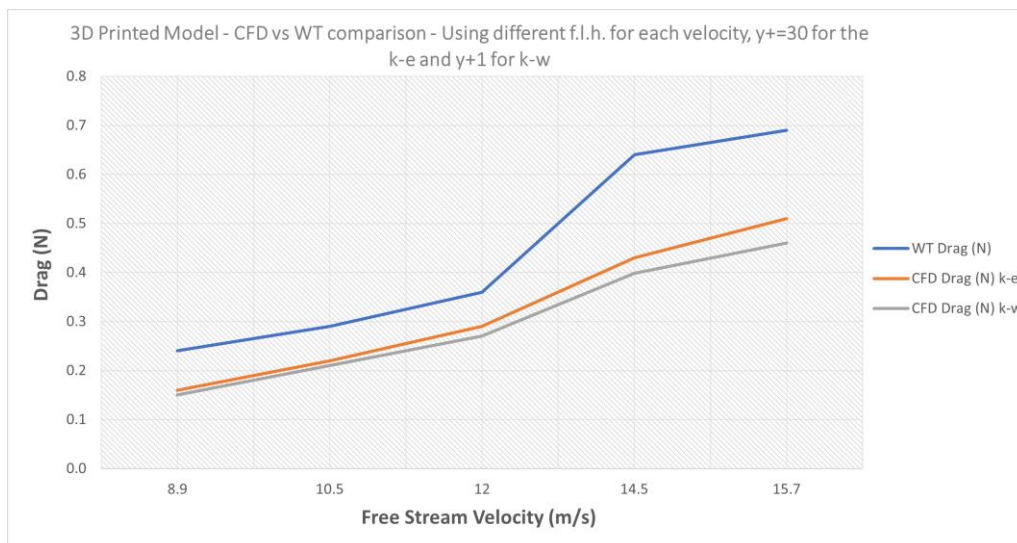

Figure 127: Wind tunnel measurements vs CFD of the "3D Printed Model" comparison

In this case someone understands that it is the opposite from what was seen in the data of the "Big Model" since the CFD lines are below the wind tunnel's line. Despite that, drag is a second order equation with respect to the free stream velocity.

4.4 Special CFD Case Studies Results

4.4.1 FSAE car Straight Simulation Results and Post Processing

4.4.1.1 Simulation Results

The straight-line simulation was performed with air moving toward the symmetrical car with a speed of 16 (m/s). Most of the comparative simulations are done using this speed since it is the average velocity of an FSAE car at the endurance track. Moreover, the road is also moving with a translational speed of 16 (m/s), while the wheels are rotating with a rotational speed of 61.53 (rad/sec). The mesh was tetrahedral dominated and consisted of 28 million cells. The boundary layer was modeled with a target $y+=30$ and the turbulence was modeled using the k-ε Realizable model with Standard wall functions approach, for near wall treatment. All the values that represent the aerodynamic performance of the car have been drawn after doubling the results that were extracted from the post processing of the symmetrical model:

Table 31: Amphion's aerodynamic performance at straight

Amphion total aerodynamic performance at 16 (m/s)						
Drag (N)	Downforce (N)	C_d	C_l	Re	C.O.P. (ref.front) %	C_l/C_d Ratio
260	-562	1.29	-2.782	2682463	52	2.2

Table 32: Aerodynamic package performance at straight

Aerodynamic package performance at 16 (m/s)			
Device	Drag (N)	Downforce (N)	C_l/C_d Ratio
Front Wing	30	-232	7.7
Undertray	14	-188	13.4
Rear Wing	108	-204	1.9

The overall efficiency of the car is characterized by C_l/C_d ratio which equals 2.2 and considering that an aerodynamically efficient race car should have a ratio above 2 (see Figure 124), the conclusion is that the car is efficient. Reading Table 32 there seems to be some lift generated which cancels out about 100N of downforce. This happens because the car consists of other part that produce lift such as the cockpit and the tires. Moreover, Table 31 shows the progress

made through the years, comparing to the overall aerodynamic performance of the Thireus, which was the predecessor of Amphion, as the downforce produced is almost doubled.

Table 33: Thireus aerodynamic performance at straight

Thireus total aerodynamic performance at 16 (m/s)				
Drag (N)	Downforce (N)	C_d	C_l	C_l/C_d Ratio
81.24	-108.87	0.532	-0.668	1.26

The data of the above table were drawn from the CFD simulations in the Thesis of [Oxyzoglou, 2018]

From Table 32 it is confirmed that the undertray is the most efficient device since it is producing a relatively high percent of the overall downforce but with a relatively small penalty in drag. Most of the downforce is produced by the front wing which is also very efficient considering the amount of downforce that it is producing. This is because the front wing interacts with the air free stream. For this reason, the front wing is the most important aerodynamic device because it can define the overall balance of the car, especially in cases where the front wing's flaps are adjustable. For this reason, most of the design development time should be spent on the front wing and the undertray rather than the rear wing. The rear wing is the least efficient device and that is because the rules restrict the teams from placing it any higher than the main hoop of the chassis. As a result, the rear wing interacts with low energy air which makes it reach an upper limit in the downforce that it can produce. So, trying different design might have a minimal effect on the overall performance. The previous conclusion will be better understood at the post processing section.

4.4.1.2   Post Processing

At this section 5 cut planes of the car are going to be studied using total pressure and static pressure plots. Total pressure is the sum of the static and the dynamic pressure and it can provide the engineers with a very good information about the quality of the air. One can imagine total pressure being very much dependent on the air's speed. Total pressure plots can give an initial idea about how effectively, aerodynamically important items, have been placed on the car. For example, if you put an aerodynamic device into a low energy area, you cannot expect it to work efficiently. So, a plot like this can tell you where high energy areas exist in order to place the aerodynamic devices properly. On the other hand, static pressure plots are useful for looking at where and how hard the air is pushing and pulling on the car. In the following figures high energy regions are indicated with the red color and very low energy regions with the blue

color, in the total pressure plots. As far as the static pressure plots are concerned red color indicates high pressure and blue color low pressure. The values in the fringe bars are given in Pascal and positive values indicate the pressure above the atmospheric while the negative values, pressure below the atmospheric.
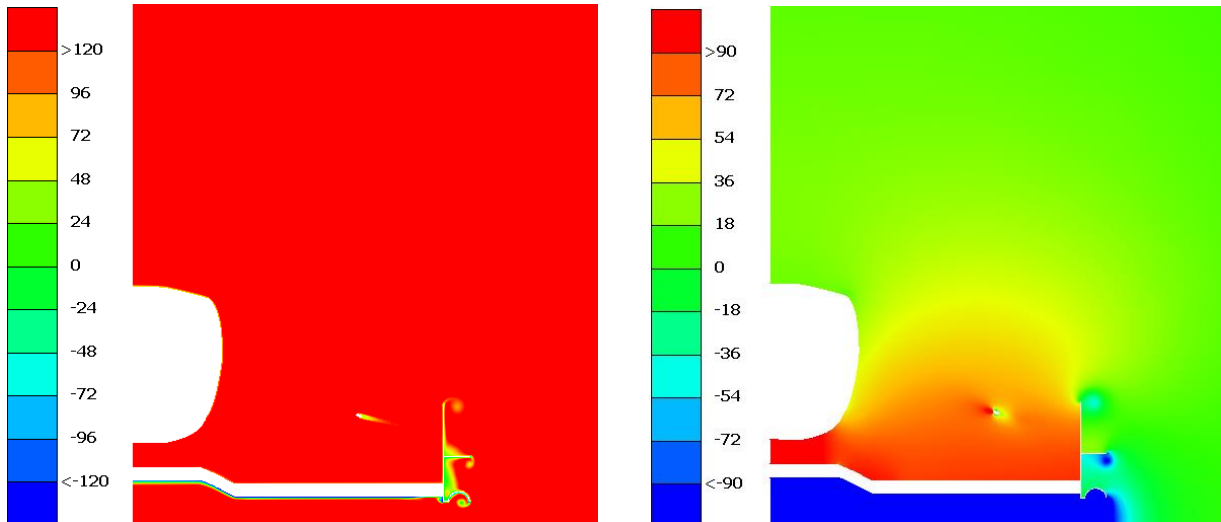

Figure 128: Front wing middle plane cut -Total pressure (left) - Static Pressure (right)

In Figure 128, a very high energy region is presented. The front wing is the most effective aerodynamic device since it is interacting the free stream's clean air. Since the front wing is placed in such a high energy region, it is an indication for the engineers that they should spend more time on the optimization of its design, rather than on any other aerodynamic device. From the static pressure plot, the pressure difference between the high-pressure region on the upper surface of the wing and the lower suction surface, is seen. The endplates role is also clearly verified since they prevent the air from moving from the upper surface to the suction side.
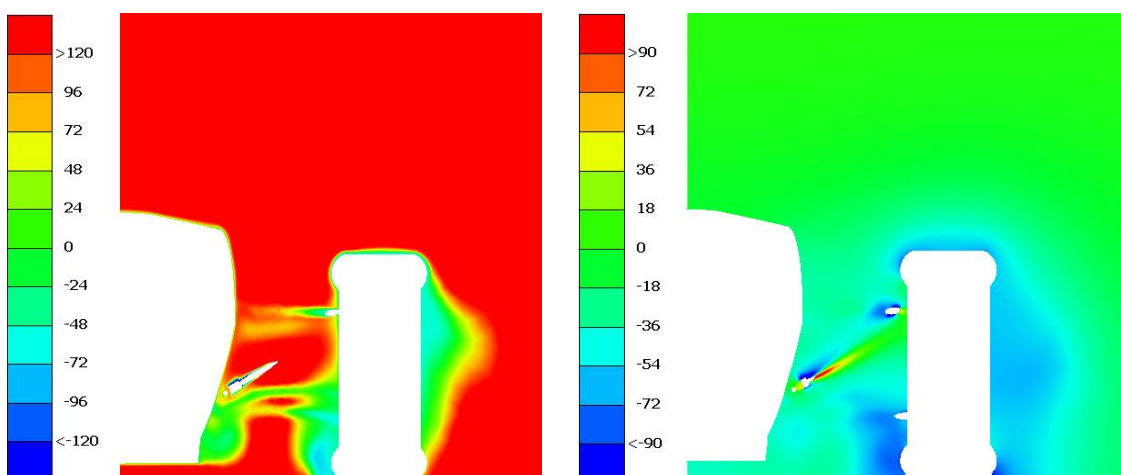

Figure 129: Front wheel middle plane cut -Total pressure (left) - Static Pressure (right)

In Figure 129, the total pressure plot indicates how the high energy is dissipated around the front wheel. The wheels are one of the biggest drag sources on the car because of the turbulence

that they produce due to their rotation. The flow also loses its kinetic energy when it crashes on the suspension's A-arms. The static pressure plot confirms that the total pressure around the wheel is mainly the result of the low static pressure. On the other hand, the total pressure loss in the suspension area is mainly caused by the kinetic energy dissipation.
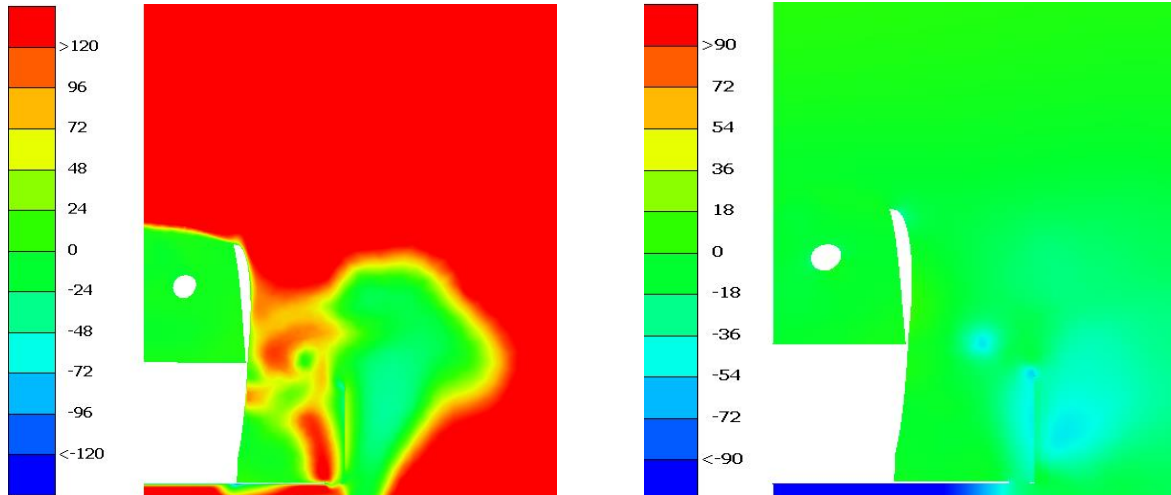
Figure 130: Plane cut in front of the undertray -Total pressure (left) - Static Pressure (right)

In

Figure 130 the total pressure indicates how much the airflow is affected by the tires and the suspension components. Moreover, a region below the front end of the undertray is spotted where energy loss is detected. This reason can be considered as a possible design change. The bargeboard also does not seem to be working properly, as big part of the front tire's wake enters the sidepod area, thus reducing the cooling efficiency. From the static pressure plot one can spot the suction area between the undertray and the road. This pressure difference is pushing the car on the road providing more grip to the tyres.
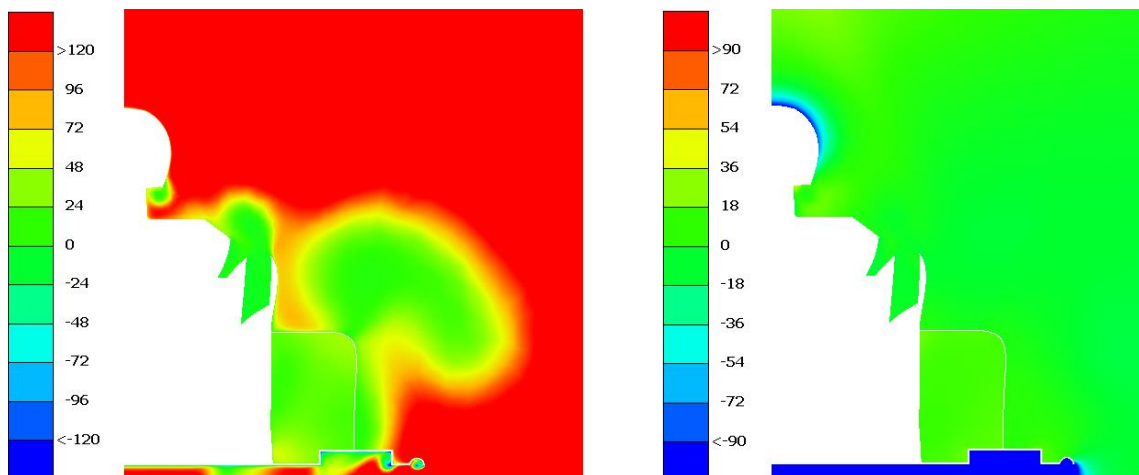
Figure 131: Undertray Middle Section - Total pressure (left) - Static Pressure (right)

In Figure 131 a good representation of the air's low pressure under the car, is done. Only the region below the car will be discussed since no radiators existed in this case. The total pressure plot indicates some losses in the energy of the air, both in the central part of the undertray but also in the side diffuser. The aerodynamic device attached to the outer side of the undertray, called "vortex tube", creates a strong vortex which drags some high energy air into the side diffuser. The problem is that the high energy across the diffuser's width is lost. That means that separation occurs, causing a loss in the overall downforce.
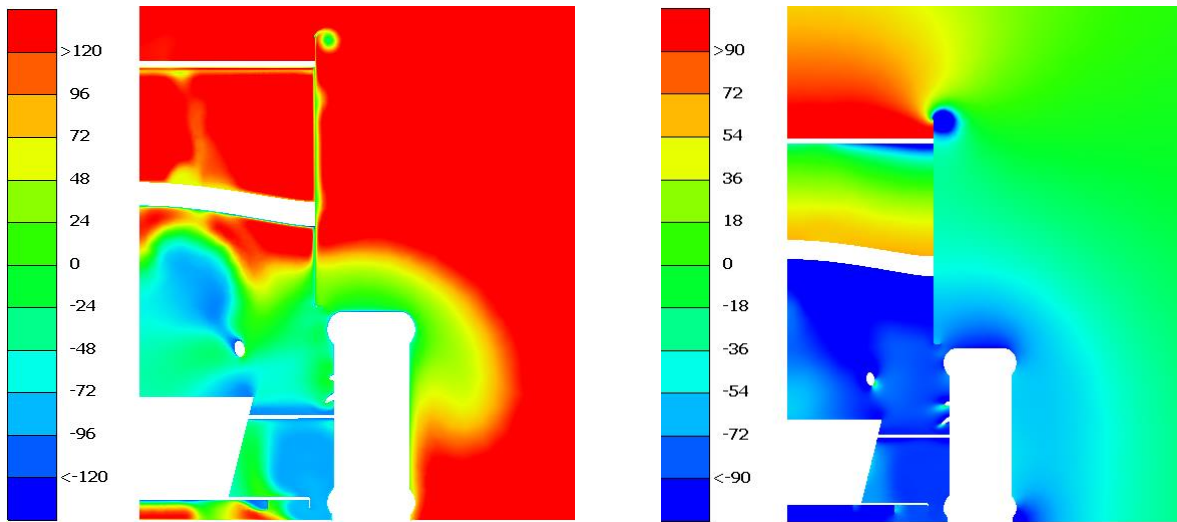

Figure 132: Rear diffuser plane cut - Total pressure (left) - Static Pressure (right)

In Figure 132 the total pressure plot gives a good representation of how the diffuser is disturbed by the rear tire's wake. Tire wake enters the undertray's rear diffuser and creates separation. This is clearly shown in the total pressure plot, from the blue region inside the rear diffuser which proves the energy loss due the tire wake. A possible solution to this problem would be a reduction of the diffuser's width. Moreover, another very low energy area is detected behind the headrest and above the engine bay. It would not make any sense to place any kind of aerodynamic device in this region. Finally, the yellow areas inside the rear diffuser are showing areas of separation.
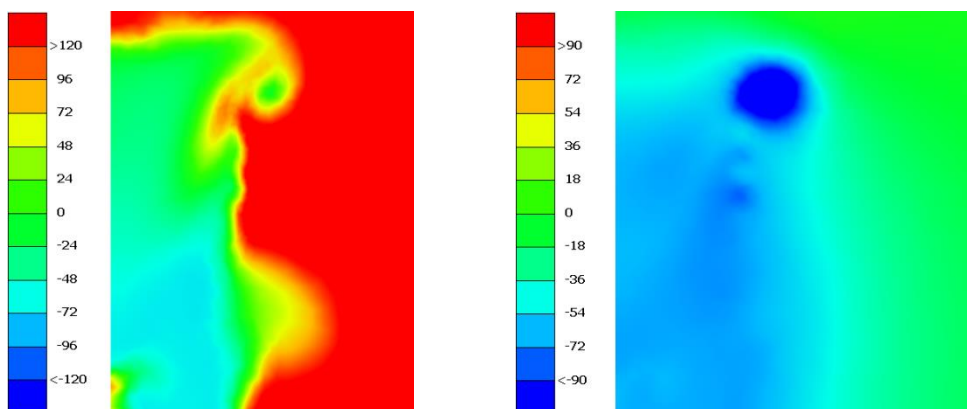
Figure 133: Plane cut behind the car - Total pressure (left) - Static Pressure (right)

In

Figure 133 there is a good representation of the car's wake. A very common spot both in the total pressure and the static pressure plot is the big vortex formed on the upper edge of the endplate.
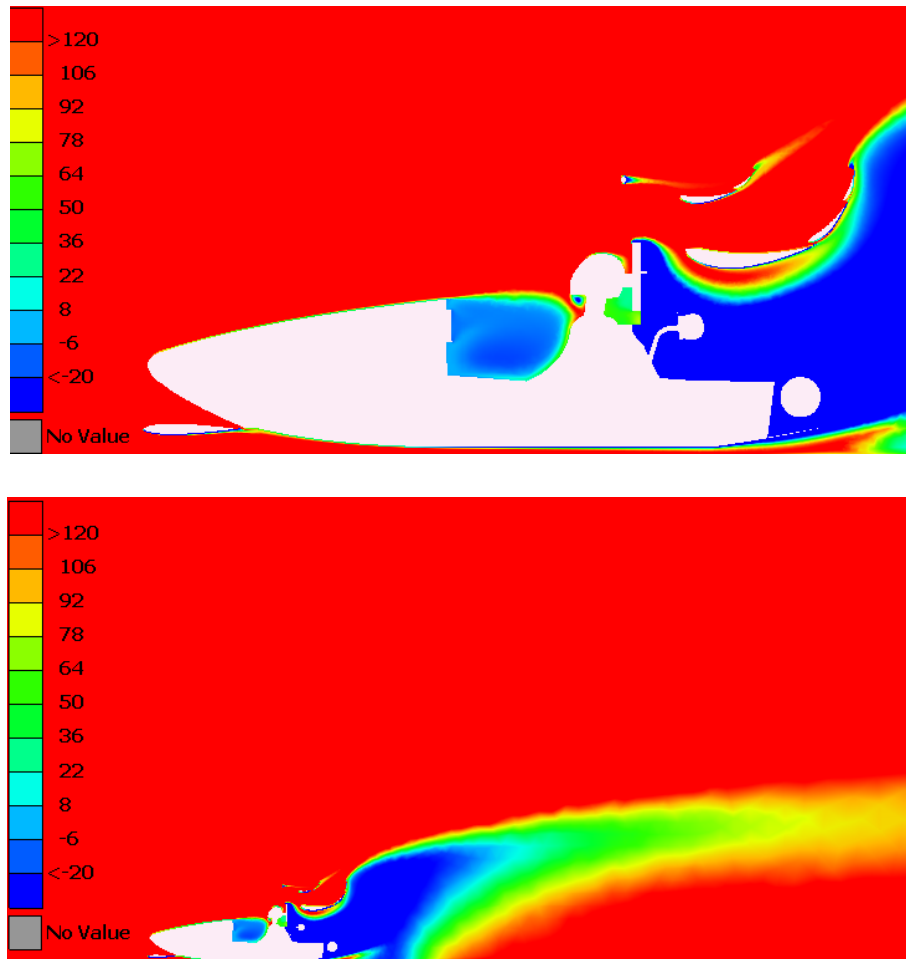
Figure 134: Symmetry plane cut - Total pressure (left) - Static Pressure (right)

In Figure 134 all the main high and the low energy areas of the car are spotted. One can see the recirculation area in the cockpit, the low energy area behind the driver's head and how it affects the performance of the lower side of the rear wing's element, but also the separation in the undertray's rear diffuser. The zoom out plot was provided in order to show the length at which the car's wake extends.

4.4.2   FSAE car Cornering Condition Results and Post Processing

During the cornering simulations, the parameter compared was the vehicle's body slip angle. In the following section the results for the 0 Body slip case are presented.

4.4.2.1   Simulation Results

In the following tables information about total aerodynamic performance of the vehicle and the performance of the main features of the aerodynamic package are presented.

Table 34: Total car aerodynamic performance for 0 Body slip

Amphion total aerodynamic performance - Body slip=0			
Drag (N)	Side Force (N)	Downforce (N)	CL/CD Ratio
243.2	-102.8	-459	1.9

Table 35: Aerodynamic package performance for 0 degrees Body slip

Aerodynamic package performance - Body slip=0				
Device	Drag (N)	Side Force (N)	Downforce (N)	CL/CD Ratio
Front Wing	20.05	-1.25	-152.90	7.60
Undertray	13.79	-5.02	-158.25	11.50
Rear Wing	102.09	-66.40	-218.10	2.10

The main difference between the cornering and the straight domain simulation is that a negative side force is created, pushing the vehicle into the turn. Moreover, there is an overall reduction in the downforce produced by the main aerodynamic devices not only because of the lower speed that the vehicle is travelling with but also because of the roll angle which affects the performance of the front wing and the undertray which are ground effect devices, while the drag is not affected that much. The ride height change due to the roll angle reduces the ground effect of the left side of the front wing and the undertray, but also prevents a large amount of air entering the right side of the devices. Reading the results of Table 35, it is understood that the center of pressure is located closer to the rear axle of the car and specifically to the left rear wheel. This indicates a possible understeering tendency of the vehicle that will prevent the driver from keeping the car to the optimum line, which will require more steering effort him in order to keep it in line, so he will lose time trying to do this correction. A necessary change to fix this problem is a configuration change on of the front wing that will make its left side produce more downforce.

4.4.2.2 Post Processing

In the figures below total pressure cut planes across the vehicle which is turning around the left circle of the Skid pad track, which corresponds to corner with a radius of 9.181m, having 0 yaw angle/body slip, 1 degree roll angle and 15 degrees steering angle, are presented:
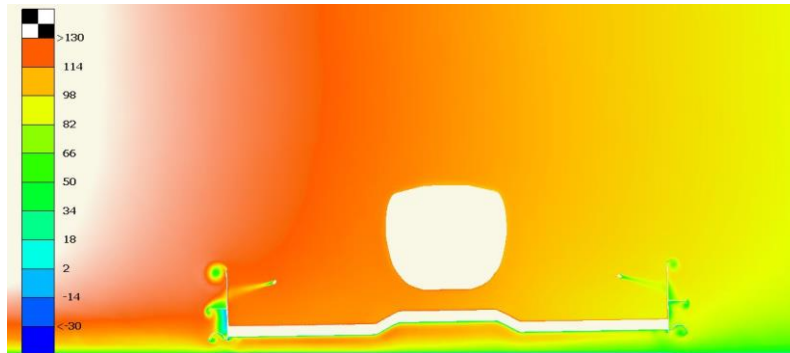
Figure 135: Front wing middle plane cut -Total pressure - 0 Body slip

Figure 135 confirms the effect of the roll angle on the performance of the front wing, since the lower ground clearance on the left side accelerates the air. Consequently, static pressure drops, thus explaining the higher total pressure in comparison to the right side.

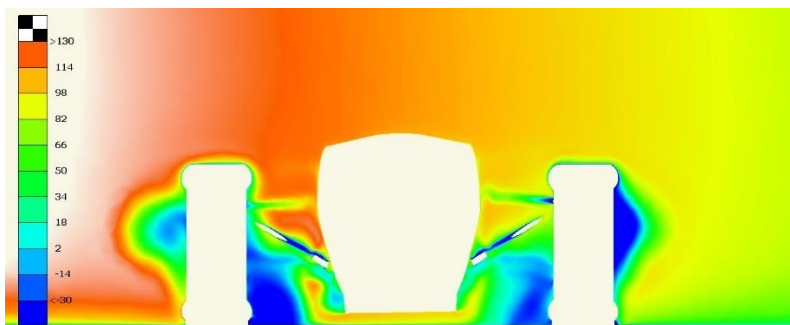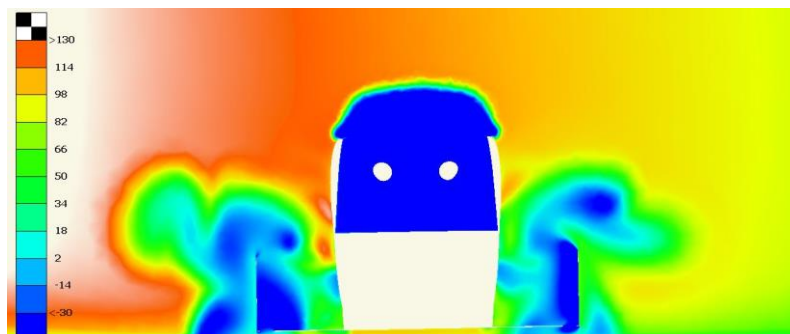**Figure 136:** Front wheels middle plane cut -Total pressure - 0 Body slip

Figure 137: Plane cut in front of the undertray - Total pressure - 0 Body slip

Figure 136 and Figure 137, represent the low total pressure regions, which build up on the outside of the front right tire and the outside surface of the bargeboard.
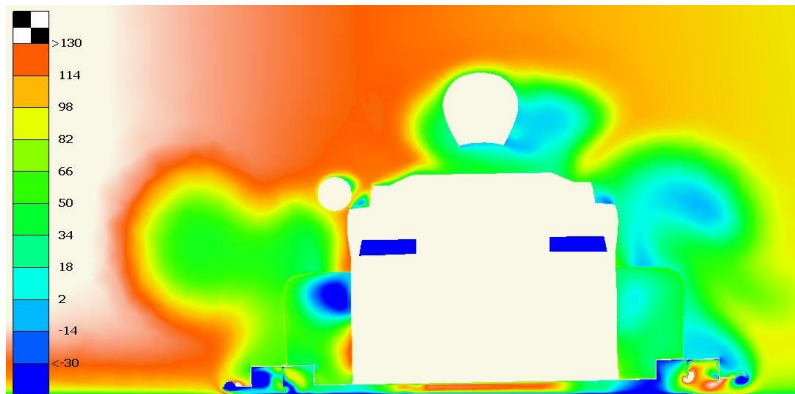
Figure 138: Undertray Middle Section - Total pressure - 0 Body slip

Once again in Figure 138, the roll angle's effect is presented when comparing the left and the right, side diffusers (as viewed from the reader's point of view). Looking at the right side due to the increment of the ride height more air is able to enter the diffuser, but then separation occurs. The only part of the undertray that seems unaffected, is the central part of the diffuser, which is characterized by a high total pressure magnitude.
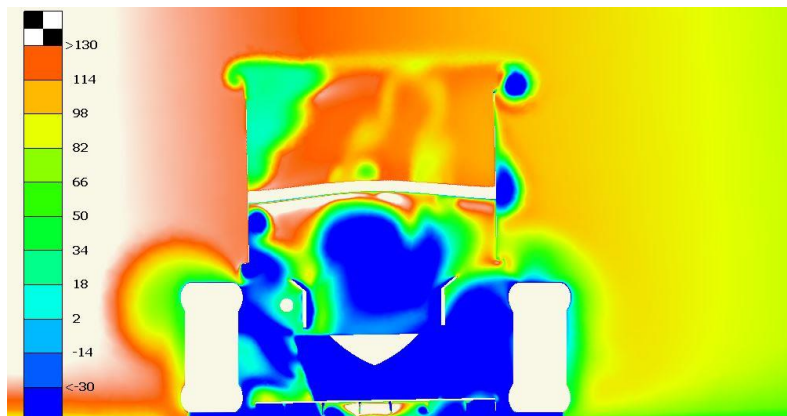
Figure 139: Rear diffuser plane cut - Total pressure - 0 Body slip

Looking at Figure 139 the rear diffuser is characterized by very low energy (around -30 Pascals) which indicates separation, almost at any point across the width of the diffuser. This dictates a possible design change because the rear diffuser is producing a very small amount of the undertray's total downforce. Moreover, looking at the top of this plane, the flow field around the rear wing is presented. This specific area shows that the rotational flow shifts the flow

towards the inside (right side of the rear wing, as viewed from a reader's point of view), while separation occurs in the left side. In Figure 140 there is a representation of the car's wake.
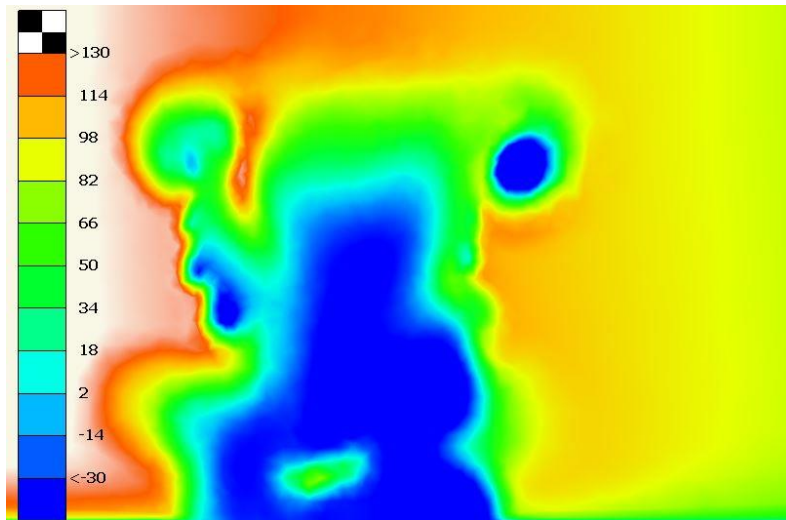
Figure 140: Plane cut behind the car - Total pressure - 0 Body slip
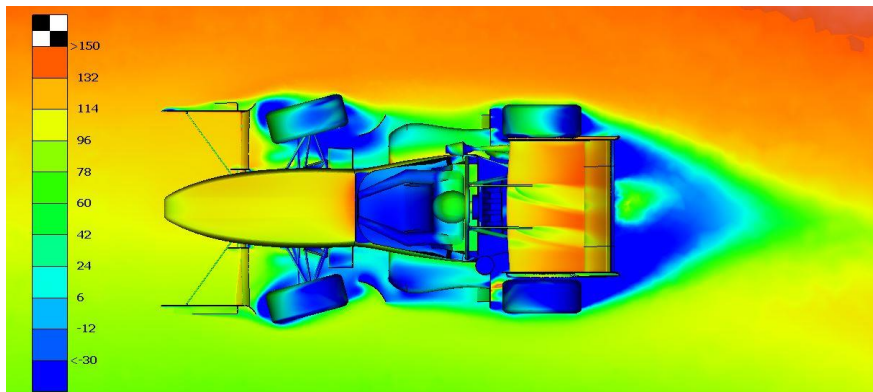
Figure 141: Plane cut parallel to the road at a distance of 20 cm above the road - Total pressure - 0 Body Slip

Watching the overview of the vehicle, while observing Figure 141, a good representation of the front tires wake, entering the sidepods, area is given. This proves that the bargeboards are not working properly, and a future redesign could help in the cooling efficiency improvement, even though engine cooling is more efficient on the straights.

5. Conclusions

5.1   Summary and Conclusions

An investigation was done on the divergence between the drag produced by two models ("Big Model, 3D Printed Model) in the wind tunnel and the drag produced by the same models through CFD simulations. After 10 experiments in total for the 2 models in the wind tunnel and more than 40 CFD simulations for the F3, the "Big" and the 3D Printed model, it was found that:

1. The results of the wind tunnel experiment showed that the drag equation with respect to the speed was a second order equation and the drag values of the "Big Model" for all the free stream velocities were at an average value 7 times larger than the drag values of the 3D Printed Model.

2. The CFD iteration dependence study suggests that the difference in the flow field and the drag value is small between 2000 and 4000 iterations. The divergence between the drag values that corresponded to 2000 and 4000 iteration was 1.3%.

3. The comparison between the hexahedral and the tetrahedral dominated mesh showed almost no difference in terms of convergence rate, computational time and results accuracy. Considering that the 2 meshes had almost the same size, the theory that wants the hexahedral mesh to be showing better accuracy, is not confirmed. Bearing in mind that tetrahedral meshes are easier to be created when complex designs are simulated, the rest of the research was done with a tetrahedral dominated mesh.

4. The mesh independence study for both models suggests that 5 million and 8 million cells for the 3D Printed and the Big Model respectively, were sufficient to produce an accurate and converged solution within 2000 iterations.

5. During the experimental study of the "Big Model" and the "3D Printed Model" 15 simulations were conducted to choose the right turbulence model. Five simulations were conducted using the k-ε turbulence model with a y+=30, another five using k-ω SST and a y+=1 and five more using again k-ω SST and a y+=30. The conclusion after this study was that solving a mesh using the k-ω SST and a y+=1 the solver manages to solve very close to the wall and that is confirmed by the fact that in post processing the velocity magnitude on the car surface is zero, and the value of the viscous drag is

lower than when solving with the k-ε Realizable and a y+=30 or with k-ω SST and y+30. The problem is that the viscous drag contribution in the total drag, in comparison to the pressure drag, is always substantial:

Free Stream Velocity (m/s)	Turbulence Model	Viscous Drag (N)	Pressure Drag (N)	Total Drag (N)
13.8	k-ε Realizable	4.75	0.33	5.08
13.8	k-ω SST	4.70	0.24	4.95

Another conclusion is that the difference in the flow field and the drag value when solving with k-ε Realizable with a y+=30 and k-ω SST with y+=1 is very small. When solving with k-ω SST and a y+=30 the drag values are closer to those obtained from the wind tunnel but the simulations last 12 hours while the k-ε lasts for 8 hours which results to a 43% reduction in computational time. For all the above reasons the k-ε model is more suitable for comparative simulations. The application of the k-ω SST using y+=30 or above has a meaning when the development of the aerodynamic package has stopped and the engineer wants to obtain a more accurate value of the performance variables that he is interested in, meaning the drag and the downforce levels of the car, otherwise he is going to waste valuable computational time while comparing cases which would have the same relationship if the simulations were performed using the k-ε. All the above need to be reevaluated in cases where large separation occurs on the geometry of the investigated model, because the k-ε might not produce accurate results. Separation can be detected by extracting the wall shear stress values of several regions of the car and searching for values close to zero. Moreover, considering a case where a dynamometer exists and makes the lift measurement possible the turbulence models also need to be reinvestigated with relation to the car's downforce/lift measured in the wind tunnel and that could also lead to a different conclusion.

6. Both the k-ε and the k-ω proved to be independent to the first layer's height change for the respective free stream velocities range. In this case the conclusion is that there it is not necessary to create different boundary layer modeling for each one of the simulated free stream velocities. Despite that being a useful conclusion for the continuation of the research, the first layer height dependency is not the general rule because f.l.h. might have a larger impact on the solution, when the speed difference between the simulations is for example 30 (km/h), so in such case it also needs investigation. The solution's

f.l.h. independency study was done after the k-ε and the k-ω comparison, so this conclusion was used for the simulation of the F3 model.

7. The comparison of the CFD drag values of the F3, the Big and the 3D Printed Model, produced by the application of k-ε model showed that the scaling factor between the F3 and the Big Model is 11.19 and between the Big Model and the 3D Printed Model 12.29. The two CFD scaling factors are very close. The scaling factor obtained from the wind tunnel experiments, between the Big Model and the 3D Printed Model was 7. Since there was a certain amount of error both in the wind tunnel experiments and the CFD simulations no definite conclusion can be made on which one of the two scaling factors should be used for the prediction of the real full-scale model.

5.2 Future Work Suggestions

Even though both the experimental and the numerical study were carried out successfully, there are still a lot of aspects that need further investigation. As far as the experimental study is concerned:

1. Further investigation of the flow field in the wind tunnel and the flow field produced by the CFD can be done, through the comparison of oil flow and streamlines symmetry planes with images drawn directly during the experiment while applying smoke in the test section.
2. Hot wire measurements behind the car in order to estimate the turbulent intensity at different free stream velocities. The intensity can also be compared to the value drawn by the CFDs.

Fifty-two CFD simulations were done and a lot of information was gathered in order to produce time effective and reliable results, but still there are many more things that can be tested in order to further improve the simulation setup and manage to reduce even more the computational time, starting with:

1. Other turbulence models such as the Spalart-Almaras or the Transition SST model.
2. Other solving algorithms such as the SIMPLEC which is the evolution of the SIMPLE algorithm.
3. Possible changes in the cornering model's setup in order to fix the problem with the boundary layer development on the road, which does not exist, and see how the aerodynamic performance is affected.

Finally, a general suggestion for the aerodynamics department of the university's FSAE team, is to create a 33% scale model of the car and by using all the tools that were developed before, predict the performance of the race car by testing different 3D Printed front wings, rear wings and undertrays and multiplying the drag and the downforce values with the suitable scaling factor. Of course, for the downforce measurement, the team has to either buy or construct and mount a scale, in the wind tunnel.

6. Bibliography

A.Hadjidimos, Successive over-relaxation (SOR) and related methods, Journal of Computational and Applied Mathematics 123 (2000) 177-199, September 1999.

Adam Jareteg, Lars Wallin, Mathias Bergfjord, Rickard Lindstrand, Adjustable wind tunnel model for an open wheeled vehicle, Chalmers Tekniska Hogskola, 2012.

ANSYS 18.1 Meshing User's Guide.

ANSYS Customer Training Material, Introduction to ANSYS Fluent, Lecture 7: Turbulence Modeling, ANSYS, Inc. Proprietary© 2010 ANSYS, Inc. All rights reserved, Release 13.0, December 2010.

ANSYS Fluent 12.0 User Guide, Standard Wall Function.

ANSYS Meshing Application Introduction, Appendix A, Mesh Quality.

B. E. Launder and B. I. Sharma Application of the energy dissipation model of turbulence to the calculation of flow near a spinning disc, Letters in Heat and Mass Transfer, 1974, 1, pp. 131-138.

B. E. Launder and D. B. Spalding, The numerical computation of turbulent flows, Comp. Methods in App. Mech and Engineering 3, 1974, pp. 269-289.

Barlow, J. B., Rae, W. H., Pope, A.: Low-Speed Wind Tunnel Testing, Copyright B 1999 by John Wiley & Sons. All rights reserved, ISBN: 978-0-471-55774-6.

D.D. Apsley & M.A. Leschziner, Advanced Turbulence Modelling of Separated Flow in a Diffuser, January 2000.

Deepak Sahini, Wind Tunnel Blockage Corrections, Master Thesis, Texas Tech University, 2004.

Durrer Simon, "Aerodynamics of Race Car Wings: A CFD Study", Master's Thesis. 798., 2016.

F.R. Menter, Two-equation eddy-viscosity turbulence models for engineering applications, Nasa Ames Research Center, Moffet Field, California 94035.

Finn E. Jorgensen - 2002 - © Dantec Dynamics A/S, P.O. Box 121, Tonsbakken 16-18, DK-2740 Skovlunde, Denmark, Publication no.: 9040U6151.

Guoxin Wan, Yinuo Hu, Tingting Xu, Zefei Li, Bo Yang, Numerical Simulation and Wind Tunnel Experiment of the Aerodynamic characteristics of a Formula Student Racing Car, State Key Laboratory of Automotive Simulation and Control, Jilin University, 5988 Renmin Street Changchun, China, Article · September 2013

H.Jasak, 'Error Estimation and Analysis for the Finite Volume Method with Application to Fluid Flows', Thesis submitted for the Degree of Doctor of Philosophy of the University of London and Diploma of Imperial College, Department of Mechanical Engineering Imperial College of Science, Technology and Medicine, June 1996.

Henrik Dahlberg, Aerodynamic development of Formula Student race car, Bachelor Thesis, KTH Mechanics, August 2014.

http://www.bakker.org, Andre Bakker, CFD Lectures, Lecture 7, 2008.

https://www.grc.nasa.gov/WWW/K-12/airplane/short.html

Ioannis Oxyzoglou, Design & Development of an Aerodynamic Package for an FSAE Race Car, University of Thessaly, Faculty of Mechanical Engineering, May 2018.

J. Bredberg. On the wall boundary condition for turbulence models. Internal report 00/4, Chalmers University of Technology, Sweden, 2000.

J. Katz: Race Car Aerodynamics: Designing for Speed (Engineering and Performance), ISBN-13: 978-0837601427, 1996.

J. Keogh, T. Barber, S. Diasinos, and G. Doig, "Techniques for Aerodynamic Analysis of Cornering Vehicles," SAE Technical Paper 2015-01-0022, 2015, doi:10.4271/2015-01-0022.

Jo Yung, Theory of ground vehicles (Second ed.). Wiley. pp. 52–53. ISBN 978-0-470-17038-0, 2008.

Joseph Katz and Darwin Garcia, 2002, Aerodynamic Effects of Indy Car Components. Proceedings of the 2002 SAE Motorsports Engineering Conference and Exhibition [online]. 2002. No. 2002-01-3311p. 11. DOI 10.4271/2002-01-3311. Retrieved from: http://papers.sae.org/2002-01-3311/

Joseph Katz and Robert Walters, 1995, Investigation of wind-tunnel wall effects in high blockage testing. In: 33rd Aerospace Sciences Meeting and Exhibit [online]. Reston, Virginia American Institute of Aeronautics and Astronautics.09 January 1995. p. -. Retrieved from: http://arc.aiaa.org/doi/ abs/10.2514/6.1995-438

Kristian F. Sagmo, Computational fluid dynamics simulations of a Formula Student racecar - Effects predicted by the modeling of a steady state cornering vehicle, Norwegian University of Science and Technology, September 2016.

LEAP Australia, Tips and Tricks, Convergence and Mesh Independence Study.

Lukas Frystak, Formula SAE aerodynamic optimization, Brno Institute of Technology, Faculty of Mechanical Engineering, 2016.

M.V. Cook, Flight Dynamics Principles, Copyright © 2007, Published by Elsevier Ltd.

Massimo Guiggiani, The science of Vehicle Dynamics, Springer Netherlands, ISBN 978-94-017-7687-5, 2014.

Miguel A. González, José Miguel Ezquerro, Victoria Lapuerta, Ana Laverón, and Jacobo Rodríguez, Components of a Wind Tunnel Balance: Design and Calibration, Escuela Técnica Superior de Ingenieros Aeronáuticos Universidad Politécnica de Madrid Spain, July 2011.

Miroslav Kratochvnl, Nikita Astraverkhau, Vntek Slanina, Wings Improving Driving Parameters, CTU Cartech, Czech Repuplic, MECCA 02 2014.

P. Lesniewiczl, M. Kulak and M. Karczewski Aerodynamic analysis of an isolated vehicle wheel, Institute of Turbomachinery, Lodz University of Technology, Poland, Article in Journal of Physics Conference Series · August 2014

Pacejka, Hans B., Tire and Vehicle Dynamics (2nd ed.). Society of Automotive Engineers, Inc. pp. 5. ISBN 0-7680-1702-5, 2006.

Richard G.J. Flag and Andrew R. Hammond, Aerodynamic Design of a Formula SAE Race Car, The University of Auckland, New Zealand, 2006.

Versteeg and Malalasekera, An introduction to Computational Fluid Dynamics: The Finite Volume Method, Longman Scientific & Technical, © Pearson Education Limited 1995, 2007 United Kingdom issued by the Copyright Licensing Agency Ltd, Saffron House, 6–10 Kirby Street, London EC1N 8TS, ISBN: 978-0-13-127498-3.

W. P. Jones and B. E. Launder The prediction of laminarization with a two-equation model of turbulence, Int. Journal of Heat and Mass Transfer, 15, 1972, pp. 301-314.

Wolf-Heinrich Hucho, Wong and Gino Sovran, Aerodynamics of Road Vehicles, Annu. Rev. Fluid Mech. 1993.25 :485-537, Copyright © 1993 by Annual Reviews Inc. All rights reserved.

X. Zhang, W. Toet, and J. Zerihan. Ground effect aerodynamics of race cars. Applied Mechanics Reviews, 59:33–49, January 2006.